BIOENGINEERING *IN VITRO* HUMAN TRABECULAR MESHWORK MODELS FOR GLAUCOMA THERAPEUTIC SCREENING

By

Karen Y. Torrejon

A Dissertation

Submitted to the University at Albany, State University of New York

in Partial Fulfillment of

the Requirements for the Degree of

Doctor of Philosophy

College of Nanoscale Science and Engineering

2015

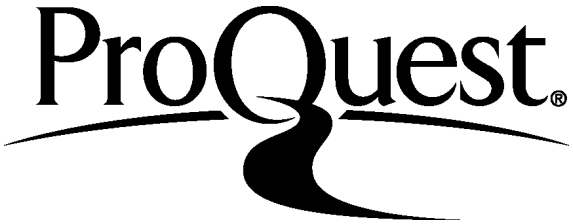

Dedication

This dissertation is dedicated to my caring mother Yud Oré, my loving brother Jorge Torrejón, my grandparents Abraham Oré and Consuelo T. León, and the entire Oré/León family-past, present and future.

Contents

Acknowledgements

This dissertation has become a reality by the hand of God, who makes everything possible and who has put on my path a wonderful group of individuals who encouraged and guided me through this journey.

I am thankful to my advisors Dr. Susan Sharfstein and Dr. Xie for their understanding, constant encouragement and for pushing me to reach beyond my expectations. It has been both, a privilege and pleasure to work with them. Thanks to Dr. Magnus Bergkvist for his always challenging questions which made me think critically about every piece of work I've done. I am also grateful for the input and guidance I have received from Dr. John Danias, without him none of this work would have been possible. To my committee member Dr. Lee Ligon, thank you for taking time out of your busy schedule to have input in my work and scientific discussions that helped greatly as I was putting this dissertation together. I am also thankful for the support I have received from Dr. Laura Schultz, Mr. Nicholas Querques and Dean Pradeep Haldar, who always took time to discuss with me the market potential to the technology described in this dissertation and have given me much needed advice on all aspects of pursuing a career in entrepreneurship as a scientist and have shared my pain during the process. Overall it has been a wonderful experience to work alongside with these mentors/scientists/professors/advisors who have become my role models and colleagues; each of them embodies different characteristics which I admire.

Despite the ups-and-downs that one faces through graduate school, I have been fortunate to share all these experiences with Dr. Andrea Unser, Dr. Nicole Flaherty, Ms. Bushra Alam, Ms. Genieve Kane, Dr. Mary Graham, Dr. Donnie McCarthy, Dr. Michael Padgen, Dr. James Williams, Mr. Paul Kutscha, Ms. Akshaya Chandrasekaran, Dr. Nurazhani Raof and Dr. Michael Zonca. Along the way I have shared many laughs (which have kept me sane throughout graduate school!) with Ms. Isabel Tian, Ms. Lauren Sfakis, Mr. Martin Tomov, Ms. Bridget Mooney.

Perhaps one of the most rewarding experiences throughout my years in graduate school has been mentoring undergraduate students Ellen Papke, Justin Halman, Adam Goodcoff, Ben Breiten and Erik Milosevic; all who, one way or another, have aid in the performing or design of some experiments described in this dissertation. I hope to have inspired them as much as they have inspired me to continue working hard.

I am grateful to the funding sources that made this project and its dissemination possible, including the National Science Foundation's Graduate Research Fellowship and SUNY Research Foundation's Technology Accelerating Funds.

I am extremely thankful for all the help, active discussions and support I have received from Brendan O'Brien. He helped tremendously with the use of the scanning electron microscope and with the perfusion device. Brendan has provided much needed moral support throughout all my years of graduate school and has kept me

company during the late nights/early mornings I had to be in lab for perfusion studies therefore for that and much more Thank You!

Most importantly, Thanks to my mother and brother for their patience and understanding; especially during all birthdays and holidays I had to miss due to working in lab or attending conferences. “My dreams are your dreams”. My mother has made countless sacrifices to give me the education I have received and my achievements are as much hers as they are mine. My brother has always being a motivation for all the work I have put into this dissertation, especially as prove that with effort, prayers, perseverance and much sacrifices one ought to accomplish almost anything. To my entire family: Thanks for all your prayers, support, advice, words of encouragement and for sharing my goals! Although we live far away, I have thought of you every step of the way and that has kept me going all these years.

Abstract

Glaucoma refers to a group of slowly progressing eye disorders that lead to damage to the optic nerve, resulting in irreversible vision loss. Recent statistics by the World Health Organization places glaucoma as a leading cause of blindness worldwide, affecting nearly 80 million people. Lowering intraocular pressure (IOP) is currently the only effective target for therapeutic intervention in glaucoma. IOP is mostly controlled by the outflow of the aqueous humor (AH) through the trabecular meshwork (TM). The TM and adjacent endothelium of Schlemm's canal, known as the conventional outflow-tract, control AH outflow and thus determine IOP.

One major challenge for development of effective glaucoma therapeutics, those targeting the conventional outflow tract, is the lack of proper, *in vitro* models for outflow and IOP-related studies. To overcome this challenge, we developed a bioengineered, 3D *in vitro* human trabecular meshwork (HTM) model to further understanding of outflow physiology and evaluate IOP-lowering agents. The central hypothesis of this dissertation is that well defined, porous substrates with a suitable biomacromolecular coating, could support culture of primary HTM cells to mimic the structure and outflow physiology of the HTM. Scaffold architecture and culture conditions were optimized, including pore size, beam width, surface coating, seeding density and cultivation period. Expression of HTM-markers was analyzed and after decellularization, the extracellular matrix surrounding/secreted by the HTM cells was surveyed to confirm the presence of appropriate basement membrane proteins. To assess the physiological behavior of our bioengineered 3D HTM, a perfusion system that hosts the construct was constructed. This system allowed perfusion at various flow rates with constant pressure monitoring.

The outflow facility of our construct was calculated to be comparable to its in *vivo* counterpart. The responsiveness of our bioengineered HTM was confirmed by treatment with active biological agents known to affect outflow physiology. Furthermore, co-culture and differentiation methods along with microfabrication techniques were explored to develop a more complex 3D human conventional outflow tract model. Overall, work presented in this dissertation confirms the applicability of a bioengineered 3D HTM in TM-physiology studies and for screening agents affecting IOP.

List of Abbreviations

AH	Aqueous humor
CD-31	Platelet endothelial cell adhesion molecule-1
CD-34	Hematopoietic progenitor cell antigen CD34
Col1A1	Collagen -1A1
colIV	Collagen type IV
CTGF	Connective tissue growth factor
DAPI	4',6-diamidino-2-phenylindole
DMEM	Dulbecco's modified Eagle's medium
ECM	Extracellular matrix
EfnB2	Ephrin-B2
FBS	Fetal bovine serum
FOXC2	Forkhead box protein C2 or forkhead-related protein FKHL14
FSP-1	Fibroblast specific protein-1
GAPDH	glycerol 3 phosphate dehydrogenase
GC	Glucocorticoids
GFP	Green fluorescent protein
HA	Hyaluronic acid
HMVEC	Human microvascular endothelial cells
hrs	Hours
HSC	Human Schlemm's canal
HTM	Huma trabecular meshwork
IHC	Immunohistochemistry
IL-1α	Interleukin-1 alpha
IMEM	Improved minimum essential medium
JCT	Juxtacanalicular region
Lat-B	Latruncunlin B

LC	Lamina cribriosa
LPA	Lysophosphatidic acid
LVP	Limbal vascular plexus
min	Minutes
miRNA	microRNA
MMP-2	Matrix metalloproteinase-2 or gelatinase A
MMP-3	Matrix metalloproteinase-3 or stromelysin-1
MRTF	Myocardin-related transcription factor
PA	Prednisolone acetate
PECAM 1	Platelet endothelial cell adhesion molecule-1
POAG	Primary open-angle glaucoma
PROX1	Prospero homeobox protein 1
q-PCR	Quantitative polymerase chainreaction
RG	Retinal ganglion
ROCK	Rho-associated kinase
RT-PCR	Reverse transcriptase polymerase chain reaction
RV	Radial vessels
SC	Schlemm's canal
SD	Standard deviation
SEM	Scanning electron micrograph or scanning electron microscope
SRF	Serum response factor
TGFβ-2	Transforming growth factor beta-2
TGF-β2	Transforming growth factor-beta 2
Tie2	Tyrosine-protein kinase receptor
TIMP-1	Tissue inhibitor of metalloproteinases-1
TM	Trabecular meshwork
UV	Ultraviolet
VE-cadherin	Vascular endothelial cadherin

Vegfr2	Vascular endothelial growth factor receptor-2
αB-crystallin	Alpha B-crystallin
α-SMA	Alpha-smooth muscle actin
°C	Degrees Celsius

Overview

I. Objective and Significance

The long term goal of this project is to develop a bioengineered, three-dimensional (3D) *in vitro* human trabecular meshwork model to better understand the hydrodynamics of the conventional outflow tract, for high-throughput screening of medications or new treatments for glaucoma. Glaucoma is a devastating neurodegenerative disease, which often leads to vision loss. According to the World Health Organization, glaucoma is a leading cause of blindness worldwide. In the U.S. alone, approximately 2.2 million people have glaucoma; of these individuals, 120,000 are blind [1] . In addition, with the world's population aging, the number of people affected by glaucoma will likely increase dramatically. The main risk factor that causes glaucoma is increased intraocular pressure (IOP) [1]. In humans, IOP is primarily controlled by the outflow of the aqueous humor through the trabecular meshwork (TM). Efforts to understand the physiology of the HTM have, over the years, provided some cues as to the pathology that leads to IOP elevation in glaucoma. While conventional HTM cell cultures are useful for studying the biology of HTM cells [2, 3], they are not suitable for evaluating the effects of medications on outflow facility [4-7]. Current outflow studies mainly rely on anterior segments of animal or human eyes [1, 8-12]; however, the preparation of these perfusion systems is cumbersome, and expensive, and not suitable for high-throughput screening [13]. Further advances in pharmacological treatment of glaucoma are, at this time, limited by the lack of proper, efficient, *in vitro* models for the screening of new, potential therapeutics [1]. Therefore, there is a great need for a bioengineered,

functional, *in vitro*-HTM model for outflow studies and glaucoma drug screening. Such a model would advance understanding of the HTM and provide a platform for low-cost, less invasive, novel studies related to the eye, facilitating drug discovery and effective treatment of glaucoma.

The central hypothesis of this dissertation is that well-defined, porous substrates with a suitable biomacromolecular coating will support HTM cell growth to mimic the structure and outflow physiology of the HTM. The work performed during this thesis aimed to develop a bioengineered, 3D *in vitro* HTM complex for understanding outflow physiology and testing IOP-lowering agents. It was anticipated that the 3D HTM system would have anatomic similarities to the actual HTM and behave similarly in terms of outflow characteristics. If successful, this bioengineered HTM will advance the understanding of the TM and provide a platform for low cost, animal-free studies related to the eye and testing of glaucoma therapeutics. At the same time, this model will permit novel therapeutics that target the TM to be developed, increasing the specificity of the future anti-glaucoma drugs.

To test the central hypothesis of this thesis, the following studies were performed:

Study 1: Recreation of an *in vitro* HTM model on well-defined microporous scaffolds incorporated into a perfusion platform

Summary: Highly porous scaffolds of biocompatible SU-8 photoresist with pore sizes ranging from 7-15 μm and different pore shapes were fabricated using photolithographic techniques to mimic the perforated sheet-like structure of the HTM. Primary HTM cells

were cultured on these scaffolds, and the culture conditions were optimized, including pore size, beam width, surface coating, seeding density, and cultivation period. Cell growth on SU-8 scaffolds and commercially available porous filter membranes was evaluated and compared by staining the cytoskeleton and evaluating expression of extracellular matrix (ECM) secreted proteins, to assess successful cell attachment and *in vivo*–like HTM morphology. Additionally, expression of HTM-markers such as α-smooth muscle actin, myocilin and αB-crystallin, was analyzed. After decellularization, the ECM surrounding/secreted by the HTM cells was surveyed to confirm the presence of basement membrane proteins similarly to those expressed at the juxtacanalicular (JCT) area of the HTM. To assess the physiological behavior of our bioengineered 3D HTM, a perfusion apparatus with a perfusion chamber and suitable pressure sensor was built. 3D HTM constructs were perfused at various flow rates with constant pressure monitoring. The outflow facility of our constructs was calculated from a formula similar to the one used to calculate outflow facility in organ cultures and *in vivo*: Outflow Facility = change of flow (ΔF)/ change in pressure across the 3D HTM (ΔP). Modulation of outflow facility by latruncunlin B, at various concentrations was confirmed.

Significance: The optimization of culture conditions for HTM cells is imperative when attempting to develop a bioengineered model. This initial optimization provides us with insight on the parameters to use for the remaining studies. The HTM-marker assessment is key to confirming that the primary HTM cells retain their proper markers and do not dedifferentiating; most importantly, given that many of these markers are known to be lost in 2D cultures on plastic or glass coverslips or on Transwell® membrane inserts, the maintenance of these markers suggests a more *in vivo*-like

phenotype. Additionally, the perfusion studies allow us to further mimic the aqueous humor (AH) flow dynamics through our 3D bioengineered HTM. Utilizing a range of flow rates, the outflow facility of our models was calculated and is comparable to its *in vivo* counterpart. The perfusion studies and treatments with latrunculin -B directly related cell-cytoskeletal organization to pressure changes across the HTM.

Study 2: Development an *in vitro* HTM steroid-induced glaucoma model to study cytoskeletal, ECM, and outflow resistance changes that induce increased IOP

Summary: Utilizing optimized concentrations of prednisolone acetate (PA), a steroid-induced glaucomatous HTM model was developed using the bioengineered HTM construct. The changes in marker expression and ECM production in this model were assessed by immunocytochemistry, western blotting, and qPCR. In addition, the phagocytic activity of this disease model was assayed. Changes in transcellular electric resistance and outflow resistance were studied by real-time electrical cell-substrate impedance sensing (ECIS) and perfusion studies, respectively. To attempt to reverse ECM induction observed in this *in vitro* glaucomatous HTM model, rho-associated protein kinase (ROCK) inhibitor (Y-27632) was used and ECM remodeling was studied by immunocytochemistry qPCR analysis of metalloproteinase (MMP)-2 and -3 expression. Time-course gene expression studies of the cytokines tissue inhibitor of metalloproteinase (TIMP)-1, interleukin 1-alpha (IL-1α) and transforming growth factor-β (TGFβ) was studied over 9 days of treatments with PA, Y-27632/PA, and Y-27632 alone.

Significance: This model can be utilized to further understand the biological and physiological changes that happen at the HTM that induce increased IOP. This model was characterized by changes similar to those described in *ex vivo* steroid-induced glaucoma models such as actin rearrangements, ECM overproduction, decreased phagocytic activity and decreased outflow facility. The changes, over time, in ECM remodeling genes such as MMP-2 and -3 and cytokine TIMP-1 were consistent with the ECM induction and elevated resistance demonstrated in this glaucomatous HTM model. Furthermore, given the growing interest on developing ROCK inhibitors as a new class of glaucoma drug that act at the HTM, the effects of a ROCK inhibitor in combination with PA were studied in our bioengineered HTM model.

Study 3: Determination of TGFβ-2 effects and analysis of the potential anti-fibrotic properties of rho-associated kinase inhibitors on the bioengineered in vitro HTM

Summary: The resistance and outflow facility of our bioengineered HTM model was assessed through perfusion studies after TGFβ-2 treatment. Rearrangement of F-actin and α-smooth muscle actin after TGFβ-2 treatment were assessed. Additionally, the effect of TGFβ-2 on HTM-marker expression such as myocilin and αB-crystallin was investigated. The ability of ROCK inhibitors to reverse the changes caused by TGFβ-2 was studied for ECM proteins, HTM-markers, ECM remodeling genes, cytokine mRNA expression, and outflow resistance.

Significance: Elevated levels of TGFβ-2 have been found in the AH of patients with glaucoma. Therefore this study was designed to investigate the changes that could be induced by clinically-relevant exogenous TGFβ-2 concentrations at the HTM utilizing our

bioengineered HTM model. TGFβ-2 effects on resistance, across the bioengineered HTM was analyzed. Given that changes in ECM proteins have been described for *in vivo* glaucomatous HTM, we investigated similar ECM changes that could be induced by TGFβ-2. Additionally, the potential anti-fibrotic effect of ROCK inhibitor, Y-27632, was analyzed.

Study 4: Development of a novel 3D *in vitro* model of the conventional outflow tract utilizing co-culture and differentiation methods along with microfabrication techniques

Summary: We attempted to differentiate primary human microvascular endothelial (HMVEC) cells into human Schlemm's canal (HSC) cells by biochemical cues. A 3D co-culture HTM/HMVEC construct was developed using porous scaffolds coated with hyaluronic acid-based hydrogels and primary HTM and HMVEC cells. The length of cell culture for this co-culture protocol was optimized. Phenotypical changes of HMVEC cells in co-culture with HTM cells were characterized and compared to HTM/HSC co-culture construct. Vacuole/pore formation was induced by perfusion in both the HMVEC and HSC cell layer under co-culture.

Significance: Given the successful development of our bioengineered HTM model, to add complexity and better mimic *in vivo* interactions between the HTM and HSC inner wall cell layer, HSC or HSC-like cells were seeded in co-culture. Interestingly, under 3D co-culture conditions, HMVEC cells appear to differentiate and resemble HSC endothelial layer. Given the recent findings on HSC development which describes the vascular-lineage of the developing HSC tissue, this finding is of great importance since

it could provide insight into the mechanism of HSC differentiation. Additionally, the 3D co-culture constructs developed during this study could prove useful for studying the effect of vacuole/pore formation at the HSC/HSC-like cell layer in outflow regulation.

II. Organization of the Dissertation

First, this overview section presents the long-term goal, objectives and significance of the project. Next, CHAPTER 1 introduces the background and motivation of this thesis, including glaucoma, the biology and structure of the TM, state-of-the-art TM models, and opportunities of utilizing micro-/nanofabrication for bioengineering TM tissue models. In CHAPTER 2, the feasibility of using microfabricated well-defined porous scaffolds to develop a bioengineered HTM model was explored. The characterization of such model including cell morphology, HTM-markers and ECM proteins expression are discussed. Additionally, perfusion studies with or without pharmacological compound latruncunlin-B, are used to analyzed transcellular pressure changes and calculate the outflow facility of this model. In CHAPTER 3, an *in vitro* glaucomatous HTM model is developed by steroid-induced changes at the bioengineered HTM. The biological and physiological changes caused by steroid treatment at the bioengineered HTM were characterized. Furthermore, gene expression of ECM turnover proteins and cytokines by HTM cells were investigated in response to steroid with or without ROCK inhibitor treatment. In CHAPTER 4, the bioengineered HTM model was used to study the effect of TGFβ-2 in the HTM outflow facility. The fibrotic and probable tissue hardening induced by TGFβ-2 is discussed. Additionally, the potential use of ROCK inhibitor to reverse TGFβ-2 fibrotic effect and increase outflow facility are explored. During CHAPTER 5, the differentiation of HMVEC cells to HSC-like cells was explored. A 3D co-culture construct of HTM/HMVEC was developed

using our well-defined microfabricated porous scaffolds along with hyaluronic acid-based hydrogel coating. Such co-culture construct induced morphological changes at the HMVEC cell layer, resembling HSC cell morphology which was further characterized. The differences and similarities between the HTM/HSC and HTM/HMVEC constructs were examined. Overall, the results obtained in this study demonstrate the feasibility to develop a conventional outflow tract model of higher complexity that our bioengineered HTM. Lastly, the entire dissertation is deduced in the section titled SUMMARY, where conclusions derived from this thesis and their implications for future works are discussed.

CHAPTER 1

OPPORTUNITIES AND CHALLENGES OF BIOENGINEERING HUMAN TRABECULAR MESHWORK MODELS

1.1 Introduction

Glaucoma is a class of diseases that damage the optic nerve of the eye. According to the World Health Organization, glaucoma is a leading cause of blindness worldwide. In the U.S. alone, approximately 2.2 million people have glaucoma; of these, 120,000 are blind, accounting for 9% to 12% of all cases of blindness globally [1]. In addition, with the world's population aging, the number of people affected by glaucoma will likely increase dramatically. The main risk factor for glaucoma is increased intraocular pressure (IOP) [1], eventually leading to damage to the eye's optic nerve. IOP is controlled by the continuous inflow of aqueous humor (AH) and its continuous elimination (outflow) through two main pathways, the conventional and uveoscleral pathway. In humans, IOP is primarily controlled by the outflow of the AH through the trabecular meshwork (TM), also known as the conventional outflow pathway [14-17](Fig.1.1). The human trabecular meshwork (HTM) is an intricate three-dimensional (3D) structure, consisting of HTM cells and their associated extracellular matrix (ECM), including interwoven collagen beams and perforated sheets composed of elastin and collagen, arranged in a laminar pattern [14]. Glaucoma is thus linked to HTM structure and function where structural changes in the HTM likely affect tissue rigidity and biomechanical properties that in turn, influence its resistance to flow [18, 19].

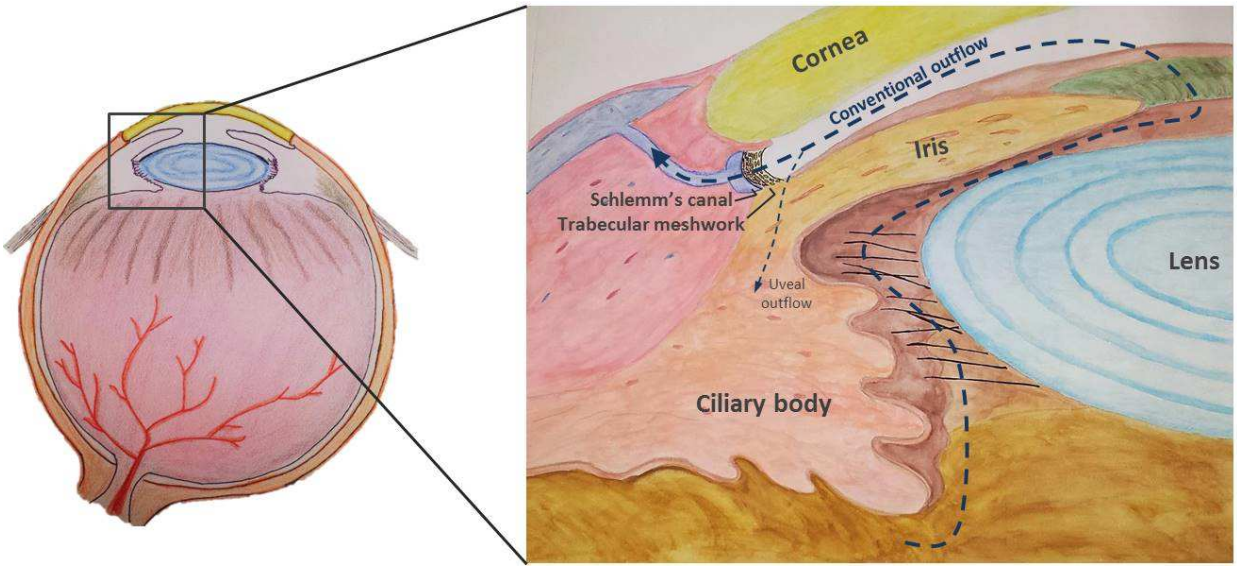

Figure 1.1. A schematic representation of the conventional and unconventional aqueous humor (AH) pathways. As indicated by the dashed arrows, the AH is produced in the ciliary body, after flowing through the posterior chamber, it fills the anterior chamber and exits via the conventional pathway (trabecular meshwork and Schlemm canal) or unconventional pathways (uveal outflow)

Current treatments for glaucoma involve lowering the IOP by means of decreasing AH production or increasing non-trabecular (uveoscleral pathway) AH outflow [20, 21]. Few therapeutic agents, however, target the HTM. Efforts to understand the physiology of the HTM have, over the years, provided some cues as to the pathology that leads to IOP elevation in glaucoma. While conventional HTM cell cultures are useful for studying the biology of HTM cells [2, 3], they are not suitable for evaluating the effects of medications on outflow facility [4-7]. Current outflow facility studies mainly rely on anterior segments of animal or human eyes [1, 8-12]; however, the preparation of these perfusion systems is cumbersome, and expensive, and not suitable for high-throughput screening [13]. Further advances in pharmacological treatment of glaucoma are, at this time, limited by the lack of proper, efficient, *in vitro* models for the screening of new, potential therapeutics [1]. Therefore, there is a great

need for a bioengineered, functional, *in vitro* HTM model for outflow studies and glaucoma drug screening. Such a model would advance the understanding of the HTM and provide a platform for future low-cost, novel studies related to the eye, facilitating drug discovery and effective treatment of glaucoma.

1.2. Glaucoma and Trabecular Meshwork

Glaucoma is a group of chronic, optic neuropathies in which damage to the optic nerve results in distinctive pattern of irreversible vision loss [22]. This major cause of blindness affects mainly older populations. In glaucoma, the neuro-retinal rim of the optic nerve becomes progressively thinner, thereby enlarging the optic-nerve cupping [23] (Fig.1.2). This phenomenon is caused by the loss of retinal ganglion cell axons along with supporting glia and vasculature. Glaucoma is classified according to anterior-segment variations that can elevate intraocular pressure (IOP). The anterior segment of the eye has a specialized circulatory system that, through the AH, allows the nourishment of crystalline lens and cornea. The AH is produced by the ciliary body and circulates through the anterior chamber of the eye, draining through the trabecular meshwork in the iridocorneal angle, which is the angle formed between the iris and the cornea [24] (Fig. 1.1). Elevation of IOP, which occurs in glaucoma, does not result from increased AH production, but rather from reduced aqueous outflow.

Over 70 million people have been diagnosed with glaucoma worldwide, and more than 4 million have vision loss in both eyes [25-29]. Glaucoma accounts for ~25% of new cases of blindness in developing countries [26, 30]. The risk factors associated with this disease include elevated IOP, age, genetic factors, race, thin corneas and

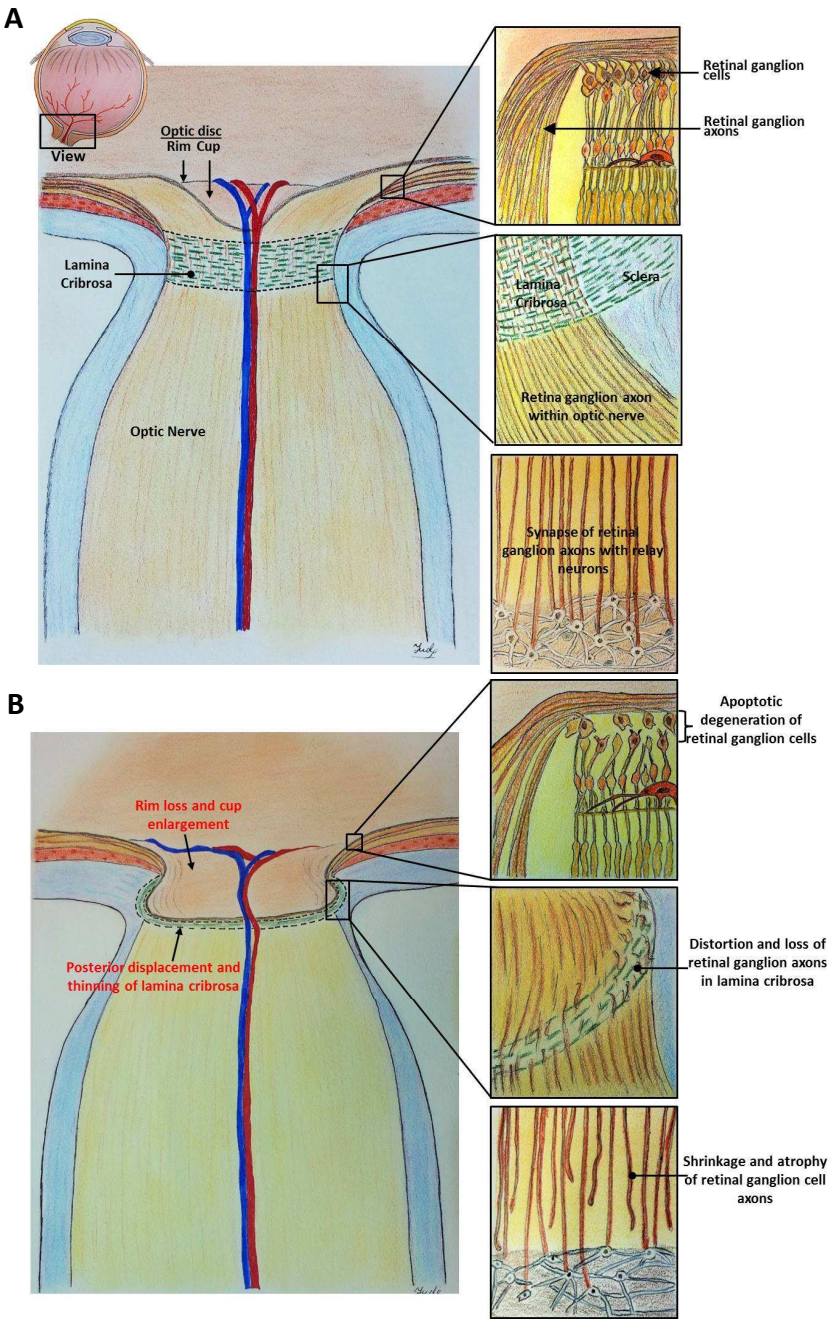

Figure 1.2 Schematic illustration of normal anatomy and neurodegenerative changes associated with glaucomatous optic neuropathy. (A) In the normal eye, the optic disc is composed of neural, vascular, and connective tissues. Retinal ganglion cell axons exit the eye through the lamina cribrosa (LC), forming the optic nerve. (B) Glaucomatous optic neuropathy involves damage and remodeling of the optic disc tissues and LC that lead to vision loss. With elevated intraocular pressure, the LC is posteriorly displaced and thinned, leading to deepening of the cup and narrowing of the rim. Distortions within the LC contribute to the blockade of axonal transport of neurotrophic factors within the RG cell axons followed by apoptotic degeneration of the RG cells. Strain placed on this region also causes molecular and functional changes to the resident cell population in the optic nerve (eg, astrocytes, microglia), remodeling of the extracellular matrix, alterations of the microcirculation and to shrinkage and atrophy of target relay neurons.

abnormal optic nerve anatomy [30]. It is estimated that up to 50% of those who currently suffer from glaucoma, are not aware that they have it [31] since glaucoma, in most cases, is asymptomatic and significant central vision is lost only once the disease is advanced. Currently, the only modifiable and preventable risk factor is increased IOP. Therefore, the proper and continual measurement of IOP can help in early diagnosis and treatment of glaucoma. If detected early enough, disease progression can be slowed with drugs and/or surgical treatment, underscoring the importance of identifying the disease in its early stages. The therapeutic management of glaucoma costs the United States and the United Kingdom respectively, ~2.5 billion and ~216 million dollars annually [32].

The types of glaucoma are classified by the appearance of the iridocorneal angle: open-angle and closed-angle. These are further divided into developmental categories as either primary or secondary type. In the primary, the cause of the disease is unknown while in secondary, the condition can be traced to a known cause such as injury, medication, inflammation or advanced cataracts. Primary open-angle glaucoma is the most common type of glaucoma. It occurs as both, an adult-onset disease, which occurs after 40 years of age, and as a juvenile-onset disease, which occurs between the ages of 3 and 40 years of age. For the purpose of this thesis, open-angle glaucoma, in which the iridocorneal angle is unobstructed and normal in appearance but AH outflow is diminished, will be the primary focus.

Primary-open angle glaucoma (POAG) usually affects both eyes and constitutes up to 85% of diagnosed cases. The elevated IOP observed in POAG usually results from decreased outflow of aqueous fluid from the eye, resulting in an imbalance

between the production and drainage of AH. Though not well understood, this elevation of IOP is believed to be due to changes that induce resistance within the TM. Among the potential TM changes are loss of trabecular endothelial cells, increased pigment accumulation, thickening or fusion of the trabecular lamellae, increased extracellular plaque material in the anterior chamber angle, and loss of ability of the endothelial cells lining the Schlemm's canal to form giant vacuoles [33]. The ongoing increase in IOP in the interior chamber subsequently exerts pressure posteriorly into the vitreous chamber. This pressure is relayed to the lamina cribrosa and suppresses axon transport and blood flow in the optic nerve bundle, resulting in damage, and ultimately death of retinal ganglion cells [34], leading to irreversible blindness (Fig. 1.2). Therefore, POAG has been directly linked to the TM structure and behavior (function), and current efforts towards the development of medications for POAG aim for TM modulation.

1.3. Biology of the Trabecular Meshwork

Elevated IOP is considered to be a causative factor in glaucoma [35] and is currently the only modifiable risk factor for this disease. Clinical trials have concluded that reducing IOP slows the onset and progression of glaucoma [21, 36], and therefore, all current treatments aim to reduce IOP either medically or surgically [37]. IOP is regulated primarily by adjustments of the outflow resistance at the trabecular meshwork (TM). Understanding the TM development, structure, and dynamics is imperative when attempting to understand the pathophysiology of POAG.

1.3.1. Development of the Trabecular Meshwork

The ocular drainage or outflow structures, the TM and the Schlemm's canal (SC), are located in the iridocorneal angle (the area where the iris and the cornea meet) of the anterior eye chamber [38]. The TM and SC are among the last structures to differentiate during anterior eye development. During the 5th week of embryonic development, the eye is composed of a rudimentary bi-layered optic cup formed from the forebrain neuroectoderm and of lens vesicles from the surface ectoderm [39-41] (Fig. 1.3A). At this developmental stage, mesenchymal progenitor cells, mainly of neural crest origin, loosely surround the developing eye and migrate anteriorly [39-44]. During weeks 15 to 20 of gestation, the iridocorneal angle is occupied by a dense mass of mesenchymal cells and shortly after begins iris elongation. These mesenchymal cells, by morphogenesis and differentiation, along with the peripheral region of the optic cup and overlying surface ectoderm, give rise to the cornea, iris and drainage structures, including TM and SC [39]. To form the TM, these mesenchymal cells elongate and flatten, becoming separated from each other by small openings partially filled with extracellular fibers. Despite both the TM and SC originating from periocular mesenchyme, the SC is formed as a result of vasculature remodeling (further described in section 1.3.2.) at the corneoscleral transition zone [40-42].

AH secretion begins later, after the TM appears [44-47]. Despite completion of the major morphogenesis of the TM around the time of birth in humans, significant development of the anterior segment's ocular drainage structures occurs in the postnatal period [41, 48]. After birth, the iridocorneal angle at the site of the TM is covered by a densely packed mass of mesenchymal cells that do not allow for the

proper outflow of AH or other physiological functions performed by fully developed TM (Fig. 1.3B). To induce a functional TM, maturation of these cells occurs as well as a major remodeling that forms intertrabecular spaces between a network of beams and sheets comprised of extracellular matrix (ECM). The early development of the TM and its direct interaction with AH is currently being exploited in attempts to direct stem cells into forming TM tissue [49, 50]. Tremendous progress towards that goal has been made but its clinical implications are as yet to be explored.

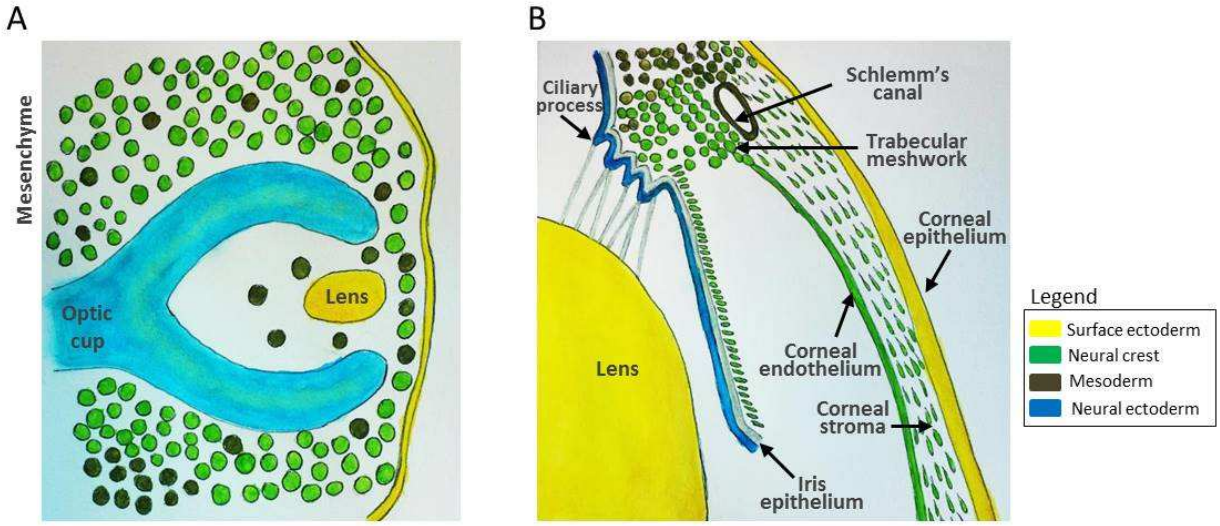

Figure 1.3. Schematic illustration of the embryonic and fetal development of the TM and SC. (A) Optic cup stage: at the 5th week of gestation, the surface ectoderm thickens and invaginates to form the lens pit and the optic vesicle forms the optic cup. (B) Maturation of a functional TM and SC postnatal.

1.3.2. Development of the Schlemm's Canal

SC has a mesodermal origin similar to the limbal vasculature in the eye [51]. The formation and major remodeling activities that give rise to the adult SC from blood vessels happen during the postnatal period [52]. Existing vessels penetrate to a location adjacent to the developing TM, these then connect/fuse with the TM and give rise to the SC [40]. During postnatal day (P)-1, the limbal vascular plexus (LVP) is complex and run completely around the eye, below the ocular surface [51]. Deep within the limbus, there is a vascular bed, known as radial vessels (RV), which run perpendicular to the LVP. Between these vascular beds, at the intermediate zone, the SC forms [51]. Signs of SC development are evident beginning at P-1 by endothelial

sprouts, emanating from the LVP and RV, penetrating into the intermediate zone (Fig. 1.4A). These sprout cells have characteristics similar to tip cells, with long filipodia [51] and resemble angiogenic remodeling. During P-2, these tip cells interact with each other using their filipodia and some macrophages are also seemed in the intermediate zone. The tip cells that will give rise to the SC (SC-tip cells) adhere and interlace with each other, giving rise to tip cell clusters (Fig. 1.4B).

At this point, not all of the cell clusters are directly connected to the LVP and/or RV. By P-3 and P-4, the clusters combine, forming a continuous flattened chain of cells that lack tubular morphology, and the number of these cells increases becoming more branched, resembling vasculogenesis [51] (Fig. 1.4C). At the end of P-4, some of these

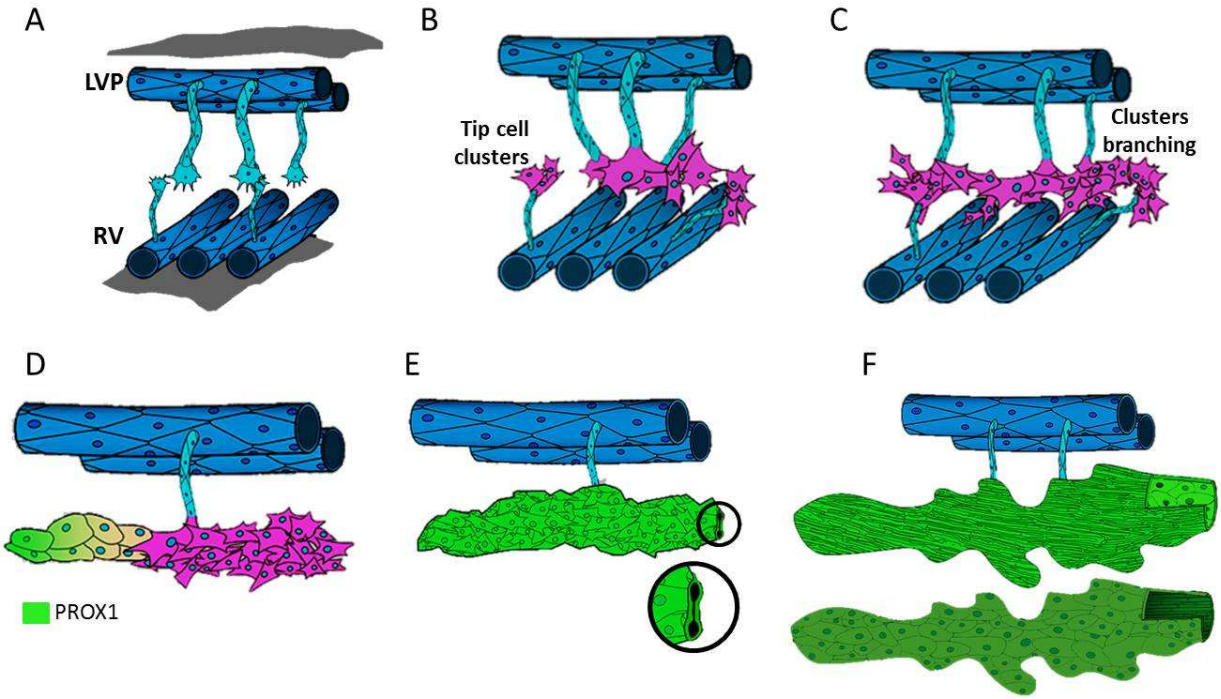

Figure 1.4. Schematic summarizing SC postnatal development. (A) During P-1, as in angiogenesis, sprouts led by tip cells penetrated the intermediate zone between LVP and RV. (B) By P-3 the number of tip cell clusters increases and they begin branching. (C) Some tip cells acquire lymphatic marker PROX1 at P-4. (D) Between P-10 to P-14, the inner lumen begins and form discontinuously between the SC's inner and outer wall. Outer wall cells become large and flat while those in the inner wall become thin and elongated. (E) By P-17, SC has its mature morphology. (F) By P15 to P17 SC presents mature morphology, with clearly distinct inner wall and outer wall cell. Adapted/modified from [50].

tip cells begin to express a few characteristic lymphatic markers such as prospero homeobox protein 1 (PROX1) [52] (Fig. 1.4D). By P-5, PROX1-expressing regions

remodel into a tubular structure with a flattened core, and cells continue proliferating. By P-9, almost all cells express PROX1. At P-10, lumen formation takes place, and cells that will comprise the SC outer wall lose PROX1 expression, while those that will become the SC inner wall become thin and elongated [51, 52] (Fig. 1.4E). By P-17, adult SC is evident as flat vessels running along the length of the limbus (Fig. 1.4F) and has a basement membrane with strong expression of collagen type IV secreted by these SC cells [53]. Despite the complicated and highly active development of the SC, its vascular beginnings, merging with the TM and AH flow dynamics that give rise to an adult SC, provide opportunities for bioengineering this tissue. Although stem cell-to-SC differentiation has not yet been achieved; given the mesodermal origin of the SC, other methods might be applied in order to induce SC-like phenotype and functions. Several attempts are currently in progress, and in the upcoming years, advances towards a successfully differentiated SC will likely be achieved.

1.3.3. Structure of the Trabecular Meshwork

The TM is a dynamic 3-D tissue that is composed of connective tissue beams, sheets, or lamellae covered by TM cells along with ECM. Cross sections of this tissue reveal a small porous triangular tissue approximately 350 x 50-150 μm. Three consecutive regions define the filtration portion of the TM: uveal meshwork, corneosleral meshwork, and juxtacanalicular region (also referred to as cribriform) (Fig. 1.5.). There is an additional region that is not involved in filtration, the insert region, attached under the cornea.

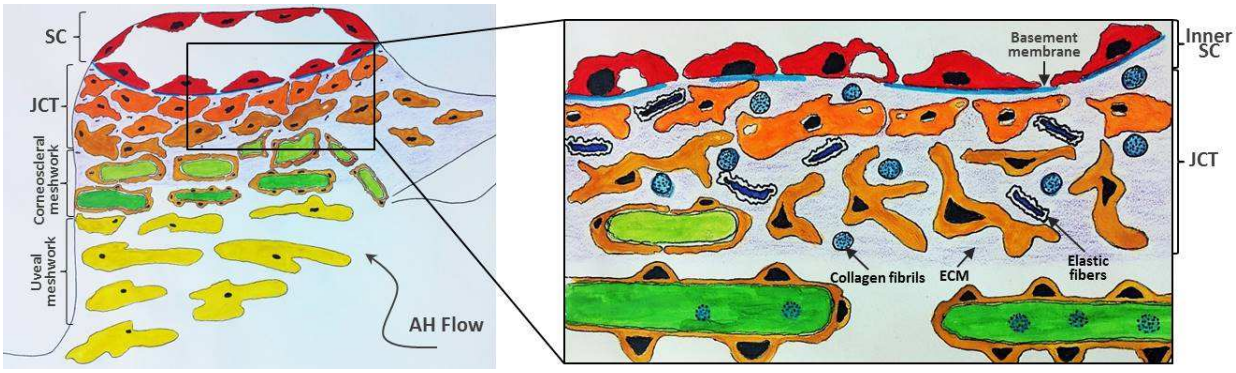

Figure 1.5. Schematic representation of the anatomy of the trabecular meshwork (conventional outflow tract). The arrow indicate the direction of the aqueous humor flow, from the anterior chamber toward Schlemm's canal. The different regions of the TM are the uveal meshwork, corneoscleral meshwork, juxtacanalicular or cribriform meshwork and Schlemm's canal. Aqueous humor flows through the intercellular spaces of the TM and crosses the inner wall of Schlemm's canal via two different mechanisms: an intercellular route and a transcellular route. Resistance to aqueous humor flow increases progressively from the anterior chamber to Schlemm's canal as intercellular spaces narrow. (Insert) Detailed schematic of juxtacanalicular or cribriform region and inner wall of Schlemm's canal endothelium.

The uveal meshwork extends from the iris root and ciliary body to the peripheral cornea [54]. It consists of approximately 2-3 layers of irregular net-like connective tissue beams that interconnect its different layers and are covered by flat TM cells that form irregular intratrabecular spaces [14, 16, 55-57]. These spaces are relatively large, often exceeded 100 μm in diameter [58] and therefore, this region provides little or no flow resistance [59]. The beams constituting this region are made up of collagens and elastin.

The corneoscleral meshwork extends approximately 100 μm in the flow-direction and is attached to the scleral spur posteriorly and to the inner aspects of the cornea anteriorly [16]. It consists of 8-15 layers of perforated/porous sheets of fibers or beams that are also covered by TM cells as in the uveal meshwork region, but here the intratrabecular spaces become smaller, with a structure that resembles a well-designed filter [60]. The beams and lamellae, described above, are only found in the uveal and

corneoscleral meshwork. Cells of the corneoscleral layer act primarily as pre-filters and are aggressively phagocytic [61], removing cellular debris from AH before the fluid moves deeper into the juxtacanalicular TM and the SC.

The deepest aspect of the TM is the juxtacanalicular region (JCT) also known as the endothelial meshwork or cribriform region. Significant evidence suggests that this region provides nearly all the resistance to AH outflow and appears to be involved in generating the elevated outflow resistance associated with glaucoma. This tissue is approximately 20-25 μm thick, and it extends from the last trabecular beam to the basement membrane of the inner wall of the SC [62]. Unlike the uveal and corneoscleral regions, the JCT is not arranged into lamellae structures, but instead it consists of loosely arranged ECM in which TM cells are embedded [14], forming a 2-5 cell layers structure within amorphous discontinuous connective tissue. This discontinuous connective tissue or disorganized ECM basement membrane [63-67] is composed of numerous proteogylcans, hyaluronan (HA), laminin, collagen type IV and fibronectin [14, 68-70] (Fig 1.5.insert). Networks of elastic fibers are also found in the JCT which allow expansion or recoil of this tissue in response to IOP fluctuations. These fibers are composed of elastin surrounded by an outer sheath of microfibrillar material [71]. The TM cells at the JCT are linked to one another and to the endothelial cells of the Schlemm's canal by long cellular processes [56, 57, 64, 72-75]. Additionally, TM cells are in contact with the ECM active molecules, which together, are believed to influence outflow resistance. Changes in the ECM environment and actin cytoskeletal are interrelated. Despite the large differences that exist between the uveal,

corneoscleral, and JCT regions, the only known differently expressed biomarker in the corneoscleral and JCT regions is αB-crystallin, a stress protein. [65, 76]

1.3.4. Trabecular Meshwork Outflow Function

A main function of the TM is to build up resistance to AH outflow in order to establish IOP. AH, produced by the ciliary body, fills the anterior and posterior chambers of the eye in front of the lens (Fig. 1). After filling the posterior chamber, the AH travels anteriorly across the lens and around the iris, then passes through the pupil to the anterior chamber [22]. The AH carries nutrients to the lens, cornea and TM [77]. It is the substitute for blood for the avascular structures in the eye, and given that the lens and cornea must remain transparent and clear, the AH also provides the right medium for light transmission in the eye [77]. The AH leaves the eye by either the conventional or unconventional (uveoscleral) pathway. Most of the AH is known to exit via the conventional route, while only about 10% leaves via the unconventional pathway [62, 78-81]. Flow through the unconventional outflow pathway is relatively independent of IOP [82]. Through the conventional outflow pathway, the AH moves down a pressure gradient from the TM across the inner wall of the SC by transcellular and paracellular routes.

The site that contributes to the most resistance within the TM is the JCT and the inner wall SC basement membrane [17, 63, 83, 84]. Before entering the SC, the tortuous paracellular spaces within the TM JCT dissipate most of the pressure, leaving a smaller pressure gradient across the SC inner wall. Ongoing ECM turnover within the conventional outflow tract (TM/SC) is required to maintain IOP and can modulate

outflow physiology [18, 63, 85-89]. In the inner wall of the SC, giant vacuoles and pores within the SC endothelial cells [90, 91] allow the flow of AH, which then enters the aqueous veins, and mixes with blood in the episcleral veins [92].

1.4. State-of-the-art Trabecular Meshwork Models

Understanding the biology and physiology of the TM is imperative for understanding the pathogenesis that leads to ocular hypertension, which in turn, can cause POAG. For over 50 years, scientists have worked towards developing diverse models to study different aspects of the TM and analyze potential IOP-lowering treatments. This section focuses on describing current model systems of the TM.

1.4.1. *In vitro* cell cultures

The metabolism and biochemistry of TM cells are believed to play an important role in the physiology of the conventional outflow tract. Primary cultures of cells isolated from the conventional outflow pathways of human donor or animal eyes have been useful to better understand the cellular mechanisms that contribute to the regulation of the AH outflow and IOP. Methods have been developed and are commonly used to specifically culture TM cells [93-96], and more recently, SC cells [97-100]. Cell cultures on glass or Transwell® membrane inserts with low porosity (5-15% porosity) or embedded in biopolymers [101] can be used to study a variety of cell activities, including contraction, phagocytosis, receptor activation, and messenger signaling. These *in vitro* models have allowed the identification of cell surface receptors that may participate in the conventional outflow regulation [102-106]. These models have also

been used to analyze the involvement of secreted ECM proteins and cell-ECM interactions on the conventional outflow tract [reviewed by [107]]. All of these studies have been critical for understanding molecular mechanisms of clinical IOP-lowering procedures for glaucoma or ocular hypertension, such as laser trabeculoplasty [108-110]. Although these *in vitro* models are simple and easy to maintain, they may not reflect *in vivo* conditions and most importantly, do not mimic the physiology of the TM or conventional outflow pathway.

1.4.2. *Ex vivo* models

The most common experimental method to study IOP regulation and the conventional outflow tract (TM/SC) are the *ex vivo* perfused anterior segments [61, 111-113]. Studies in this system can be conducted at constant perfusion rate while the pressure (IOP) is measured via pressure transducers. Additionally, constant pressure can also be maintained by modulating the flow rates, mostly gravimetrically. An important feature of this model is that perfused anterior segments mimic the homeostatic behavior of the TM by modulating outflow resistance in responding to pressure changes [63, 114]. This model, using healthy human tissue, allows for 2-3 week studies. However, human donor eyes are limited by their availability and high cost [115]. Perhaps more importantly, because desirable healthy human donor eyes are prioritized for corneal transplantation, those available for research are not of the best quality [115]. Therefore, organ segments from other species have also been used to study outflow physiology [115-119]. Although still expensive, animal organ segments used for perfused organ cultures are abundant and are more easily manipulated,

especially if utilizing larger animal eyes such as bovine. Despite these advantages, unlike human anterior segments, most animal eyes experience "washout effect" (phenomenon attributed to the wash away of plasma-derived proteins and ECM in animals' conventional outflow tract during the perfusion) which can increase outflow facility and skew the data [120-123]. At the same time, diverse animal species have different rates of AH formation than humans which affects the perfusion flow rates used in experiments [124]. Overall, *ex vivo* models provide better simulation of the physiological conditions than *in vitro* cell cultures and may require less time and cost than *in vivo* models, but they are still cumbersome, and hence, not suitable for high-throughput analysis of the HTM.

1.5. Opportunities of Micro-/Nanofabrication for Bioengineering Trabecular Meshwork Tissue Models

Classically, tissue engineering consists of isolating patient's specific cells and growing them on a biomimetic scaffold under controlled culture conditions; delivering the resulting construct to the desired site in the patient's body, and directing the new tissue formation into the scaffold that can be degraded overtime [125]. This approach relies on the innate capabilities of the cells/tissues to self-adapt. However, the natural capabilities of cells to adapt to any type of surroundings has limitations that hinder the optimum *in vivo*-like structure and behavior of various engineered tissues [126]. An example of such limitations is the lack of means to distribute oxygen and nutrients homogeneously, enabling functionality and viability of the construct [127]. In order to overcome this challenge and generate constructs capable of accurately

mimicking/replacing biological structures, novel scaffolds and devices have been developed, which can allow fine tuning of cellular position, organization and interactions [127]. Many of these novel scaffolds and devices benefit from advances in micro- and nanotechnology [128] (Fig. 1.6.).

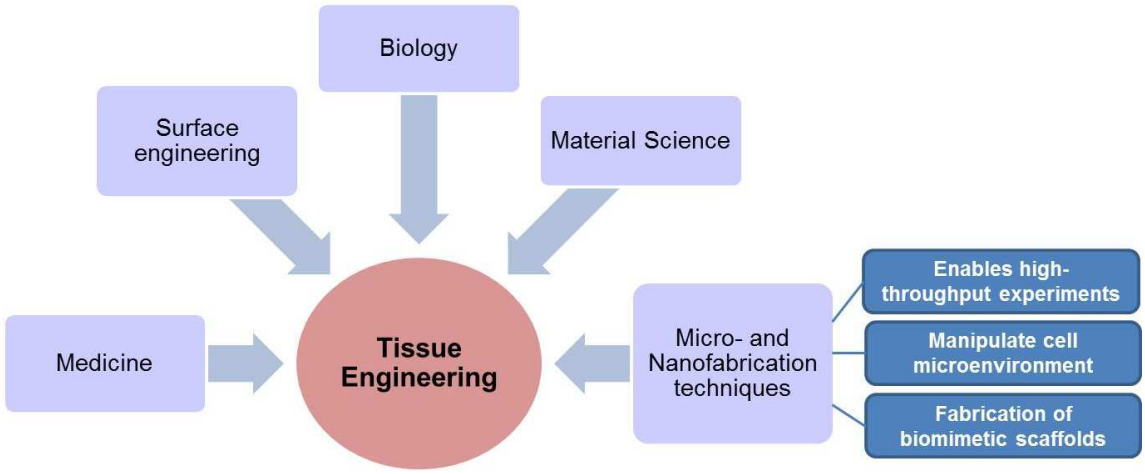

Figure 1.6. Schematic of different areas of expertise involved in current tissue engineering strategies. Tissue engineering involves diverse areas of science and is currently benefiting greatly from micro- and nanofabrication techniques.

Micro-/nanotechnology in tissue engineering and medicine is a rapidly growing scientific area, and has become a widely used method for biomedical applications [127]. Several groups have demonstrated that varying the (micro-/nano-) patterning and coating concentration/stiffness on the surface of scaffolds, can drastically change cell behavior [129-131]. Several requirements must be considered when selecting the appropriate micro-/nanofabricated scaffold material such as biocompatibility, mechanical and surface properties, transparency and potential coating factors that may better supplement biochemical cues for cells [128, 132-134]. With this knowledge, several areas of medicine have exploited the new methods developed by tissue

(biomedical) engineering as related to micro-/nanofabrication. Of interest to this dissertation, are the advances in ocular-tissue engineering with particular focus on the conventional outflow pathway. Despite the growing use of tissue engineering in areas such as trauma (bone-related) [reviewed by [135] and [136]], an integrated approach in the engineering of a healthy conventional outflow tract as an improved treatment and/or drug screening platform for glaucoma medications, still lags behind.

The unique ECM composition of the TM JCT and inner SC wall, along with their filtration requirements, suggests that micro-/nanotechnology could be used to recapitulate the microenvironment of the conventional outflow tract. Utilizing photolithographic techniques, highly structured and well defined features within the micro-/nanoscale range can be obtained from diverse polymeric materials [137]. Interestingly, TM cells modulate their phenotypical characteristics on different PDMS substrates patterned by soft lithography [4], demonstrating their responsiveness to their microenvironment. Additionally, given the HTM porous architecture covered by ECM proteins and populated by TM cells [58, 138], porous structures with the correct coating factors may allow the development of a bioengineered TM construct.

To date, there are very few attempts to bioengineer trabecular meshwork models. 3D polymer scaffolds, created by electrospinning nanofibers, have been used to enhance the microenvironment on which TM cells are seeded and to achieve more realistic measurement of hydraulic conductivity [139]. Utilizing soft lithography to prepare patterned structures, they further studied changes in HTM-marker expression as related to the topography of microstructures. Unfortunately, these studies have had very limited success and have proved impractical for physiological perfusion studies.

On the other hand, efforts to use natural 3D biopolymer scaffolds for *in vitro* modeling of the trabecular meshwork are currently in progress [101]. The model uses porcine TM cells and requires proper characterization of TM-marker expression, and perhaps most importantly, it needs to demonstrate proper construct function (outflow studies). Overall, these studies have demonstrated that bioengineering a more realistic HTM model is not an easy task and may require different tissue engineering approaches in order to develop a functional HTM model. Despite recent attempts, there is still an unmet need to successfully develop a functional bioengineered HTM construct that can facilitate biological and physiological studies in a more relevant environment than current *in vitro* models; such constructs should have higher-throughput capabilities and demonstrate *in vivo*-like characteristics.

1.6. Bioengineering Human Trabecular Meshwork on Micropatterned Microporous Scaffolds for Understanding of the Biology and Pathophysiology and Drug-screening of IOP-lowering Agents

To address the unmet needs of an *in vitro* HTM model to aid in understanding glaucoma pathology, drug screening, and glaucoma treatment, I propose to use well-defined, porous scaffolds with suitable biomacromolecular coatings for supporting HTM cells to mimic the structure and outflow physiology of the HTM. Such HTM-scaffold constructs could be used to study novel IOP-lowering treatments for glaucoma. The overall strategy to develop this model is to culture primary HTM cells on biocompatible, well defined, porous scaffolds that can support TM cells growth and proper fuction, for the purpose of recreating a 3D *in vitro* HTM complex. In order to validate our *in vitro*

HTM construct, the physical, biochemical and physiological properties, including outflow characteristics, will be studied throughout all experimental studies.

Current state-of-the-art *in vitro* models of the HTM cannot mimic the physiological behavior of the *in vivo* HTM, limiting their utility in predicting outflow regulation; making them impractical for drug screening. It is hypothesized that the proposed HTM construct will facilitate studies of HTM physiological responses, such as outflow resistance, to biochemical stimuli. Furthermore, it is hypothesized that our novel *in vitro* model could be used to study known and new cellular pathways that are involved in the regulation of the conventional outflow tract.

In order to test the hypothesis that the HTM can be recreated *in vitro* using microfabricated porous scaffolds and be used for the study of agents that induce or reverse the physiological condition elevated-IOP at the TM, the following studies have been performed as detailed in Chapters 2-5, respectively.

Study 1: Recreation of an in vitro HTM model on well-defined microporous scaffolds incorporated into a perfusion platform.

Study 2: Development an *in vitro* HTM steroid-induced glaucoma model to study cytoskeletal, ECM, and outflow resistance changes that induce increased IOP.

Study 3: Determination of the effects of TGFβ-2 and analysis of the potential anti-fibrotic properties of rho kinase inhibitors on the bioengineered *in vitro* HTM.

Study 4: Development of a novel 3D *in vitro* model of the conventional outflow tract utilizing co-culture and differentiation methods along with microfabrication techniques.

CHAPTER 2

Recreating the Human Trabecular Meshwork Outflow System using Microfabricated Porous Structures[1]

2.1 Introduction

The most recent statistics by the World Health Organization have placed glaucoma as a leading cause of irreversible blindness worldwide, affecting nearly 70 million people. In addition, with the world's population aging, the number of people affected by glaucoma will likely increase dramatically. Currently, the only treatment for glaucoma is lowering intraocular pressure (IOP), the only modifiable risk factor for glaucoma. IOP is determined by the continuous inflow of aqueous humor and its continuous elimination (outflow) through two main pathways: the classical and alternative pathway. In humans, IOP is primarily controlled by the outflow of the aqueous humor through the trabecular meshwork (TM), also known as the classical outflow pathway [14-17]. The human trabecular meshwork (HTM) is an intricate three-dimensional (3D) structure, consisting of HTM cells and their associated extracellular matrix (ECM), including interwoven collagen beams and perforated sheets composed of elastin and collagen, arranged in a laminar pattern [14]. Glaucoma is thus linked to HTM structure and function where structural changes in the HTM likely affect tissue rigidity and biomechanical properties that in turn, influence its resistance to flow [18, 19].

[1] Part of this chapter has previously appeared as: Karen Y. Torrejon, Dennis Pu, Magnus Bergkvist, John Danias , Susan T. Sharfstein, Yubing Xie. "Recreating a Human Trabecular Meshwork Outflow System on Microfabricated Porous Structures" Biotechnology and Bioengineering 110(12): 3205-18 (2013)

Current treatments of glaucoma involve lowering the IOP by means of decreasing aqueous humor production or increasing non-trabecular aqueous humor outflow [20, 21]. The compound latruncunlin-B (Lat-B) has recently gained interest as a potential novel glaucoma treatment as Lat-B increases aqueous humor outflow and decreases IOP [8, 9, 140]. Few therapeutic agents target the HTM and further advances in pharmacological treatment of glaucoma are currently limited by the lack of proper, efficient, *in vitro* models for the screening of new, potential therapeutics [1].

While conventional HTM cell cultures are useful for studying the biology of HTM cells [2, 3], they are not suitable for evaluating the effects of medications on outflow facility [4-7]. Current outflow facility studies mainly rely on anterior segments of animal or human eyes [1, 8-12]; however, the preparation of these perfusion systems is cumbersome and expensive, and not suitable for high-throughput screening [13]. Therefore, there is a great need for a bioengineered, functional, *in vitro* HTM model for outflow studies and glaucoma drug screening. Such a model would advance the understanding of the HTM and provide a platform for future low-cost, less invasive, novel studies related to the eye, facilitating drug discovery and effective treatment of glaucoma.

Building upon current knowledge of HTM morphology and physiology, microfabricated porous membranes of SU-8 were chosen as scaffolds to generate an *in vitro* HTM model. SU-8 is a biocompatible [141, 142], photo-definable epoxy and suitable for micropatterning high aspect-ratio structures using photolithography [143] that can be used for cell culture [144, 145]. SU-8 allows the design of a porous microstructure to support HTM cell layers, which can generate similar flow

characteristics as the *in vivo* HTM. To realize an *in vivo*-like pore structure and physiology, the effects of the pore size of SU-8 microstructures (7, 12 and 15 μm), biomacromolecular coatings (polylysine and gelatin), cell seeding density (1, 2 and 4 x 10^4 cells/cm^2) and culture duration were evaluated. Furthermore, HTM cell growth on the SU-8 scaffolds was compared to growth on commercially available, porous membranes. Subsequently, the bioengineered HTM was characterized for expression of HTM markers and secretion of ECM proteins, followed by functional analysis of outflow characteristics using a perfusion chamber with an integrated pressure transducer. Finally, the bioengineered HTM model was treated with Lat-B under controlled flow condition to test whether the *in vitro* 3D HTM model responds to this agent in a dose responsive manner and mimics the *in vivo* outflow physiology.

2.2. Materials and Methods

2.2.1. Materials

All chemicals were purchased from Sigma-Aldrich unless otherwise specified.

2.2.2. Human Trabecular Meshwork Cell Culture

Primary HTM cells, isolated from the juxtacanalicular and corneoscleral region of human eye, were purchased from ScienCell Research Laboratories (Carlsbad, CA). The HTM cells were initially plated in poly-L-lysine–coated 75 cm^2 cell culture flasks (2 μg poly-L-lysine/cm^2) and cultured in Improved MEM (Cellgro, Manassas, VA) with 10% fetal bovine serum (ScienCell Research Laboratories, Carlsbad, CA). Fresh culture medium was supplied every 48 hours. Cells were maintained at 37°C in a humidified atmosphere with 5% carbon dioxide until 80%-90% confluence at which point cells were

trypsinized using 0.25% Trypsin/0.5 mM EDTA and subcultured. After comparing the poly-L-lysine coating to gelatin for HTM cell growth, in all the subsequent experiments, HTM cells were subcultured on gelatin-coated 75 cm^2 cell culture flasks. All studies were conducted using cells before the 5th passage.

2.2.3. SU-8 Scaffold Fabrication

SU-8 2010 (MicroChem Corp., Newton, MA) was used to develop free-standing porous microstructures that served as scaffolds for HTM cell culture. SU-8 scaffolds with varying microstructure dimensions were fabricated using standard photolithography techniques (Fig. 2.1). First, a silicon substrate was cleaned using Piranha (3:1 H_2SO_4:H_2O_2) (H_2SO_4 was purchased from Transene Company, Danvers, MA and H_2O_2 from Puritian Products, Bethlehem, PA), rinsed with deionized water and then dried with nitrogen. A release layer of Omnicoat (Microchem, Boston, MA) was then spun on the wafer at 3000 rpm using a spin coater (Brewer Science, Rolla, MO), and baked on a hot plate at 200°C for 1 min. SU-8 2010 (Microchem) was applied by spin-coating to a final thickness of approximately 20 μm, then baked at 95 °C for 10 min, and cooled to room temperature. The resist was exposed through a mask containing the desired patterns using a 150 mJ/cm^2 dose on an EVG 640 I-line Contact Aligner (EV Group, Albany, NY). Finally, the substrate was baked at 95 °C for 10 min, cooled to room temperature, and placed in PGMEA developer (Microchem) overnight. The immersion of the substrate in PGMEA enabled the development and release of the SU-8 scaffolds from the substrate. The released, porous SU-8 scaffolds were then removed from the PGMEA solution, washed in acetone, and sterilized by soaking in 70% ethanol for 30 min.

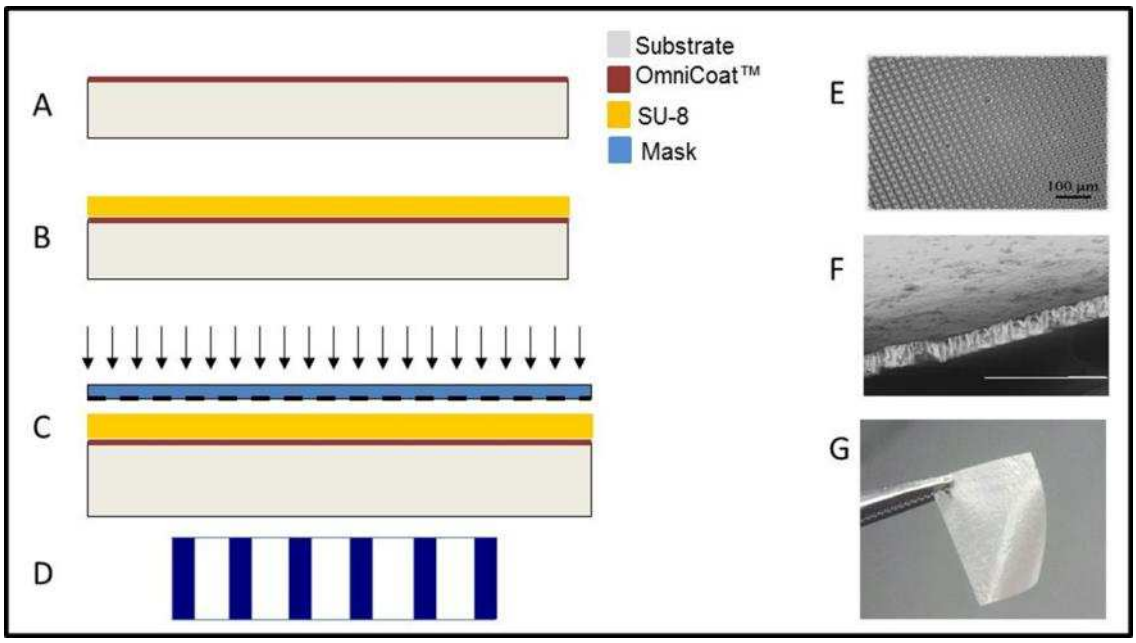

Figure 2.1. Schematics of the fabrication of the micropatterned, porous SU-8 scaffold using photolithography. (A) Omnicoat™ treatment on previously cleaned silica wafer for the release layer. (B) SU-8 2010 coating. (C) Exposure and post-exposure bake. (D) Development. Representative scanning electron micrographs of top view (E) and cross-section (F), and optical image (G) of the freestanding scaffold. (E and F) Scale bar = 100 µm.

2.2.4. Culture of Human Trabecular Meshwork Cells on SU-8 Scaffolds

SU-8 scaffolds were coated with poly-L-lysine or gelatin to promote HTM cell attachment by soaking in sterile solution of 10 mg/mL poly-L-lysine or 1% gelatin for 30 min, after which the scaffolds were removed and allowed to air-dry in a sterile tissue culture hood overnight. Aluminum-tape rings of 0.7 cm inner diameter and 1 cm outer diameter were cut, autoclaved and placed around the borders of the previously sterilized scaffolds. Reinforcing the microfabricated SU-8 membrane with an aluminum tape ring allowed the SU-8 scaffolds to rest at the bottom of a 24-well plate while preventing direct contact between the scaffold and the bottom of the plate; the ring also facilitated manipulation without handling cell-seeded scaffolds directly. HTM cells were seeded on the scaffold at various cell densities ($1x10^4$, $2x10^4$, $4x10^4$ and $5\ x10^4$

cells/cm^2) and cultured in Improved MEM (Cellgro) with 10% fetal bovine serum (ScienCell Research Laboratories). Cell growth was monitored by a Nikon inverted TS-100 F microscope (Micro Video Instruments, Avon, MA) every 48 hours for 14 days.

2.2.5. Culture of Human Trabecular Meshwork Cells on Commercially Available, Porous Membranes

Commercially available, porous membranes—polyester transwell inserts of 0.4 μm pore size (Corning Incorporated, Corning, NY) were coated with 1% gelatin for 30 min. HTM cells were seeded at 4 x10^4 cells/cm^2 and grown on these membranes for 9 days, compared with cells grown on gelatin-coated, 12-μm-pore SU-8 scaffolds and glass coverslips.

2.2.6. Scanning Electron Microscopy (SEM)

HTM cell morphology was characterized using a LEO 1550 field emission scanning electron microscope (SEM) (Leo Electron Microscopy Ltd, Cambridge, UK), 7 or 14 days after cultures were initiated. For SEM imaging, samples were fixed with 3% glutaraldehyde solution in 0.1 M phosphate buffer containing 0.1 M sucrose for 2 hrs at room temperature. The samples were then rinsed three times in 0.1 M phosphate buffer, dehydrated in a graded ethanol series and slowly infiltrated with a graded hexamethyldisilazane (HMDS)-ethanol series (25%, 50%, 75%, 100% HMDS) for drying [146]. Fixed samples were mounted on one-cm^2 stubs using carbon tape and were sputter-coated with ~5 nm gold-palladium to avoid charging the sample. Images were collected at a working distance of 3 mm with an acceleration gun voltage of 3 kV. The thickness of the HTM construct was determined in cross-sectional images using the incorporated digital annotation software.

2.2.7. Immunocytochemistry and Confocal Imaging

In parallel to the SEM studies, cells were fixed and stained for characteristic F-actin cytoskeleton and the presence of several HTM-specific markers, including α-smooth muscle actin (α-SMA) [147], myocilin [148, 149] and αB-crystallin [150]. After 14 days in culture, the cells grown on the SU-8 scaffolds were fixed with 4% paraformaldehyde, permeabilized with 0.2% Triton X-100, and blocked with 5% goat serum in PBS. HTM cells were subsequently incubated with Atto488-conjugated phalloidin (1:40) or primary antibodies: mouse anti-α-SMA, mouse anti-αB-crystallin and rabbit anti-myocilin (1:500) (Abcam, Cambridge, MA). Secondary antibody, goat anti-mouse Alexa Fluor® 594 (1:100, Invitrogen, Grand Island, NY), was used for the detection of α-SMA and αB-crystallin, and goat anti-rabbit Alexa Fluor® 488 (1:100, Invitrogen) was used to detect myocilin. These samples were further counter-stained with 4',6-diamidino-2-phenylindole (DAPI) to reveal cell nuclei. Laser scanning confocal microscopy was performed using a Leica SP5 confocal microscope (Leica Microsystems, Mannheim, Germany), and images were acquired at 63X magnification with an oil-immersion objective. Confocal images were processed using Leica LasAF software, and all confocal images within a given experiment were captured using the same laser intensity and gain settings in order to be able to compare intensities across samples.

2.2.8. Decellularization of ECM

After culturing on SU-8 scaffolds for 9 days, HTM-scaffold constructs were treated with 0.5% Triton X-100 for 30 min to removed cells and subsequently washed with PBS for three times. The decellularized ECM was fixed and chemically dried for

SEM observation of the ultrastructure. Additionally, samples were performed immunocytochemistry using antibodies against collagen IV and fibronectin (Abcam) and observed with confocal microscopy.

2.2.9. Perfusion Studies

A flow system apparatus for the controlled flow pressure measurement was constructed as shown in Figure 2.2., combining a perfusion chamber with an integrated pressure transducer (Edwards Lifesciences, Irvine CA). The SU-8 scaffolds with or without HTM cells were secured in the scaffold holder inside the perfusion chamber. This flow system allowed for simultaneous control of flow and measurement of the transmembrane pressure, enabling study of the outflow characteristics in our *in vitro* HTM model. Fourteen days prior to perfusion measurements, 4 $x10^4$ cell/cm^2 HTM cells were seeded on SU-8 scaffolds. At day 14, SU-8 scaffolds with a confluent layer of HTM cells were placed in the perfusion chamber and perfused at 2, 10 and 40 µl/min in the apical-to-basal direction for 24 hrs, with perfusion medium consisting of Dulbecco's modified Eagle's medium (DMEM) (Cellgro, Manassas, VA) with 0.1% gentamicin (MP, Solon, OH). The temperature was maintained at 34 °C. Back pressure was continuously monitored with a pressure transducer and recorded. For the treatment with Lat-B, once a stable baseline pressure was reached through perfusion of medium, samples were then perfused with 2 µM Lat-B in Hank's balanced salt solution (HBSS) (Cellgro, Manassas, VA) at the same constant flow rate and temperature for 4 hrs where samples perfused with 0.15% (v/v) DMSO in HBSS were used as control. Samples were fixed and stained for SEM and confocal image analysis as described above. Finally, the dose response of bioengineered HTM to Lat-B was examined by

perfusing with 0.2, 2 and 20 μM Lat-B in HBSS (Cellgro) at 40 μl/min in the apical-to-basal direction for 4 hrs and measuring the transmembrane pressure. Samples were fixed for SEM observation.

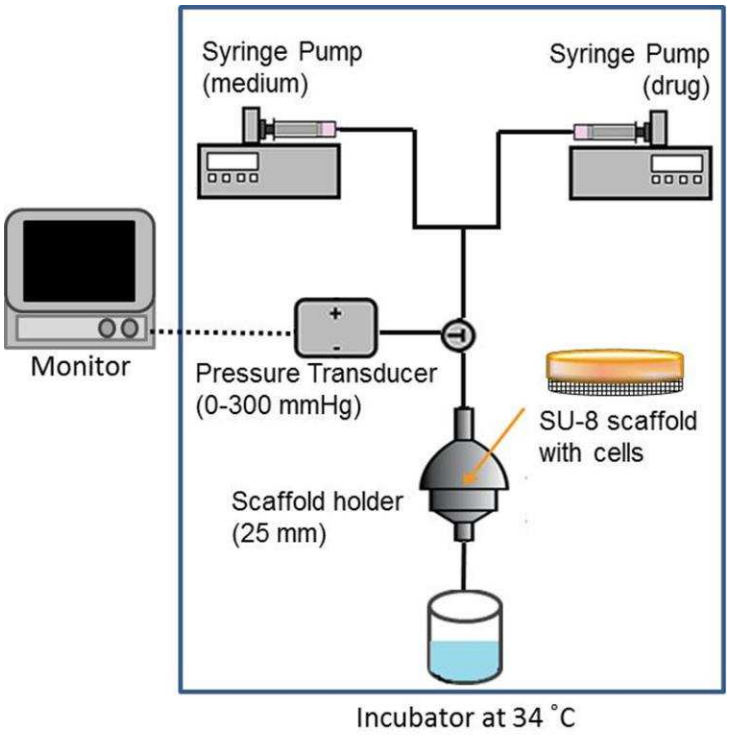

Figure 2.2. Diagram of the flow system constructed for perfusion studies.

2.2.10. Image Analysis

In order to quantitatively compare cell coverage of HTM cell growth on SU-8 scaffolds with various pore sizes at different seeding density, and to quantitatively describe the shape of nuclei and alignment of HTM cells, SEM and Phalloidin/DAPI stained confocal images were analyzed using the Adobe Photoshop CS5 Extended software. The area, perimeter, length, width, and directionality of DAPI-stained nuclei in purple were quantified. The length to width ratio was used to quantify the degree of elongation. The vector plot graph of directionality was drawn using Minitab v16.2.2 (Minitab Inc., State College, PA).

2.3. Results

2.3.1. Design and Evaluation of SU-8 Scaffold-based HTM Cell Culture System

To better recapitulate the perforated sheet-like structure and outflow characteristics of HTM, we fabricated freestanding, microporous SU-8 scaffolds. These scaffolds consist of arrays of square pores 7, 12, or 15 μm, with beam widths of 3.4 ± 0.1 μm, 7.3 ± 0.1 μm and 5.2 ± 0.1 μm ($p<0.05$), respectively. The pore sizes in these scaffold structures are close to the size of a single HTM cell. We noticed during our preliminary studies that HTM cells had difficulty growing into a confluent layer on larger pore-size microstructures and were unable to expand over the pores (data not shown). The thickness of these free-standing scaffolds was measured to be 20 μm through SEM analysis of cross-sectional micrographs.

SEM and light microscopy were used to evaluate the effects of biomacromolecular coating, initial cell seeding density, SU-8 pore size, and culture duration on HTM cell attachment and growth on SU-8 scaffolds. Towards the goal of mimicking the functional morphology of HTM, we expected the SU-8 scaffold-based culture system to promote HTM cell growth to form a confluent permeable TM in a laminar pattern.

Initial screening of coating factors (gelatin vs. polylysine) demonstrated that micropatterned SU-8 scaffolds coated with a thin layer of gelatin (5-10 nm as determined by ellipsometry on planar SU8 substrates) showed greater cell attachment and higher percentage of confluence after culturing for 10 days, and thus all scaffolds used in this study were coated with 1% gelatin prior to cell seeding. The effect of initial cell seeding density ($1x10^4$, $2x10^4$, $4x10^4$ and $5\ x10^4$ cells/cm^2) on HTM cell attachment

and growth on all SU-8 scaffolds was evaluated. When the cell seeding density was lower than 4 x 10^4 cells/cm^2, the cells exhibited poor attachment and growth (Fig. 2.3.A-C). The lowest initial cell seeding density that allowed confluent cell layer formation was 4 x 10^4 cells/cm^2 (Fig. 2.3D-F). Increasing the seeding density beyond 4 x 10^4 cells/cm^2 gave no noticeable improvement in cell layer formation (data not shown). Therefore, 4 x 10^4 cells/cm^2 seeding density was used for all subsequent studies toward construction of the in vitro HTM model.

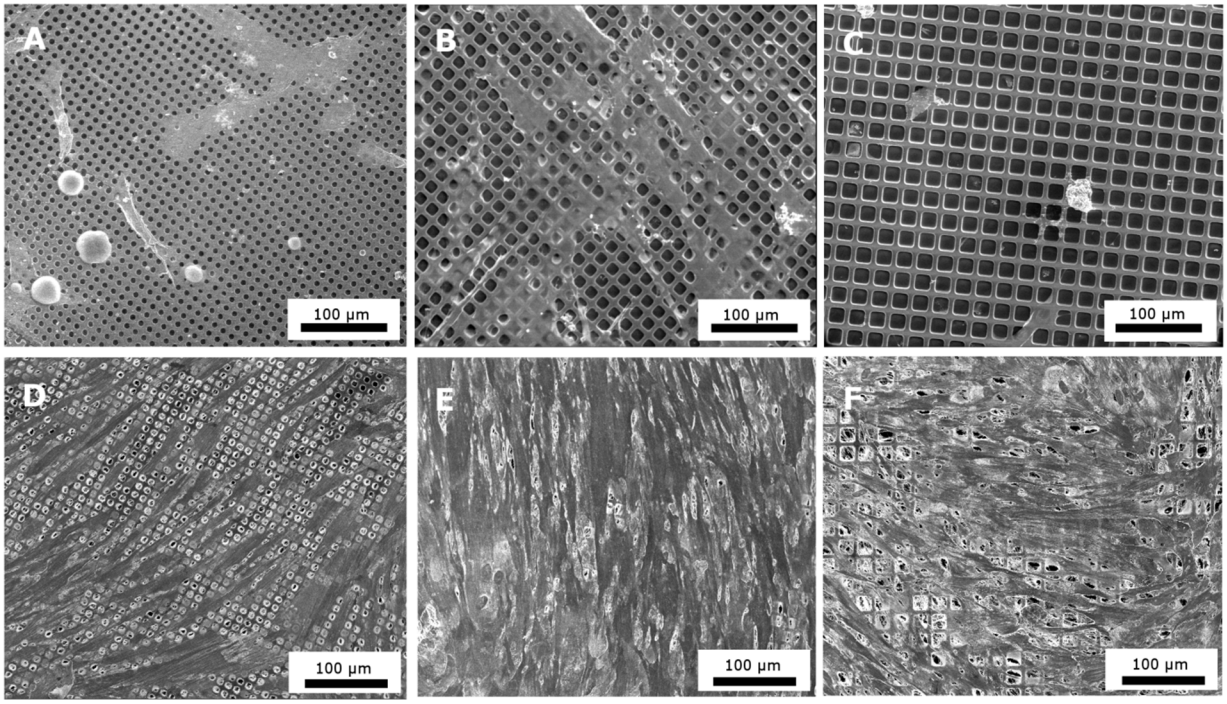

Figure 2.1. SEM micrographs of HTM cells grown on SU-8 scaffolds of different pore sizes for 7 days. (A-C) Seeding density of 1 x 10^4 cell/cm^2. (D-F) Seeding density of 4 x 10^4 cell/cm^2. (A and D) Pore size= 7 µm. (B and E) Pore size= 12 µm. (C and F) Pore size= 15 µm. Scale bar = 100 µm.

The effect of pore size (7, 12 and 15 µm) of SU-8 scaffolds on HTM cell growth was compared. By day 7, cells grown on the 7-µm-pore SU-8 scaffolds exhibited less cell coverage than the other two (Fig. 2.3D). HTM cells grown on 12-µm SU-8 scaffolds fully covered the pore spaces and began secreting their fibrillar, mesh-like ECM evenly

throughout the scaffold and between the cells as shown in Figure 3E. Cells grown on 15-μm SU-8 scaffolds showed larger gaps between cells and ECM than those grown on 12-μm-pore scaffolds (Fig. 2.3F). The effect of pore size on HTM cell attachment and growth was even more pronounced at the low cell density (1×10^4 cells/cm^2) where the 12-μm SU-8 scaffold provides the best cell coverage among all three pore sizes (compare Fig. 2.3B to 2.3A and C). Additionally, observation under light microscopy showed that fewer cells attached to the other two scaffolds compared to the 12-μm SU-8 scaffolds (data not shown). The effects of pore size of SU-8 scaffolds and cell seeding density on HTM cell coverage were quantified using Adobe Photoshop CS5 Extended (AP CS5E) software and are summarized in Table 2.1. Results showed that HTM cells at a seeding density of 4×10^4 cells/cm^2 grown on 12- μm SU-8 scaffold approximated 99% surface coverage after 7 days of cultivation.

Cell seeding density (cells/cm^2)	7 μm pores (%)	12 μm pores (%)	15 μm pores (%)
1×10^4	10	43	3
4×10^4	47	96	89

Table 2.1. Effects of pore size of SU-8 scaffolds and cell seeding density on surface coverage of HTM cells after culturing for 7 days

The effect of culture duration for HTM cells grown on 12-μm SU-8 scaffolds was further evaluated. Compared to 7 days of cultivation, cells grown for 14 days achieved greater coverage, appearing to reach full confluence (Fig. 2.4). In order to further assess whether an extended culture period could enhance cell-layer formation, HTM cells on SU-8 scaffolds were allowed to grow for 21 days. No apparent difference from the 14 day culture was noted through SEM or light microscopy observation (data not

shown). Additionally, HTM cells grown on the 12-μm SU-8 scaffolds exhibited representative characteristics of HTM cells such as a spindle-shaped appearance (Fig. 2.4A and C) and microvillus projections and overlapping cell processes (Fig. 2.4B and D). Based on the above findings, gelatin-coated 12-μm SU-8 microstructures were deemed to provide the most favorable scaffold, enhancing HTM cell growth and confluent meshwork formation, and chosen for further characterization.

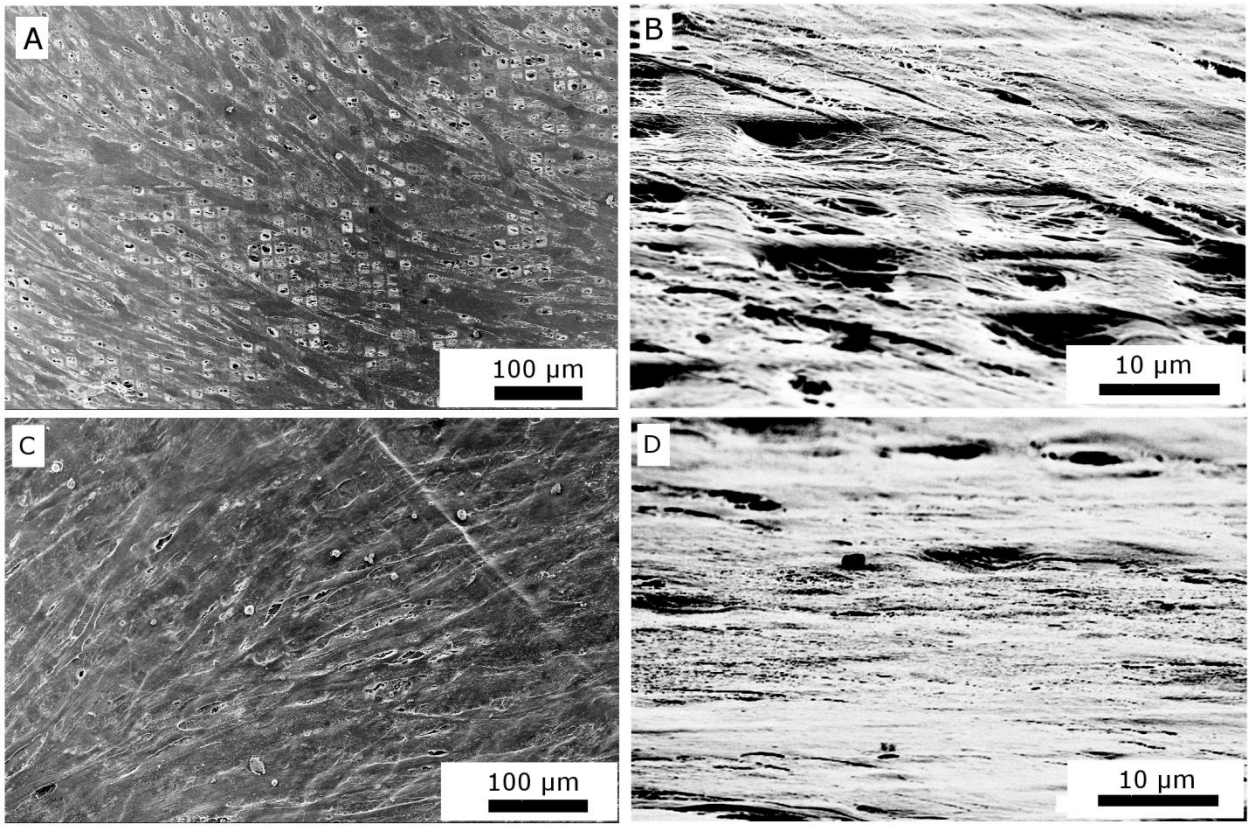

Figure 2.4. SEM micrographs of HTM cells grown on SU-8 scaffolds. HTM cells seeded on scaffold with a pore size of 12 μm for (A and B) 7 days and (C and D). 14 days (A) and (C) Scale bar = 100 μm. (B) and (D) Scale bar = 10 μm.

2.3.2. Comparison of HTM cells grown on well-defined SU-8 scaffolds with commercially available, porous membranes

After we demonstrated the feasibility of constructing an *in vitro* HTM model system by culturing 4 x 10^4 cells/cm^2 on gelatin-coated 12-μm SU-8 scaffolds, we

further compared this bioengineered HTM with cells cultured on commercially available, porous membranes. After 9 days of cultivation, HTM cells grown on porous membranes showed randomly oriented F-actin fibers (Fig. 2.5A). F-actin staining characterized the cytoskeleton of bioengineered HTM as containing partially elongated stress fibers, which also appeared to be aligned (Fig. 2.5B). The shape of nuclei was analyzed using AP CS5E software. The area, perimeter, length, width, length to width ratio of nuclei on these substrates are summarized in Table 2.2. The area and length of individual nuclei of HTM cells grown on well-defined SU-8 scaffolds is somewhat higher than those on porous membrane. However, the nuclear length to width ratio of HTM cells grown on SU-8 scaffolds was almost two-fold of cell nuclei grown on commercially available, porous membranes, indicating that SU-8 scaffolds supported more elongated nuclei. Additionally, the directionality of nuclei was quantified and graphed using Minitab v16.2.2 software (Fig. 2.5C). The vector plot demonstrated that HTM cells grown on commercially available porous membranes were more randomly oriented than bioengineered HTM on well-defined SU-8 scaffolds as seen by the narrower distribution of the samples from the SU-8 scaffolds (black) than the porous membranes (grey) (Fig. 2.5C). Compared to commercially available porous membranes, well-defined SU-8 scaffolds provide a more in vivo-like HTM structure (e.g., elongated nuclei, elongated actin stress fiber structures). Therefore, we focused on SU-8 scaffolds for the subsequent studies.

	Area (μm^2)	Perimeter (μm)	Length (μm)	Width (μm)	Length to width ratio
SU-8 scaffolds	125.9 ± 36.0	47.2 ± 6.6	18.2 ± 2.5	9.3 ± 1.9	**2.0**
Porous membranes	100.5 ± 40.8	42.9 ± 8.9	13.6 ± 3.9	12.2 ± 3.4	**1.1**

Table 2. Comparison of the shape of nuclei of Bioengineered HTM on SU-8 scaffolds with porous membranes

After culturing for 14 days, the phalloidin-stained F-actin fiber structures of bioengineered HTM showed even more alignment compared to 9 days (compare Fig. 2.5D with Fig. 2.5B). 3D confocal reconstruction by z-stacking of F-actin demonstrated that HTM cells grown on top of the SU-8 scaffolds formed a densely packed, 3D multiple-layer structure approximately 20 μm thick (Fig. 2.5E). A few cells were observed to grow inside the pores and to penetrate the sidewall of the SU-8 scaffolds. Additionally, cells that constitute the primary (basal) layer sent thin fibrous processes into the SU-8 scaffold (Fig. 2.5E middle image).

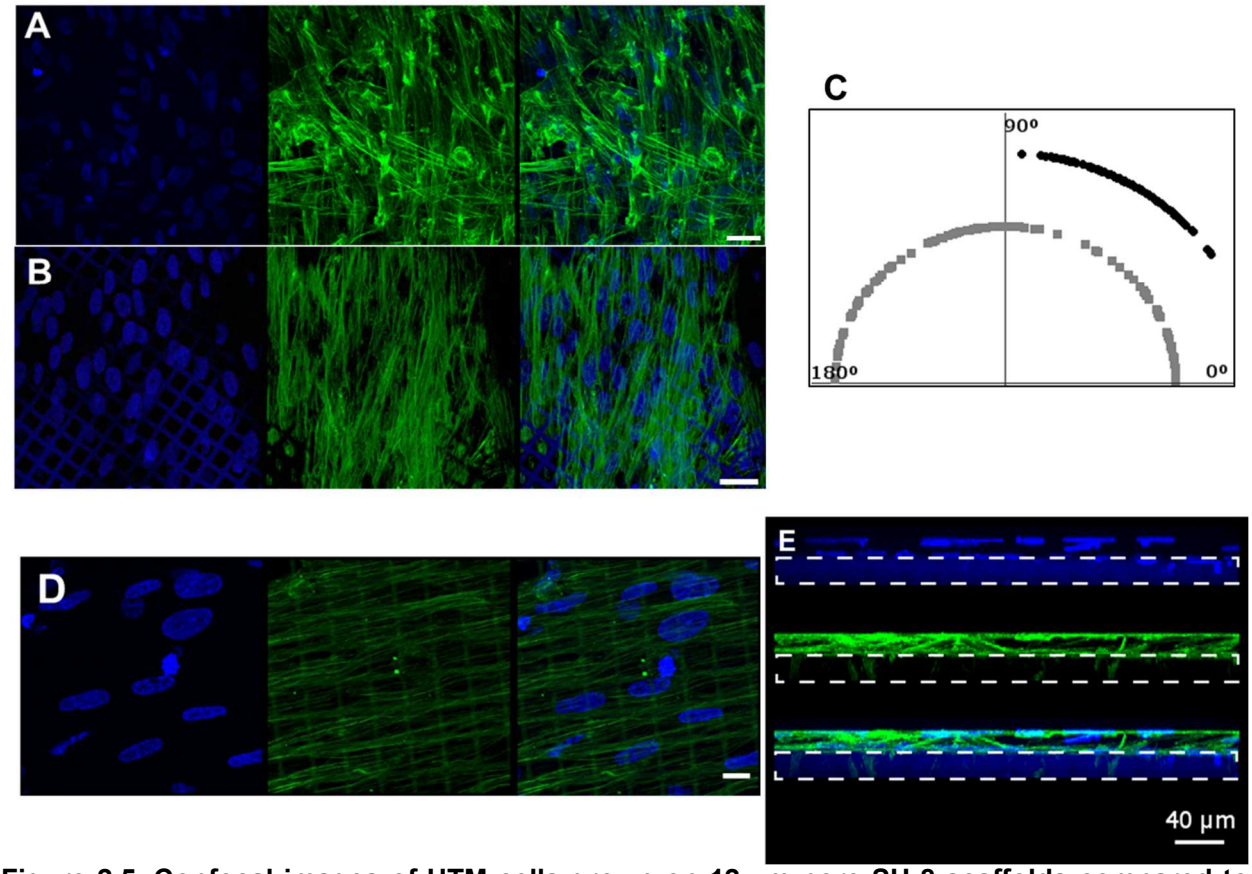

Figure 2.5. Confocal images of HTM cells grown on 12-μm pore SU-8 scaffolds compared to commercially available, porous membranes. Cells were costained with phalloidin and DAPI to visualize F-actin fibers in green and nuclei in blue. HTM cells grown on porous membranes (A) and SU-8 scaffolds (B) for 9 days. (C) Vector plot of cell nuclear alignment (Grey: porous membranes; Black: SU-8 scaffolds). (D) HTM cells grown on an SU-8 scaffold for 14 days. (E) Three-dimensional confocal reconstruction of HTM cells grown on an SU-8 scaffold. (Top panel) DAPI-stained nuclei in blue. (Middle panel) F-actin expression in green. (Bottom panel) Merged images. The SU-8 scaffold exhibits autofluorescence and is indicated by the dashed-line rectangles. Scale bar = 40 μm.

2.3.3. Biological Characterization of Bioengineered Human Trabecular Meshwork

Next, we confirmed HTM-specific gene expression in the bioengineered HTM using immunocytochemistry analysis followed by confocal imaging. Confocal images showed that HTM cells grown on SU-8 scaffolds expressed α-SMA (Fig. 2.6A), myocilin and αB-crystallin (Fig. 2.6B), suggesting that these cells maintained HTM-like expression pattern. Since the ECM of TM plays an important role in regulating aqueous outflow in both normal and glaucoma eyes [151], we further confirmed the secretion of relevant ECM proteins after HTM cells grew on SU-8 scaffolds. 0.5% Triton X-100 was used to remove HTM cells to obtain decellularized ECM. SEM imaging revealed the nanofibrous structure of densely packed ECM (Fig. 2.7A). In addition, we demonstrated via immunocytochemistry analysis that these HTM cells grown on SU-8 scaffolds secreted ECM that was enriched in collagen IV (Fig. 2.7B) and fibronectin (Fig. 2.7C).

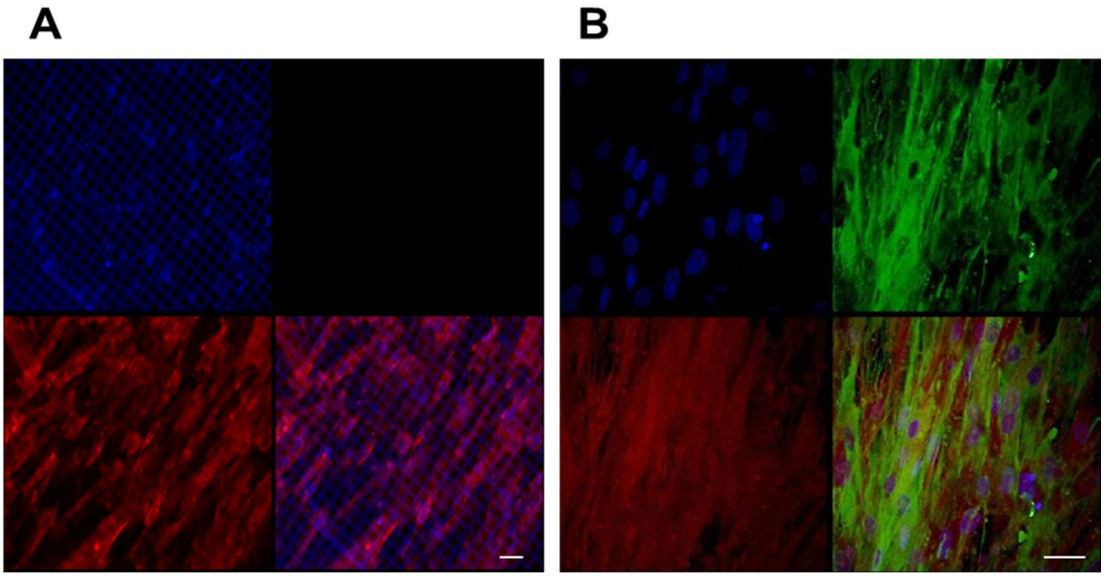

Figure 2.6. Confocal images of HTM cells grown on SU-8 scaffolds showing HTM marker expression. (A) Expression of α-SMA (in red). (B) Expression of αB-crystallin (in red) and myocilin (in green). Top left panel: DAPI-stained nuclei (in blue). Bottom right panel: Merged image. Dark panel: Unused channel. Scale bar = 40 μm.

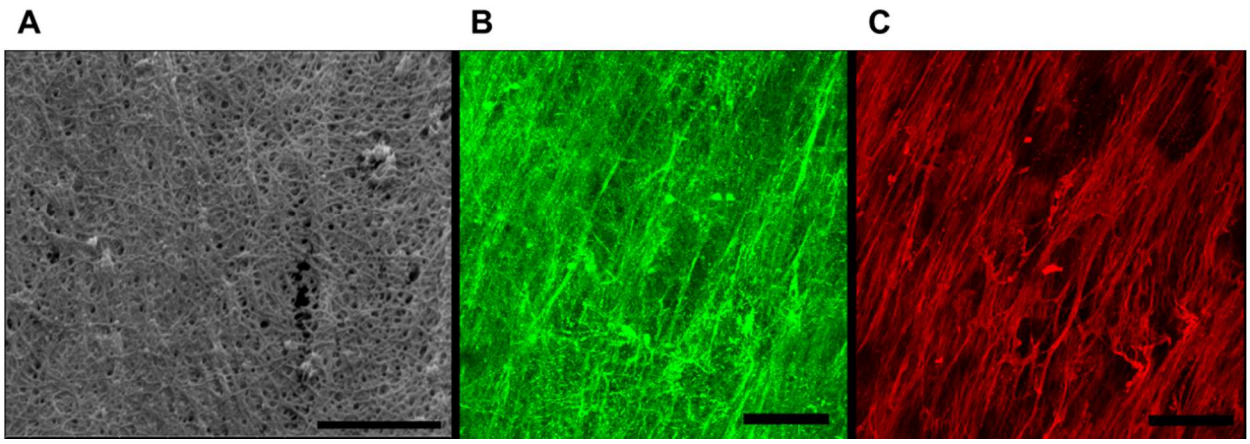

Figure 2.7. Decellularized ECM produced by HTM cells grown on SU-8 scaffolds. (A) SEM image. Scale bar = 1 μm. Confocal images showed the expression of collagen IV (B) and fibronectin (C). Scale bar = 40 μm.

2.3.4. Outflow Studies of Bioengineered Human Trabecular Meshwork

The fact that HTM cells grown on gelatin-coated 12 μm SU-8 scaffolds maintained an HTM-like cell phenotype prompted us to further evaluate the outflow facility of the bioengineered HTM using a flow apparatus as shown in Figure 2.2. The construct of HTM cells cultured on SU-8 scaffolds for 14 days was incorporated into a stand-alone perfusion chamber, where the pressure across the tissue construct was measured using an integrated pressure sensing system while maintaining a constant flow rate (40 μl/min). HTM cells provided flow resistance, raising the transmembrane pressure to 8 ± 1 mmHg, while SU-8 scaffolds alone (without HTM cells) had no significant resistance to flow (transmembrane pressure of 0.3 ± 0.5 mmHg). Pressure measurements at different flow rates (2, 10 and 40 μl/min) allowed for calculation of the outflow facility of the bioengineered HTM. The slope of the transmembrane pressure (P) vs. flow rate (F) curve was 0.21 mmHg/μL/min (Fig. 2.8A), and the outflow facility

(ΔF/ΔP), was calculated to be 0.135 µl/min/mmHg/mm^2 (0.131-0.141 µl/min/mmHg/mm^2 with 95% confidence).

2.3.5. Physiological Response of Bioengineered 3D HTM to Latruncunlin B

To further evaluate whether our system allows HTM cells to behave in a "physiologic manner", Lat-B was added to the perfusate at a concentration of 2 µM for 4 hrs. The mechanism of action of Lat B is reversible disruption of the dynamic process of actin filament maintenance, which affects the cytoskeleton of cells [152] through net actin depolymerization [153]. The transmembrane pressure of the bioengineered HTM decreased dramatically from 9.0 ± 1.0 mmHg to 0.6 ± 0.6 mmHg after Lat-B perfusion, indicating decreased flow resistance in HTM in response to Lat-B treatment (Fig. 2.8B). This pharmacological agent decreased the resistance to flow by 92 ± 6% (*N*=8, p<0.05).

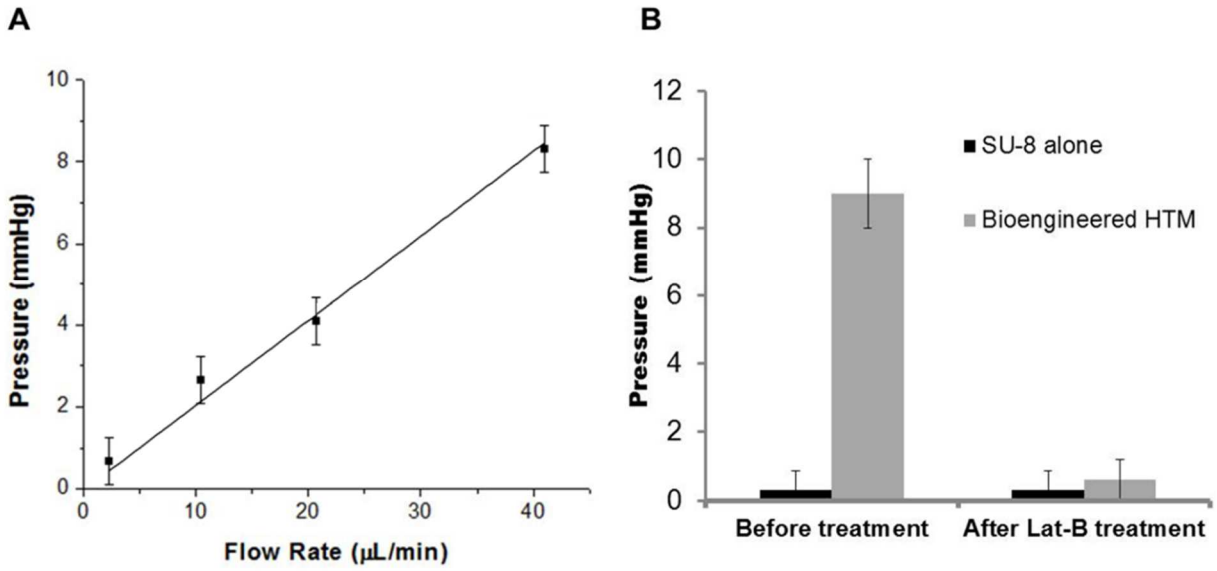

Figure 2.8. Outflow studies of the bioengineered HTM on SU-8 scaffolds. (A) Determination of outflow facility of the artificial TM through the relationship of transmembrane pressure and flow rate under perfusion. (B) Decreased resistance to flow in the bioengineered HTM in response to 2 µM Latrunculin B treatment.

Furthermore, Lat-B appeared to increase the outflow facility of our system by inducing shrinkage of HTM cells and disruption of secreted ECM (Fig. 2.9A-C). SEM images showed that HTM cells changed their morphology dramatically from an elongated spindle-shaped appearance to a square-like shape after Lat-B treatment. Additionally, thick fibrillose bundles of circular appearance were seen throughout the entire scaffold under SEM. Confocal images showed that elongated actin fibers (Fig. 2.9E and F) were disturbed and became punctate actin bundles after Lat-B perfusion (Fig. 2.9G), suggesting the critical role of actin filaments in maintaining HTM morphology and outflow physiology in our system. Additionally, confocal z-stack analysis revealed that after Lat-B treatment, the 3-D structure of the bioengineered HTM collapsed, with many cells collapsing into the pores of the scaffold (Fig. 2.10). To further investigate the normal recovery of HTM cells, perfusate was switched to 10%FBS-IMEM. Cells were allowed to recover for 3 days, after which samples were fixed and images, demonstrating that the actin disruption caused by Lat-B treatment can be reversible once the treatment is ceased. HTM cells recovered the elongated-spindled shape (Fig. 2.9D and H).

We also examined whether the bioengineered HTM had a dose-dependent response to Lat-B. After culture on SU-8 scaffolds for 14 days, HTM cells formed a confluent layer with extensive intercellular contacts and full cell coverage. These HTM-scaffold constructs were then perfused with 0.2, 2 and 20 μM Lat-B for 4 hours. The transmembrane pressure of the bioengineered HTM decreased from 9.0 mmHg (before treatment) to 2.5 mmHg (treated with 0.2 μM Lat-B), to 1 mmHg (treated with 2 μM Lat-B), or to 0 mmHg (treated with 20 μM Lat-B), respectively, indicating that the flow

resistance decreased with increasing in the dosage of Lat-B. SEM images showed distinct HTM morphology after Lat B treatment at various concentrations (Fig. 2.11A-C). The loss of filament integrity was dose-dependent (Fig. 2.11D-F). After perfusion with 0.2 μM Lat-B, HTM cells started to shrink and separate from neighboring cells while most of the cells were still elongated (Fig. 2.11A), showing partially uncovered SU-8 scaffolds (Fig. 2.11D). At 2 μM Lat-B, more HTM cells became rounded while ECM began to form fragments (Fig. 2.11B and E). When Lat-B was as high as 20 μM, HTM cells developed numerous cytoplasmic projections and the underlying ECM was disrupted (Fig. 2.11C), leaving large percentage of uncovered, clear SU-8 scaffold (Fig. 2.11F). Taken together, these results indicate a dose-dependent response of the bioengineered HTM to Lat-B.

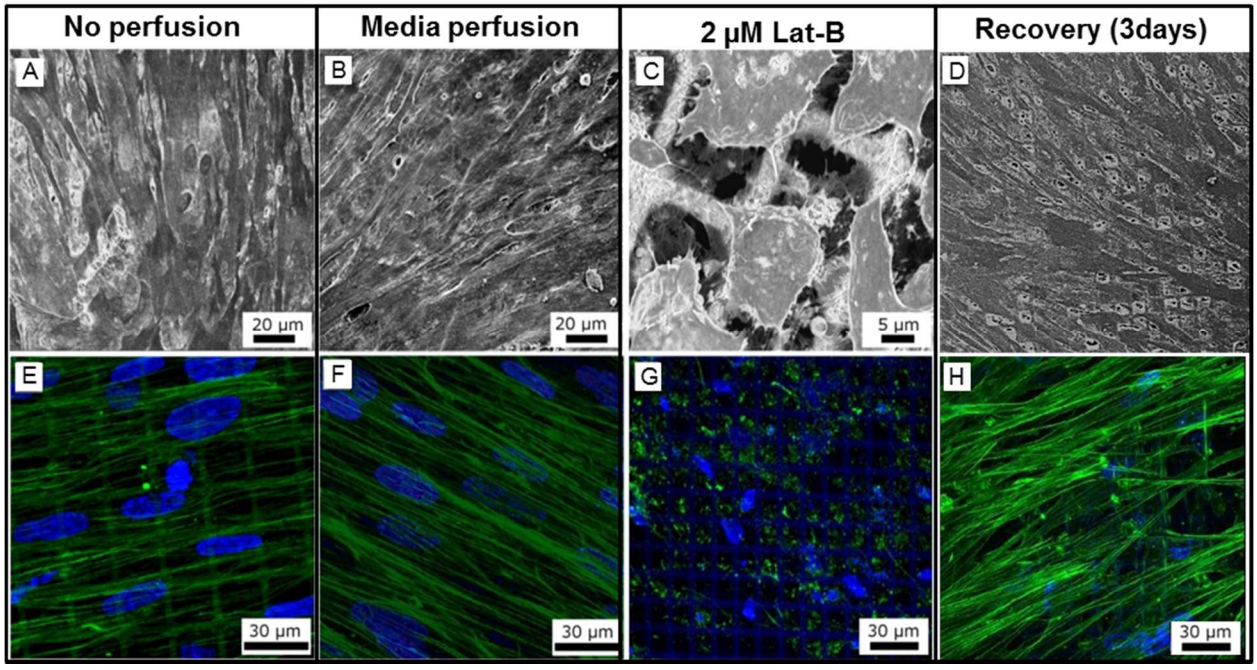

Figure 2.9. Biological response of bioengineered 3D HTM to 2 μM Latruncunlin B. (A-D) SEM micrographs of HTM cells grown on SU-8 scaffolds. (E-H) Confocal images of F-actin cytoskeleton in green and co-stained nuclei with DAPI in blue. (A and E) Before perfusion. (B and F) After perfusion with medium. (C and G) After perfusion with medium and Lat-B. (D and H) After 3 days of recovery from Lat-B treatment.

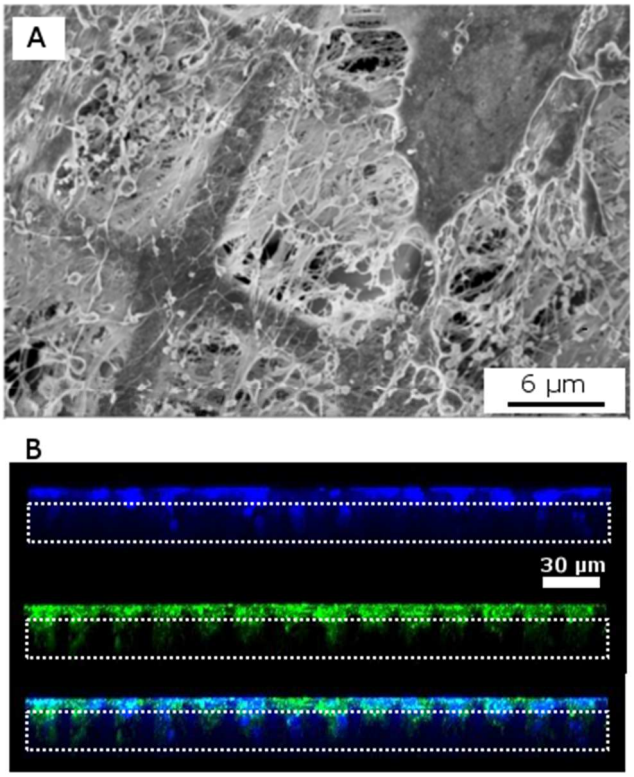

Figure 2.10. (A) SEM micrograph of bioengineered HTM complex after Lat-B perfusion. (B) Three dimensional confocal reconstruction of HTM cells grown on SU-8 scaffold after Lat-B perfusion. DAPI stained nuclei in blue (top), F-actin expression in green (middle), and merged images (bottom). The SU-8 scaffold exhibits autofluorescence and is indicated by the dashed-line rectangles.

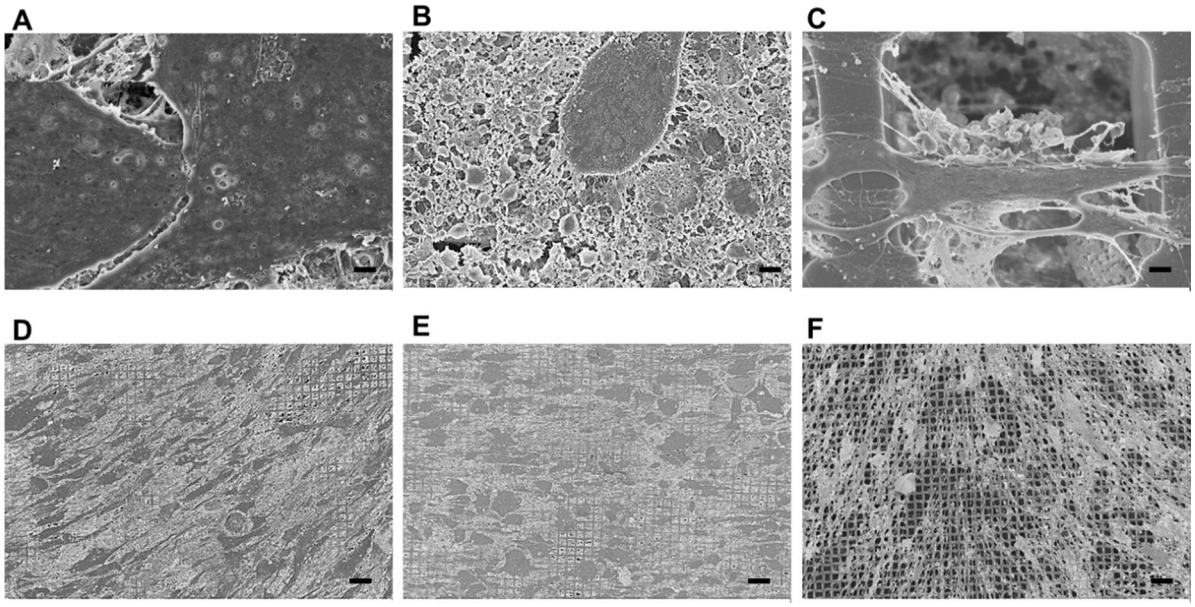

Figure 2.11. Effects of Latruncunlin B concentration on bioengineered 3D HTM. (A, D) 0.2 µM. (B, E) 2 µM. (C, F) 20 µM. (A-C) Scale bar = 1 µm. (D-F) Scale bar = 40 µm.

2.4. Discussion

In this study, we investigated the feasibility of using micropatterned, porous SU-8 scaffolds to support HTM cell growth into a trabecular meshwork that functions as an *in vitro* HTM model system for outflow studies. Conventional HTM cell culture on plastic tissue-culture surfaces is useful for fundamental studies of HTM biology [12, 97, 154-157]. However, it cannot be used for the investigation of outflow physiology. Commercially available, porous membranes were tried for HTM cell culture [158], but with limited success. This is because these membranes either possess irregular pore structures or have low porosity (i.e., 4-20%) which limits their performance for HTM cell growth and usefulness in perfusion experiments. To overcome these disadvantages, we have used photolithograpically defined SU-8 to achieve a highly porous membrane with pre-defined, well-controlled, uniform pore size, shape and beam width. We demonstrated that well-defined SU-8 scaffolds support a more in vivo-like HTM morphology than commercially available, porous membranes (Fig. 2.5).

SU-8 is a biocompatible, epoxy-based, negative tone photoresist [141]. It was selected as our scaffold material because of the following merits: it can be micropatterned into custom-designed microstructures using photolithography and reproducibly fabricate microstructures over a wide range of thicknesses [143, 159-167], it produces high aspect-ratio structures without collapsing [168], it can be used as cell culture substrate [144, 169], and it is transparent, allowing for easy monitoring of cell growth and behavior [144]. In addition to these practical considerations, the SU-8 scaffolds described in this work have great potential to be adapted into a high-throughput platform, which is essential for practical implementation of these scaffolds.

In conventional *in vitro* systems, cells are grown on a flat surface, only allowing monolayer growth of HTM cells [12, 154] . As shown in Figure 2.5E, our micropatterned SU-8 scaffold allows for multiple HTM cell layers to form, much like observed in the *in vivo* environment [17]. Previous SEM work has revealed the intricate microenvironment of the TM as a complex meshwork of pores, fibers, ridges, and other features of micro- and nano-scale dimensions [170]. Part of these microstructures seen in the *in vivo* TM include microsized pores formed by the net-like structure of trabecular beams [58], composed of 5-12 μm diameter fibers [171] that are covered by TM cells resting on their basal lamina [14]. In our study, the SU-8 scaffold with pore size of 12 μm and a beam width (spacing between two neighboring pores) of 7.3 ± 0.1 μm, which match the beam diameter found in vivo, gave rise to the highest HTM cell coverage among the conditions tested. 3D confocal reconstruction of the F-actin-stained artificial TM complexes described herein showed that HTM cells sent processes along the sidewall of the pores (Fig. 5E middle panel). These processes were also noted during SEM observations. The beam-width feature may provide specific topographic cues to the TM cells for their proliferation, 3-D multilayer growth, and ECM synthesis/secretion. Additionally the sidewall of the pore may allow HTM cells to sense a 3D environment, guiding 3D arrangement of the cell layers. Our results suggest that the 12-μm-pore scaffolds, in conjunction with the appropriate beam width used here, have enhanced cellular interactions, allowing formation of a 3D HTM complex.

An essential aim of this work was the construction of a permeable, drug-responsive HTM complex that can be used as a laboratory model to study aqueous outflow. Hence, we studied the responsiveness of our 3D culture system using a

perfusion chamber and a well-documented therapeutic agent, Lat-B [1, 8, 9]. During the perfusion experiment, treatment with Lat-B caused a marked drop in transmembrane pressure. SEM surface analysis of our fixed HTM complex after Lat-B perfusion showed bundles of material around contracted HTM cells. In addition to the bundles, large spaces between cells could be seen (Fig. 2.9C and Fig. 2.10), likely causing the drop in pressure. Further confocal imaging of F-actin staining of the HTM complex before and after Lat-B perfusion, showed disruption of the actin cytoskeleton of the HTM cells. Before Lat-B perfusion, long, polymerized actin fibers were observed, but after Lat-B treatment, many actin fibers appeared to have contracted and exhibited actin-dense spots (Fig. 2.9F). These observations lent further support that the punctate material observed in the SEM micrographs after Lat-B perfusion (Fig. 2.10) is partly comprised of concentrated actin depolymerized fibers, indicating that the polymerized actin fibers are an integral part of the formation of the 3-D structure of the bioengineered HTM complex, and that the depolymerization of actin causes the collapse of HTM complex. This observation is consistent with previous *in vitro* studies [140, 152], including perfusion studies of TM using Lat-B [8, 9, 153, 172], indicating that our bioengineered HTM model system is responsive to IOP-lowering drugs in a dose-dependent manner and can be used to study aqueous outflow *in vitro*.

The perfusion system implemented in this work allowed for calculation of outflow facility of the artificial HTM complex. Outflow facility provides insight into the ability of the HTM complex to resist flow under pressure. In our system, this resistance is created by the HTM cells themselves as well as the ECM they secreted; the SU-8 scaffold alone did not significantly resist flow. Although the outflow facility calculated in

our experiments is higher than actual outflow facility of perfused HTM [9] (0.135 µl/min/mmHg/mm^2 compared to 0.075 µL/min/mmHg/mm^2 *in vivo*), this discrepancy is expected. The *in vivo* HTM has a high level of complexity with multiple different cell layers, a significant amount of ECM, fibers and perforated sheets in addition to a different cross-sectional area, which as a whole contribute to the lower outflow facility found in the *in vivo* HTM. In addition, it is well known that a large part of outflow resistance *in vivo* is provided by the ECM of the juxtacanalicular area and the inner wall of Schlemm's canal [17, 173]. Although the value of the outflow facility of the current bioengineered HTM model is higher than that *in vivo*, it provides a valuable outflow system for investigating drug response to IOP-lowering agents that target HTM cells directly and for understanding the mechanism of drug action. This type of system may be implemented as a high-throughput platform for drug screening. We anticipate further incorporation of Schlemm's canal cells and manipulation of the properties of scaffolds will help achieve an improved artificial HTM that better reflects HTM physiology and thus provides an outflow facility value closer to the one measured in tissue.

We have successfully fabricated the microstructure of the SU-8 scaffold to support a characteristic HTM cell phenotype. Further development of this in vitro system has the potential to further mimic and control the nanoscale topography that is found at the extracellular connective tissue and basement membrane of HTM cells, possibly by including electrospun or self-assembled nanofibers composed of either natural or synthetic materials on top of the SU-8 scaffold. Synthetic surfaces with nanotopographic features have been shown to influence cell alignment, migration and gene expression

[4, 174-176]. The incorporation of nano-features onto the microstructure can provide HTM cells with additional topographic cues that would direct their behavior, allowing for a more *in vivo*-like TM complex. Additionally, the importance of substrate compliance on HTM cell mechanics and response to drugs (e.g., actin cytoskeleton disrupting agents) has been documented [6, 19, 153, 177, 178]. Together, the combination of the optimized scaffold described in this work and future nanostructured hydrogel environments that support growth and function of HTM cells could recreate a better *in vitro* HTM model system. To achieve a greater insight into how co-culture and structural design of scaffolds influence the biology and physiology of bioengineered HTM, work is currently underway to increase the structural and cellular complexity of our system. Additionally, to further validate the bioengineered HTM model system, we plan to test the effects of Rho-kinase inhibitors on flow resistance and outflow facility, a new class of IOP-lowering agents that are currently used in clinical trials for glaucoma and act specifically on TM [179].

In this study, we have confirmed the feasibility of using micropatterned, porous SU-8 scaffolds to construct an *in vitro* HTM model for investigation of HTM outflow physiology and response to biological agents. The geometry and surface treatment of the SU-8 microstructure influence HTM cell attachment, surface coverage and meshwork formation. The HTM constructs maintain a characteristic HTM phenotype as demonstrated by cell morphology, expression of HTM markers, ECM secretion and outflow facility measurement. The *in vitro* perfusion studies demonstrate that the 3D HTM is responsive to Lat-B treatment in a dose-dependent manner and confirm the central role of F-actin filaments in maintaining HTM morphology and outflow physiology.

This work provides an *in vitro* HTM model system to bridge structural and functional studies of the HTM, which will permit efficient and relevant analysis of novel glaucoma drugs.

CHAPTER 3

Steroid-induced Glaucoma Model of Bioengineered Human Trabecular Meshwork for Studying ECM Alterations and Cytokine Expression

3.1. Introduction

Glaucoma is a leading cause of blindness worldwide, affecting over 80 million people [26]. Given the world's aging population, cases of glaucoma are expected to increase rapidly over the next ten years. There is currently no cure for this disease. The only modifiable risk factor for glaucoma is elevated intraocular pressure (IOP). In the human eye, homeostatic IOP is maintained by formation and drainage of the aqueous humor, primarily through the human trabecular meshwork (HTM). Approximately 90% of the aqueous humor is drained through this tissue [180]. Therefore, understanding the glaucoma pathology at the HTM can give rise to novel therapies to treat this disease. Current research in the field is hampered by the lack of a realistic *in vitro* HTM-based model that can allow for more efficient and species relevant pathological outflow studies and/or drug screening.

The administration of steroids, such as glucocorticoids (GCs), used to treat inflammation either topically or systematically, has long been linked to primary open-angle glaucoma (POAG) [181-186]. In susceptible patients, steroids can lead to the development of ocular hypertension and POAG [181, 187-189]. If left untreated, these conditions can cause glaucomatous optic neuropathy, in turn leading to irreversible vision loss. Steroid-induced glaucoma is associated with morphological and biological

changes in the HTM *in vivo*, which in turn are believed to reduce aqueous humor outflow [190]. The morphological and physiological changes induced by steroids in the HTM bear resemblance to those seen in the pathogenesis of POAG. Among the most studied changes are (a) increase in extracellular matrix (ECM) deposition in the juxtacanalicular (cribriform region) [68], (b) decrease of intra-trabecular spaces [191], (c) induction of myocilin protein, (d) rearrangement of cytoskeletal elements [192-195], (e) inhibition of phagocytosis [196, 197] and (f) increase in outflow resistance. Since the HTM accounts for nearly 90% of aqueous humor outflow in the eye [198], changes in this tissue could have detrimental effects on homeostatic IOP. Rho-associated kinase (ROCK) inhibitors reduced IOP in several animal models by increasing aqueous humor drainage through the trabecular meshwork (TM) due to disruption of actin fibers [199, 200]. Several ROCK inhibitors are currently undergoing clinical trials as a potential new class of glaucoma drugs [201-203]. However, using ROCK inhibitors in combination with steroid-based anti-inflammatory agents to lower IOP is yet to be explored.

Although multiple *in vivo* animal models and *ex vivo* organ cultures, in addition to conventional 2D cell cultures, have been utilized to study effects of GCs on the TM, the field is lacking a species-relevant 3D *in vitro* model that allows for extensive studies pertaining to physiological outflow along with biological changes caused by steroids. Such a 3D *in vitro* model would further our current understanding of the pathology of steroid-induced glaucoma, and most importantly, could pave the path for the discovery of novel glaucoma targets. We have previously established a 3D HTM *in vitro* model that recapitulates the biological and physiological characteristics of HTM and behaves similarly to *ex vivo* organ cultures in response to IOP-lowering agents, e.g., latrunculin-B

(Lat-B) [204]. The ability to recapitulate the pathological changes could further strengthen this model and address the need of 3D glaucomatous HTM for biological and outflow studies, as well as drug screening.

We hypothesize that GC treatment of a bioengineered 3D HTM model could recapitulate steroid-induced glaucoma characteristics *in vitro* similar to that seen in susceptible humans with topical application of GCs. To test this hypothesis, we analyzed the effects of GC on bioengineered 3D HTM constructs, including myocilin expression, ECM deposition, cell morphology, phagocytosis, outflow resistance and outflow facility; demonstrating the ability of our model to be used as a powerful tool that could help unify the proposed mechanisms by which extended GC treatment induce glaucomatous HTM and hence, increase IOP. Furthermore, by analyzing HTM marker expression, ECM remodeling, and inflammatory cytokine gene expression, we investigated whether use of ROCK inhibitor in conjunction with steroid treatment could prevent the detrimental biological effects of steroids at the HTM by.

3.2. Materials and Methods

3.2.1. Primary Human Trabecular Meshwork Cell Culture

HTM cells were isolated from donor tissue rings discarded after penetrating keratoplasty. Isolation of the cells was performed under an IRB exempt protocol approved by the SUNY Downstate IRB. Isolation and culture conditions were as previously described [204] . Before use in experiments, all HTM cell strains were characterized by expression of αβ-crystalline and α-smooth muscle actin. HTM cells were initially plated in 75 cm^2 cell culture flasks with 10% fetal bovine serum (FBS)

(Atlas Biologicals, Fort Collins, CO) in Improved MEM (IMEM) (Corning Cellgro, Manassas, VA) with 1% 10mg/mL gentamicin. Fresh medium was supplied every 48 h. Cells were maintained at 37˚C in a humidified atmosphere with 5% carbon dioxide until 80-90% confluence. at which point cells were trypsinized using 0.25% trypsin/0.5 mM EDTA (Gibco, Grand Island, NY) and subcultured. At least three donors' human primary cell cultures were used during experiments. All studies were conducted using cells before the 5th passage.

3.2.2. Biomimetic Scaffold Fabrication

SU-8 2010 (MicroChem Corp.) was used to develop free-standing biomimetic porous microstructures that served as scaffolds on which primary HTM cells were cultured. Scaffolds were fabricated using standard photolithographic techniques as previously described [204]. Briefly; a release layer was spin-coated on the wafer and baked at 150˚C. SU-8 2010 was applied by spin-coating to final thickness of 5 µm, then baked at 95˚C and cooled to room temperature. The resist was UV-exposed through a mask containing the desired pattern, baked at 95˚C and developed in PGMEA developer (MicroChem Corp.) SU-8 scaffolds with the desired features were released from the substrate, washed with acetone and sterilized using 70% ethanol.

3.2.3. 3D Culture of HTM Cells on Scaffolds and PA treatment

To create 3D HTM constructs, 40,000 HTM cells were seeded on each microfabricated SU-8 scaffold in a well of a 24-well plate and cultured in 10% FBS-IMEM for 14 days. Medium was changed every 2-3 days. On day 14, 3D HTM constructs were serum- starved for 48 hrs and then treated with PA (Sigma Aldrich, ST.

Louis, MO) (3, 30, 300, 3,000 and 30,000 nM) or vehicle alone (0.1% ethanol) for 3, 6, or 9 days, as indicated. Out of the four donors' HTM cells being used, three were PA-responsive while one did not appear to be affected by PA. Hence three PA-responsive HTM cell strains were used for the remaining studies. After comparing the effect of PA concentration on selected protein expression, in all subsequent experiments, 3D HTM cultures on the scaffolds were treated with 300 nM PA, vehicle (ethanol), Y27632, or 300 nM PA/10 μM Y27632 (Sigma Aldrich).

3.2.4. Protein Extraction and Western Blot Analysis

To quantify secreted protein expression, medium samples were collected on day 3, 6 and 9 (500 μlof each sample) and concentrated 4X with centrifugal ultrafiltration columns (Centricon YM-10; Millipore, Bedford MA). Cellular proteins were extracted with radioimmunoprecipitation assay (RIPA) buffer (50 mM Tris-HCL, pH 7.5, 150 mM sodium chloride, 1% triton X-100, 1% sodium deoxycholate, 0.1% sodium dodecyl sulfate, 25 mM NaF, 0.1 mM sodium orthovanadate, 10 mM NaP4O7, 1 nM phenylmethyl sulfonyl fluoride) containing protease inhibitors (Complete Protease Inhibitor, Roche, Manheim, Germany) on ice. Proteins were quantified by bicinchoninic acid assay (Thermo Fischer Scientific). 25 μg of proteins from each sample were separated by SDS polyacrylamide gel electrophoresis on a 4-12% gel in MOPS running buffer (Life Technologies), transferred onto PVDF membrane and probed with antibodies against rabbit anti-myocilin(Sigma Aldrich), mouse anti-fibronectin, rabbit anti-collagen IV, mouse anti-αβ-crystallin and mouse anti-β-actin (Abcam) (Table 3.1.A). HRP-conjugated mouse or rabbit secondary antibodies (Invitrogen) were used. Bound antibody was detected using FluorChem E (Protein Simple). Protein expression was

analyzed by densitometry using ImageJ, and normalized to β-actin. All experiments were performed in triplicate for each of three donor cell.

A

Name	Specie	Dilution	Company	Secondary Antibody
Myocilin	Rabbit	1/200	Sigma Aldrich	HRP goat anti-rabbit
Collagen type IV	Rabbit	1/100	Abcam	HRP goat anti-rabbit
Fibronectin	Mouse	1/100	Abcam	HRP goat anti-mouse
β-actin	Mouse	1/200	Abcam	HRP goat anti-mouse
αB-crystallin	mouse	1/500	Abcam	HRP goat anti-mouse

B

Name	Specie	Dilution	Company	Secondary Antibody
Collagen type IV	Rabbit	1/200	Abcam	Goat anti-rabbit 488
Fibronectin	Mouse	1/200	Abcam	Goat anti-mouse 594
Laminin	Chicken	1/500	Abcam	Goat anti-chicken 633
Alexa-488 conjugated Phalloidin	-	1/100	Life Technologies	-
Myocilin	Rabbit	1/200	Sigma Aldrich	Goat anti-rabbit 488
αB-crystallin	mouse	1/200	Abcam	Goat anti-mouse 594

Table 3.1. Primary antibodies. Information of antibodies used for (A) western blot and (B) immunocytochemistry

3.2.5. Immunocytochemistry Followed by Confocal Microscopy

After 14 days in culture, 3D HTM constructs were serum-starved in 1% FBS and treated with 300 nM PA, 300nM PA/10 μM Y-27632, or vehicle alone for 9 days. 3D HTM samples were fixed, permeablized, and incubated with antibodies against HTM markers myocilin, and αB-crystallin, and ECM proteins, collagen type IV, fibronectin and laminin (Abcam) (Table 3.1.B), as described previously [204]. Laser scanning confocal microscopy was performed using a Leica SP5 confocal microscope, and images were acquired at 40 X and 63 X magnifications with an oil-immersion objective. Confocal images were processed using Leica LasAF software, and all confocal images within a given experiment were captured using the same laser intensity and gain settings in order to be able to compare intensities across samples.

3.2.6. Cytoskeleton Stain and Nuclear Size Analysis

3D HTM samples were fixed and stained for F-actin cytoskeleton using phalloidin (Life Technology) and co-stained with DAPI to reveal cell nuclei, followed by confocal imaging. Nuclei size measurements were done using ImageJ. Fifteen images from seven control samples and twenty images from eight PA-treated samples were used for nuclear size analysis.

3.2.7. Scanning Electron Microscopy

3D HTM samples were fixed, dehydrated and sputter-coated to prevent charging. Samples were observed under a LEO 1550 field emission scanning electron microscope (SEM) (Leo Electron Microscopy Ltd, Cambridge, UK) as described previously [204].

3.2.8. Phagocytosis Assay

Cultures of 3D HTM were challenged with E. coli conjugated to pHrodo green particles dyes (0.5 mg/well, Life Technologies) and incubated for 3 hours. These bioparticle conjugates are non-fluorescent outside the cell, but fluorescent at acidic pH in phagosomes. After the incubation, nuclei were stained with NucBlue live cell stain (Life Technologies) and cultures were imaged using fluorescence microscope. Fluorescence was quantified using a live-cell multi-plate reader (Tecan, Männedorf, Switzeland). All experiments were performed in triplicate using three donor cell strains.

3.2.9. Electric-Cell-Substrate Impedance Sensing

To measure the transcellular electrical resistance across 3D HTM constructs, Electric Cell-Substrate Impedance Sensing (ECIS®) [205, 206] (Applied Biophysics Inc., Troy, NY) was used. The SU-8 scaffolds on 6.5 mm filter inserts were inserted into an ECIS Trans-Filter Adapter for parallel measurement of up to 8 filters at a time and measured using ECIS Zθ (Theta) instrument. A non-invasive alternating current was injected and the complex impedance across the SU-8 scaffold between the bottom and top electrode was measured from which resistance can be extracted. Resistance was monitored at a frequency of 1000 Hz with a temporal resolution of 22 data points per h. The frequency of 1000 Hz was selected for monitoring as previous study of cell-covered and cell-free scaffolds showed a maximum resistance ratio at this particular frequency. (Figure 3.1.). Before starting measurement and after every medium change, SU-8 scaffolds were microscopically inspected for any possible defects as small holes would yield inaccurate measurements. Resistance of a cell-free filter in medium was about 100 Ω at 1000 Hz. HTM cells were cultured for 14 days on the scaffolds to create 3D HTM constructs before resistance was recorded (denoted as day 0). Medium was exchanged every 2 – 3 days, adding 300 nM fresh PA to the treated samples each time. On day 11 of PA treatment, 3D HTM constructs were treated with 10 μM Lat–B in order to reverse the effect of PA. Untreated samples were used as the controls. Experiments were run in quadruplicate, using three donors‘ cells.

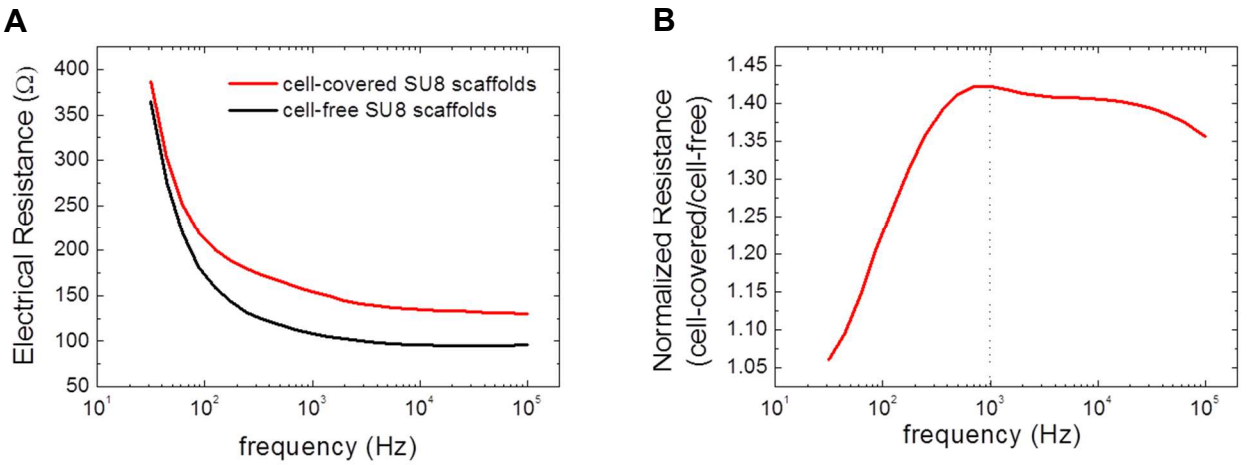

Figure 3.1. Frequency scan studies. (A) Electrical behavior of scaffold with and without HTM cells at various frequencies. (B) Electrical resistance across 3D HTM cell layers on scaffolds is greatest at 1000 Hz.

3.2.10. Perfusion Studies

A perfusion apparatus was used as previously described [204]. After at least 7 days of PA treatment, samples were securely placed in the perfusion chamber and perfused at various rates for 6 hrs per flow rate (2, 10, 20 and 40 µl/min). Samples were perfused in an apical-to-basal direction with perfusion medium consisting of Dulbecco's modified Eagle's medium (DMEM) (Cellgro) with 0.1% gentamicin (MP) containing 300 nM PA. The temperature was maintained at 34˚C. Pressure was continuously monitored and recorded. After perfusion, samples were fixed and stained for SEM or confocal imaging. The "outflow facility" of our bioengineered 3D HTM model, Δflow/Δpressure, was calculated from the inverse of the slope of the pressure versus flow graph per unit surface area. Twelve different samples per condition including HTM cells from three donors were studied under perfusion.

3.2.11. Quantitative Real-time PCR (qPCR) analysis

Total RNA was extracted from samples cultured for 3, 5, and 9 days with or without PA treatment using an RNeasy Plus Mini kit (Qiagen Inc., Valencia, CA). RNA concentrations were determined using a NanoDrop spectrophotometer. 20 ng of RNA per sample was used for each qPCR experiments. qPCR was carried out using TaqMan RNA-to-CT™ 1-Step Kit (Applied Biosystems, Carlsbad, CA) and performed on an AB StepOnePlus Real Time PCR system (Life Technologies, Carlsbad, CA) using primers for MMP2, MMP3, IL-1α, TIMP-1 and TGFβ (Table 2).The temperature profile was as follows: 48˚C for 15 min (reverse transcription step), followed by an enzyme activation step of 95°C for 10 min, 40 cycles of 15 s denaturation at 95°C and 1 min anneal/extend at 60°C. Relative quantitation data analysis was performed using the comparative quantification method, ΔΔCt, with GAPDH as the endogenous reference. All samples were normalized to the vehicle-treated controls. q-PCR experiments were performed in triplicate (technical replicates) and from duplicate biological experiments using three donor cells. Average values are presented as mean ± SD.

NCBI Gene symbol	Ref. Sequ. number	Forward Primer	Reverse Primer
MYOC	NM_000261	ATCCACACACCATACTTGCC	CTGCTTCCCGAATTTTGAAGG
COL4A1	NM_001845	CCTTTGTGCCATTGCATCC	GAACAAAAGGGACAAGAGGAC
FN1	NM_054034	GTCCTTGTGTCCTGATCGTTG	AGGCTGGATGATGGTAGATTG
MMP2	NM_004530	CCAAGGTCAATGTCAGGAGAG	GCACCCATTTACACCTACAC
MMP3	NM_002422	TGAGTGAGTGATAGAGTGGT	TGAACAATGGACAAAGGATACAAC
TIMP1	NM_003254	GCTTGGAACCCTTTATACATCTTG	CCTTCTGCAATTCCGACCT
IL1A	NM_000575	AGTTCTTAGTGCCGTGAGTTTC	GTGACTGCCCAAGATGAAGA
TGFB2	NM_003238	ACTTTGCTGTCGATGTAGCG	GCAGAGTTCAGAGTCTTTCGT
GAPDH	NM_002046	TGTAGTTGAGGTCAATGAAGGG	ACATCGCTCAGACACCATG

Table 3.2. qPCR primers

3.2.12. Statistical Analysis

Data were expressed as the average ± standard deviation. Student's t-test was performed for nuclear size analysis and phagocytosis assay. The difference between controls, PA-treated, and PA/ Y-27632-treated 3D HTM samples was analyzed using two-way ANOVA followed by Bonferroni post-tests (GraphPad Prism 6.02; GraphPad Software, Inc., La Jolla, CA). P values $P<0.05$ and $P<0.001$ considered significant and highly significant, respectively.

3.3. Results

3.3.1. Glucocorticoid-Induced Glaucomatous Expression of Myocilin and ECM Proteins in 3D Human Trabecular Meshwork Model

To engineer an *in vitro* HTM model that recapitulates the pathology of steroid-induced glaucoma, we used photolithographic techniques in combination with 3D cell culture of primary HTM cells followed by long-term GC treatment. We chose prednisolone acetate (PA) as a model steroid, which is a frequently used ophthalmic (inflammatory) steroid drug. We began by creating a biomimetic SU-8 scaffold using photolithography. The microfabricated, well-defined, porous scaffold was previously shown to support growth and proliferation of primary HTM cells in an architecture that mimics the biochemical and outflow environment of the HTM *in vivo* [204]. As described previously, primary HTM cells were isolated from normal human donors and characterized for expression of myocilin, αB-crystallin and α-smooth muscle actin [204]. Primary HTM cells were seeded on gelatin-coated SU-8 scaffolds and cultured for 14 days, which has been optimized to recreate the HTM morphology and outflow physiology [204]. We next examined the concentrations of PA, which could induce changes in protein expression, e.g., induced myocilin and increased ECM proteins, characteristics seen in patients with steroid-induced glaucoma. We first analyzed intracellular and secreted protein expression of myocilin, fibronectin and collagen IV in our model after static treatment with concentrations of PA ranging from 3 nM to 30 μM for over 9 days. A maximum response was observed at a GC concentration of 300 nM PA for these proteins, most notably for intracellular and secreted myocilin and fibronectin (Fig. 3.2. A and B). Additionally, 300 nM PA significantly increased levels of

both intracellular and secreted fibronectin (P<0.01 and P<0.001, respectively) and myocilin (P<0.001 and P<0.05) as well as secreted collagen IV (P<0.001). Therefore, we used 300 nM PA for the remainder of these studies (Fig. 3.2.).

Changes in myocilin and ECM protein expression after perfusion were confirmed

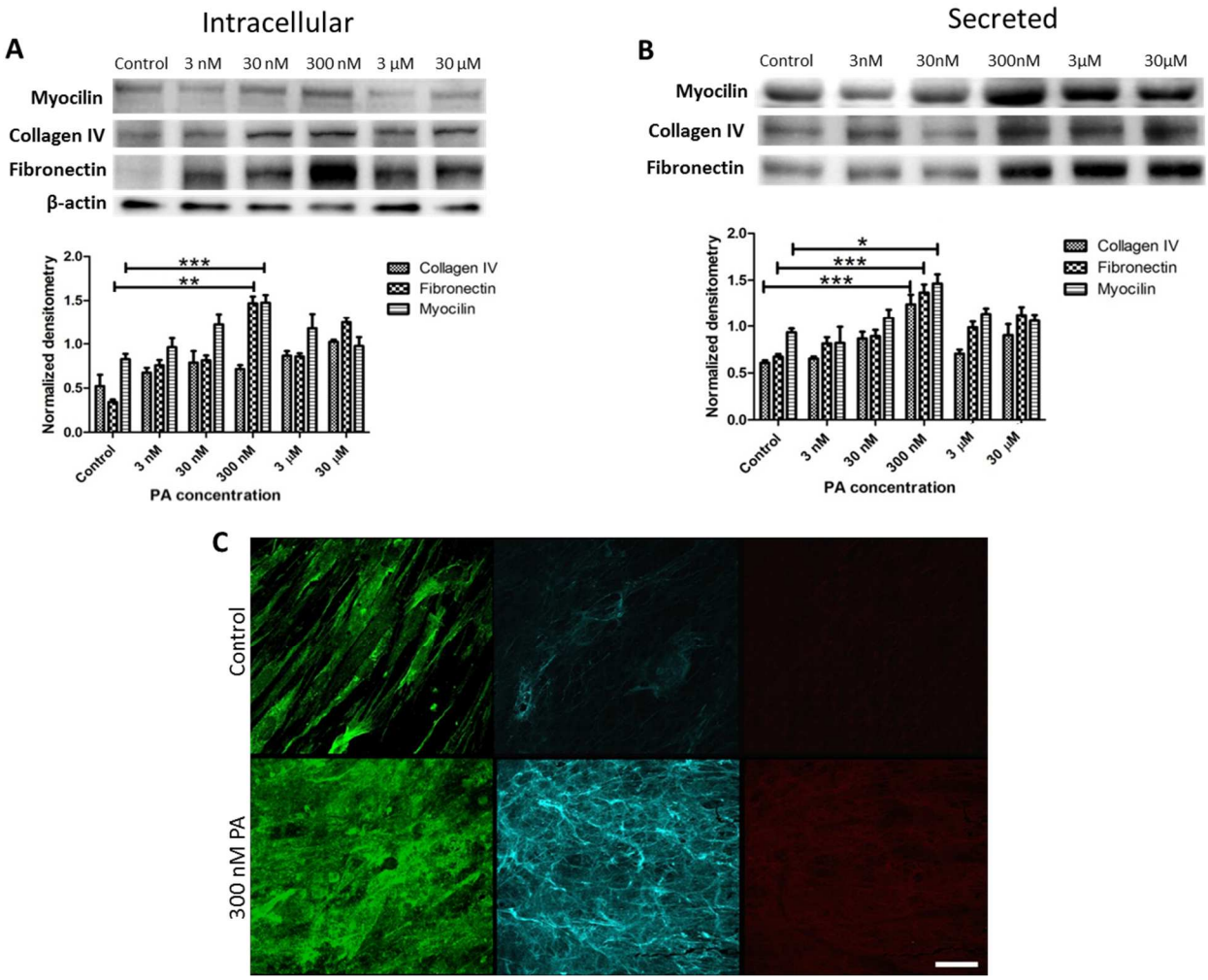

Figure 3.2. Effects of glucocorticoid on expression of myocilin and ECM proteins in 3D HTM. Western blot analysis of dose-response to prednisolone acetate (PA) on (A) intracellular expression and (B) secretion of myocilin, fibronectin and collagen IV. (C) Confocal images of immunocytochemistry of myocilin, fibronectin and collagen IV in 3D HTM after perfusion with vehicle control (top panel) or 300 nM PA (lower panel) for 9 days. Scale bar = 40 µm.

through immunocytochemistry analysis, which revealed rearranged patterns of these secreted proteins. Bioengineered 3D HTM constructs were perfused with 300 nM PA for 9 days. After perfusion with PA, secreted myocilin appeared amorphous and plaque-like, while collagen IV and fibronectin seemed remodeled into densely packed, thin fibrous arrangements (Fig. 3.2.C). In multiple PA-treated samples from multiple donor HTM cells, we consistently observed nodular, aggregated vertices formed by secreted collagen IV fibers, with a greater level of collagen IV expression than untreated cultures (Fig. 3.2.C, middle panel). The fine fibrils of collagen IV and fibronectin appeared denser and more organized than those in control cultures, similar to those described in human eyes with corticosteroid-induced glaucoma [207]. Altogether, the induction of myocilin expression and increase in ECM deposition confirmed that the bioengineered 3D HTM is responsive to PA.

3.3.2. Glucocorticoid-Induced Intensified Actin Rearrangements and Enlarged Nuclei

Given the increased attention to cytoskeletal rearrangements that have been described in patients with glaucomatous HTM, we examined whether similar changes were induced by perfused PA treatment in our model. Phalloidin-staining of F-actin filaments in HTM cells showed increased actin fibers after exposure to 300 nM PA for 9 days, several of which joined together into bundles, demonstrating crosslinked actin networks (CLANs). (Fig. 3.3.A-C) The CLANs observed in the bioengineered 3D HTM were similar in architecture to those reported after dexamethasone treatment in organ culture models as well as histological samples of glaucomatous HTM [193, 194, 207].

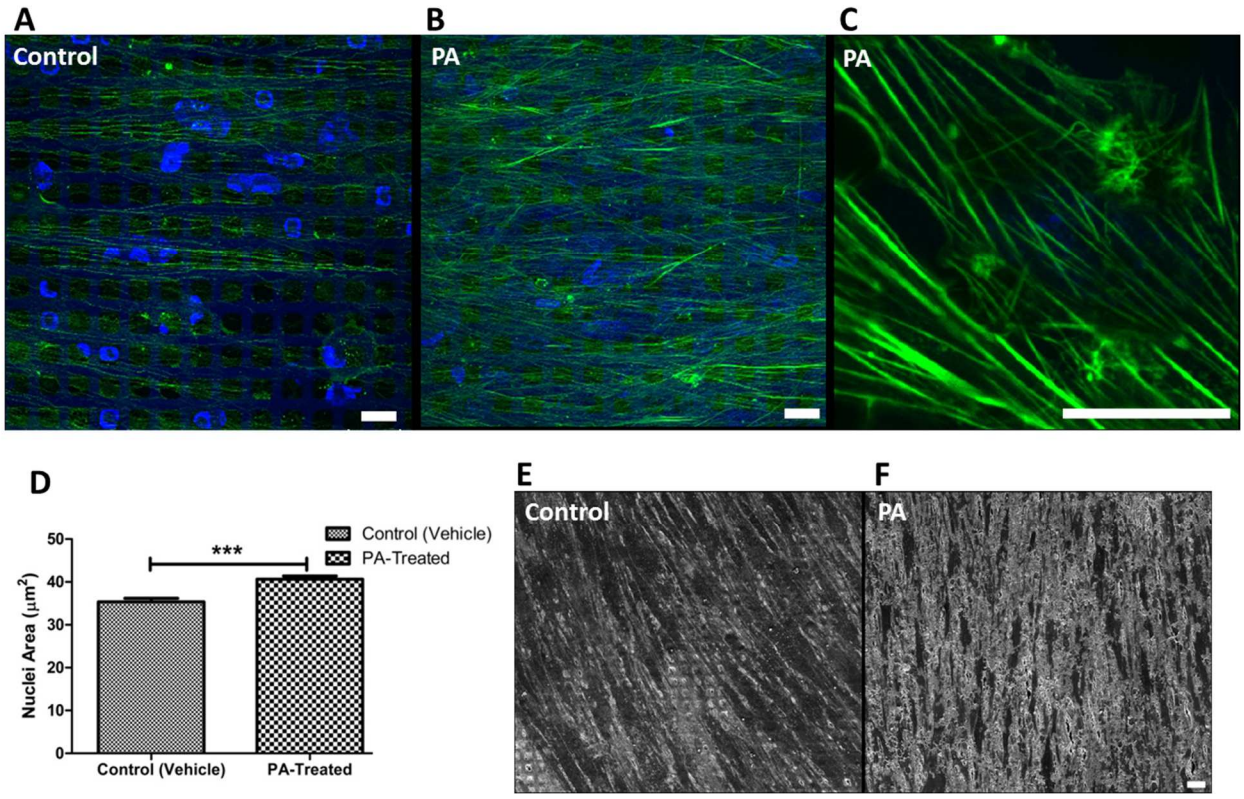

Figure 3.3. Effects of glucocorticoid on actin cytoskeleton and nuclear size in 3D HTM. (A-C) Confocal images of phalloidin-stained F-actin in untreated control (A) and treated with 300 nM PA for 9 days (B and C). (A) Scale bar = 30 μm. (B) Scale bar = 30 μm. (C) Scale bar = 20 μm. Arrows indicate CLANs. (D) Quantification of nuclear size after PA-treatment compared to control. (E and F) SEM images of cell morphology in 3D HTM of control (E) or with PA-treatment (F). Scale bar = 40 μm.

Although a few CLANs were also observed in control samples in one donor's HTM cells (data not shown), its PA- treated counterpart had even greater F-actin staining and more actin rearrangements. Moreover, cells treated with PA in our bioengineered 3D HTM model had larger nuclei compared to vehicle-treated controls. The area of the nuclei in both vehicle and PA-treated samples were measured and analyzed using ImageJ software. There was a significant difference in the nuclei size between vehicle- (36.9 ± 5.7 μm^2) and PA- (42.3 ± 5.1 μm^2) treated samples (N=12; t-test, $p<0.0001$) (Fig. 3.3.D). Enlarged nuclei have previously been reported in dexamethasone-induced

glaucoma *ex vivo* [208] and are associated with activated HTM cells. Scanning electron microscopy (SEM) revealed differences in the surface topography with larger amount of amorphous fibrillary material in the PA-treated cultures. HTM cells appeared embedded and even covered by this material, reducing intercellular spacing (Fig. 3.3.E-F). Furthermore, compared to vehicle-perfused controls where the cell surface was fairly smooth and cells were easily distinguished (Fig. 3.3.E), in PA-perfused samples, the cell surface appeared rough and surrounded by plaque material (Fig. 3.3.F).

3.3.3. Inhibited Phagocytotic Activity of the 3D Human Trabecular Meshwork After Steroid Treatment

Given corticosteroid-induced glaucomatous characteristics described in the studies above, functional properties of HTM cells were further analyzed to assess whether these morphological changes enhanced or impaired cellular functions. The phagocytic activity of bioengineered 3D HTM was assessed using E. coli labelled with pH-sensitive dye. These bioparticles are non-fluorescent outside the cell at neutral pH, but exhibit bright green fluoresce at acidic pH such as in phagosomes, indicating cellular uptake through phagocytosis. After treatment with 300 nM PA, fluorescence imaging revealed that only 5-10% of the PA-treated HTM cells were phagocytic, compared with 20-30% of HTM cells in vehicle-treated controls (Fig.3.4.A-B) demonstrating a statistically significant decrease in phagocytotic activity (Fig.3.4.C), similar to those reported after dexamethasone treatment *in situ* [196, 209].

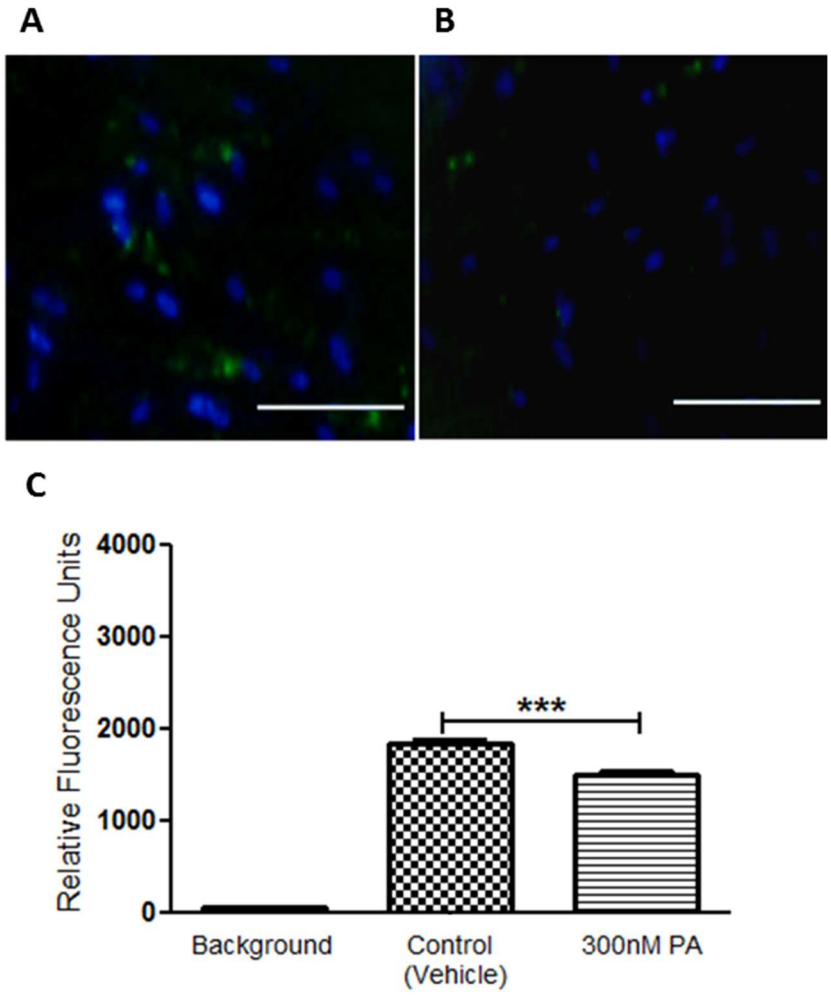

Figure 3.4. Inhibition of phagocytosis activity of 3D HTM after treated with glucocorticoid. (A and B) Confocal images of phagocytic 3D HTM of control (A) and treated with 300 nM PA for 3 days (B). Scale bar = 200 μm. (C) Quantitation of fluorescence analysis of phagocytic activity.

3.3.4. Increased Transcellular Electrical Resistance in the 3D Trabecular Meshwork Model After Steroid Treatment

We further characterized the pressure-independent resistance using real-time monitoring of electric cell-substrate impedance sensing (ECIS), which measures the transcellular electrical resistance towards ionic species in the medium [205, 210]. After 14 days of growth on the scaffold, the bioengineered 3D HTM constructs were analyzed. First, the impedance was recorded before treatment, where no significant

difference was observed between 3D HTM samples. Subsequently, samples were either treated with 300 nM PA or vehicle alone (control) for 11 days, throughout which impedance was continuously monitored (Fig.3.5.A). Medium was changed every two to three days, causing a spike in the impedance curve. Increased impedance was observed over time in PA-treatment compared to the vehicle-treated controls and, in particular, during days 9 through 11, establishing greater electrical resistance differences (N=8, 0.18 ±0.02 Ω/hrs vs.0.06 ± 0.03 Ω/hrs, P≤0.001).

To analyze the effect of actin networks on the increased transcellular electrical resistance caused by PA treatment, PA-treated 3D HTM samples were challenged with the actin disruptor Lat-B, an IOP-lowering agent, on day 11 for three hours while the resistance was continuously recorded. Lat-B rapidly decreased the electrical resistance across these samples, stabilizing after 3 hours. Even after Lat-B action, the resistance of the PA-treated constructs was still significantly higher (125 ± 2.3 Ω) than vehicle-treated controls (110 ± 2.6 Ω) (P<0.001)(Fig. 3.5.B), suggesting changes resulting from PA treatment beyond actin rearrangements.

Altogether, we have demonstrated that the bioengineered 3D HTM is responsive to PA treatment, exhibiting enhanced myocilin induction, increased ECM deposition, intensified actin rearrangements, enlarged nuclear size, reduced intercellular spacing, inhibited phagocytosis, and increased outflow resistance. These markers indicate a corticosteroid-induced glaucoma model that resembles the biological and biochemical characteristics of this disease at the pathology site, the HTM.

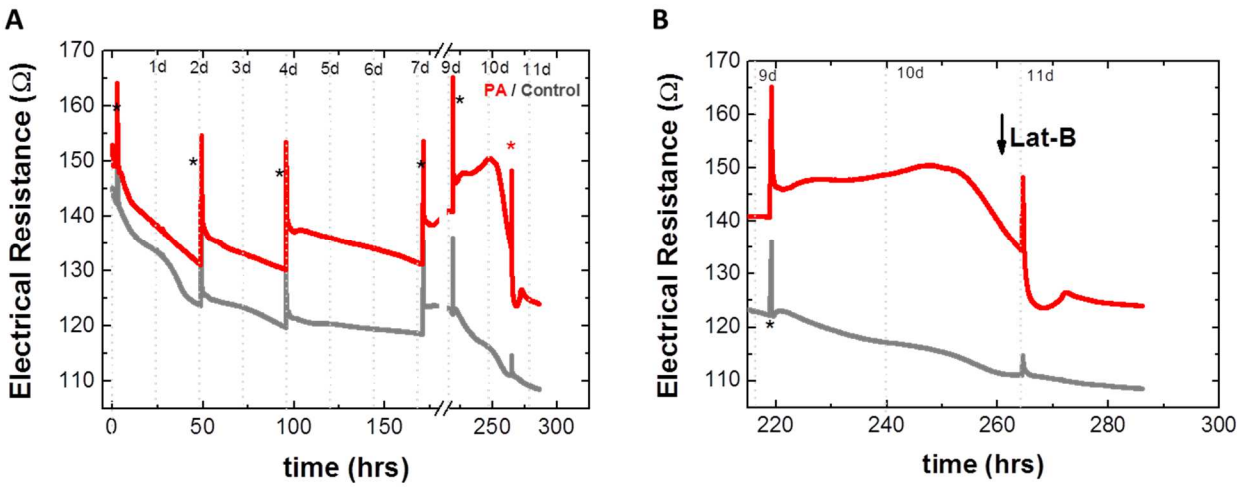

Figure 3.5. Glucocorticoid-induced elevated electrical resistance. (A and B) Electrical resistance during 11-day of PA-treatment with the addition of Lat-B (A) and enlarged graph for Lat-B treatment. (B) Black asterisks indicate medium changes; red asterisk indicates addition of Lat-B.

3.3.5. Physiological Outflow Studies in the Steroid-induced Glaucomatous 3D HTM Model

One of the main functions of the HTM is to regulate aqueous humor outflow. To examine the ability of our bioengineered 3D HTM model to regulate outflow, we utilized a perfusion system apparatus, as previously described [204], to study the hydrodynamic behavior, in which the rate of perfusate flow was controlled while recording the transmembrane pressure across the 3D HTM. After treatment with 300 nM PA for 9 days, the bioengineered 3D HTM construct was perfused with serum-free medium supplemented with 300 nM PA at various flow rates (2, 10, 20, and 40 µl/min) in an apical-to-basal orientation. The pressure was continuously recorded for over 6 hours to assure equilibrium at each flow rate. Bioengineered 3D HTM grown for 9 days and perfused with vehicle alone was used as the control. Compared to controls, PA perfusion significantly decreased the outflow facility (N=12, P<0.0001) across the 3D HTM (Fig.4C). The slope of the transmembrane pressure (P) versus flow rate (F) curve

for control cultures was 0.24 ± 0.011 mmHg/mL/min while that for PA-treated was 0.37 ± 0.014 mmHg/mL/min (Fig.3.6.A). Control cultures showed an outflow facility of 0.131 ± 0.003 μL/min/mmHg/mm^2 while PA treatment significantly lowered the outflow facility of the bioengineered 3D HTM to 0.093 ± 0.004 μL/min/mmHg/mm^2 (Fig.3.6.B). These data demonstrate that the bioengineered 3D HTM is GC-responsive, regulating perfusate flow in a similar fashion as aqueous humor outflow regulation seen *in vivo* and *ex vivo* glaucomatous HTM, by increasing pressure and decreasing the outflow facility across this tissue.

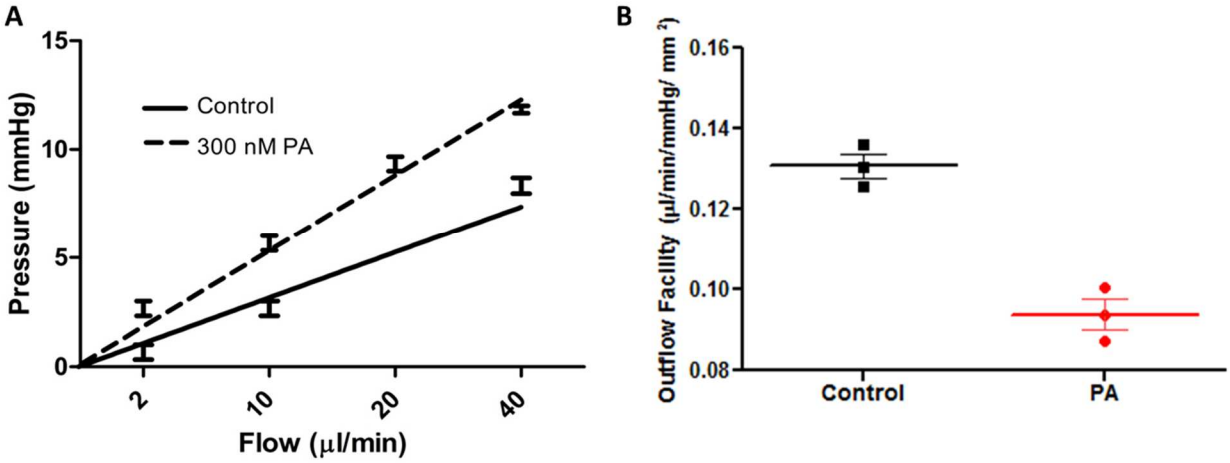

Figure 3.6. Glucocorticoid-induced outflow resistance in 3D HTM. (A) Trans-scaffold pressure as a function of flow rate. (B) Outflow facility.

3.3.6. Response to ROCK Inhibitor by ECM Remodeling in the Steroid-induced Glaucomatous 3D HTM Model

To explore the potential use of ROCK inhibitors to arrest the drastic effects observed from PA treatment on the HTM ECM, we treated 3D HTM samples with a combination of these two agents: 300 nM PA and 10 μM Y-27632, a ROCK inhibitor. Compared to PA-treatment alone, the presence of ROCK inhibitor during PA treatment

caused no significant change in myocilin expression, but significantly decreased ECM proteins, including collagen IV and fibronectin (N=9, P<0.001 for both proteins) (Fig.3.7.A-B). Compared to vehicle-treated controls, cells co-treated with PA and Y-27632 still exhibited significantly higher expression of intracellular myocilin (P<0.05) and αB-crystallin (P<0.01), but lower fibronectin expression (P<0.05).

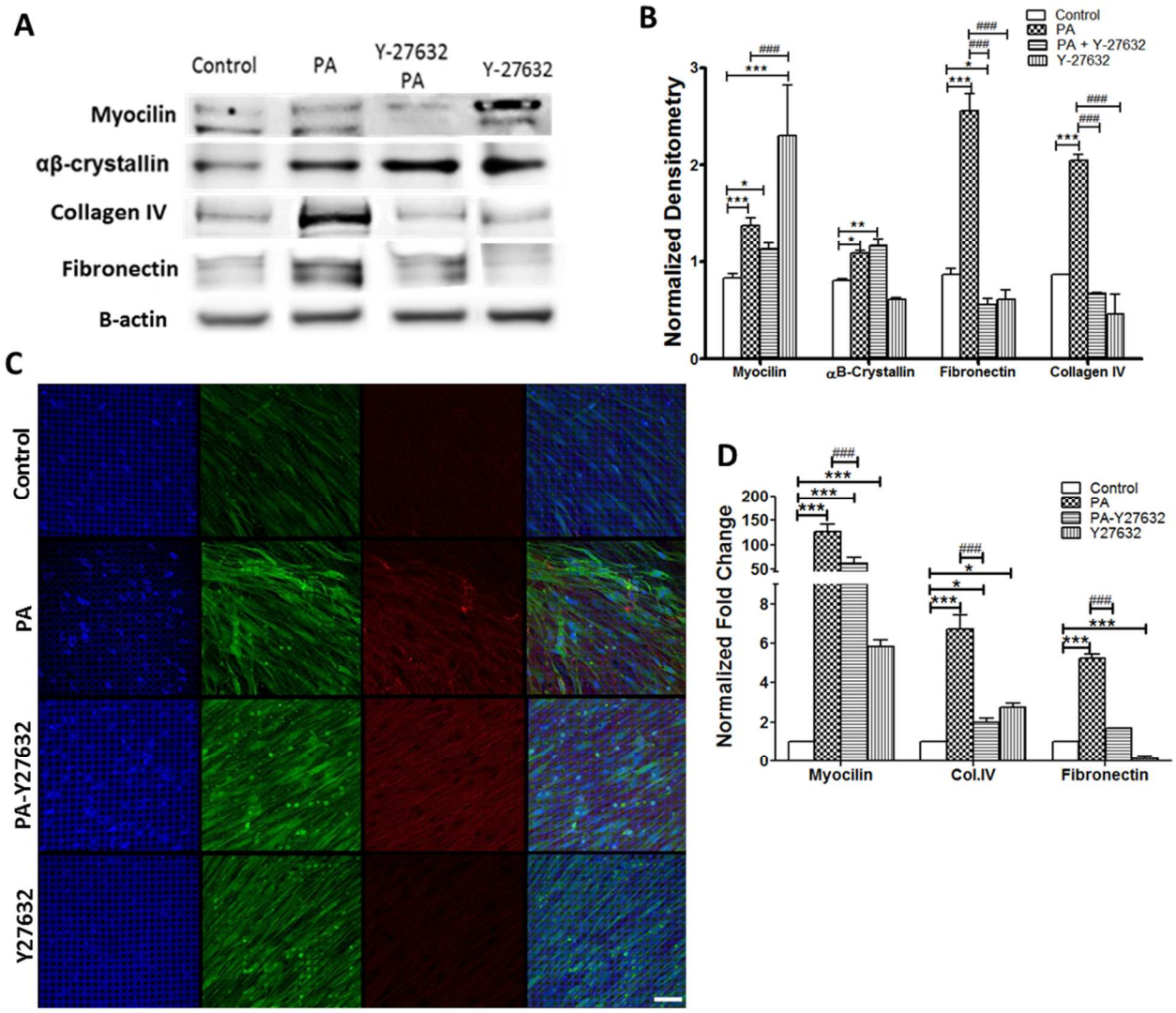

Figure 3.7. Expression of trabecular meshwork markers and ECM proteins in 3D HTM treated with glucocorticoid and/or ROCK inhibitor. (A) Western blot analysis of myocilin, αB-crystallin, fibronectin, and collagen IV for 3D-HTM scaffolds treated with ethanol (vehicle control), 300 nM PA, or 300 nM PA + 10 μM Y27632 for 9 days (left panel). Densitometry analysis of western blot (right panel). * p< 0.05, ** p < 0.005, *** p < 0.001, # p< 0.05, ## p < 0.005 and ### p < 0.001. (B) Confocal images of myocilin and αB-crystallin expression in 3D-HTM treated as in panel A Blue: DAPI-stained nuclei. Green: myocilin. Red: αB-crystallin.

Given the observed changes in ECM protein deposition, we evaluated expression of matrix metalloproteinase (MMP)-2 and -3 enzymes responsible for degradation and remodeling of the ECM at the conventional outflow pathway. Imbalances in the expression of these MMPs have been linked to POAG and corticosteroid treatments [211-213]. Similarly, increased MMP expression has been described soon after mechanical or pressure-induced homeostatic response in organ cultures [214]. Through a 9-day time course study, the transcriptional expression of MMP-2 and -3 after PA and PA/Y-27631 treatments were evaluated. MMP-2 mRNA expression increased ~2.4-fold after a 3-day PA-treatment compared to untreated controls ($P < 0.001$) (Fig. 3.8.A); this increase was eliminated by PA/Y-27631 co-treatment; however, after 5 days in culture, neither treatment showed any difference from control cultures. Interestingly, MMP-2 expression decreased ~1.8-fold ($P < 0.001$) after 9 days treatment with PA and to a greater extent (~2.2-fold, $P < 0.001$) with PA/Y-27632 treatment (Fig. 3.8.A). MMP-3 expression showed no significant difference between control, PA, and PA/Y-27632 treated cultures at day 3 and 5; however, by day 9, MMP-3 expression was down-regulated ~150-fold ($P < 0.001$) for PA treatment and 49-fold ($P < 0.001$) for PA/Y-27632 treatment, respectively (Fig. 3.8.B).

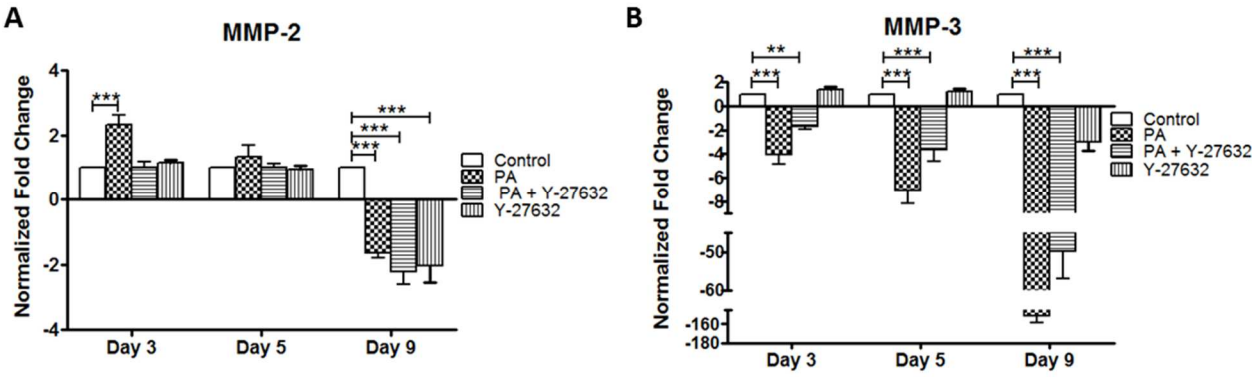

Figure 3.8. qPCR analysis of MMPs gene expression in 3D HTM after 3, 5 and 9 days of treatments with glucocorticoid (PA) and/or ROCK inhibitor (Y-27632). (A) MMP-2. (B) MMP-3. * $p< 0.05$, ** $p < 0.005$ and *** $p < 0.001$.

3.3.7. Dynamic Gene Expression of Cytokines in the Steroid-induced Glaucomatous 3D HTM Model

HTM cells secrete several cytokines that modulate cell behavior and ECM turnover at the conventional outflow pathway. Therefore, we investigated whether the transcriptional expression of these cytokines was modulated as a result of PA treatment, which could give us some insight into the pathology of corticosteroid-induced glaucoma. Increased cytokine expression have been observed in the aqueous humor of glaucoma patients, including tissue inhibitor of metalloproteinase-1 (TIMP-1) [215] and transforming growth factor-β (TGFβ) [216, 217]. In addition, interleukin 1-alpha (IL-1α) is an inflammatory cytokine that can regulate outflow facility [86]. Transcriptional expression of cytokines IL-1α, TIMP-1 and TGFβ were studied in response to PA alone and PA/Y-27632 treatment. IL-1α mRNA expression was down-regulated 21-fold, 41-fold, and 16-fold ($P < 0.001$ for each) after PA treatment for 3, 5 and 9 days, respectively (Figure 3.9.A). Treatment with Y-27632 ROCK inhibitor exhibited a time-dependent effect on IL-1α mRNA expression during PA treatment. On days 3 and 5 after initiation of PA/Y-27632 treatment, the PA-induced decrease in IL-1α gene expression was partially rescued by the presence of Y-27632, but still lower than untreated controls by 10- ($P < 0.05$) and 17-fold ($P < 0.05$), respectively. On day 9, the presence of Y-27632 during PA treatment caused an even greater decrease in IL-1α gene expression (61-fold) compared to untreated controls ($P < 0.001$). While TIMP-1 mRNA expression was up-regulated by 4- ($P < 0.001$) and 2-fold ($P < 0.05$) after 3 and 5 days of PA-treatments, after day 9, TIMP-1 was down-regulated by 2-fold ($P < 0.001$) (Figure 3.9.B). On the other hand, co-treatment with Y-27632 during PA treatment

obviated changes in TIMP-1 gene expression for all 9 days. TGFβ gene expression was down-regulated on days 3 and 5 by PA treatment (1.2- and 3.2-fold) and to a greater extent during PA/Y-27632 co-treatment (4.8- and 2.8-fold, $P < 0.001$ for all) (Fig. 3.9.C). Despite its initial down-regulation, TGFβ gene expression was up-regulated over 3.7-fold by PA treatment for 9 days suggesting potential bi-phasic response. Given TGFβ's ability to enhance ECM protein expression and deposition that can block paracellular pores at the HTM, this final increased expression of TGFβ in PA-treated 3D HTM could account for the greater suppression of MMPs observed on day 9 and increased transcellular electrical resistance seen at the same time. Although extended analysis of GC effect on TGFβ expressed by TM cells have not been reported previously, studies performed using human lung fibroblast cells have shown that GC modulate TGFβ production [218], and similarly to these studies, several days of GCs treatment initially inhibited TGFβ. The presence of Y-27632 during PA treatment reduced TGFβ gene expression back to the control level on day 9. This is the first time, to our knowledge, that the effects of extended treatment with PA in the presence and absence of ROCK inhibitors on gene expression of these cytokines have been examined. The dynamic pattern of MMP and cytokine gene expression also highlights the importance of a 3D HTM model that is suitable for long-term drug treatment studies.

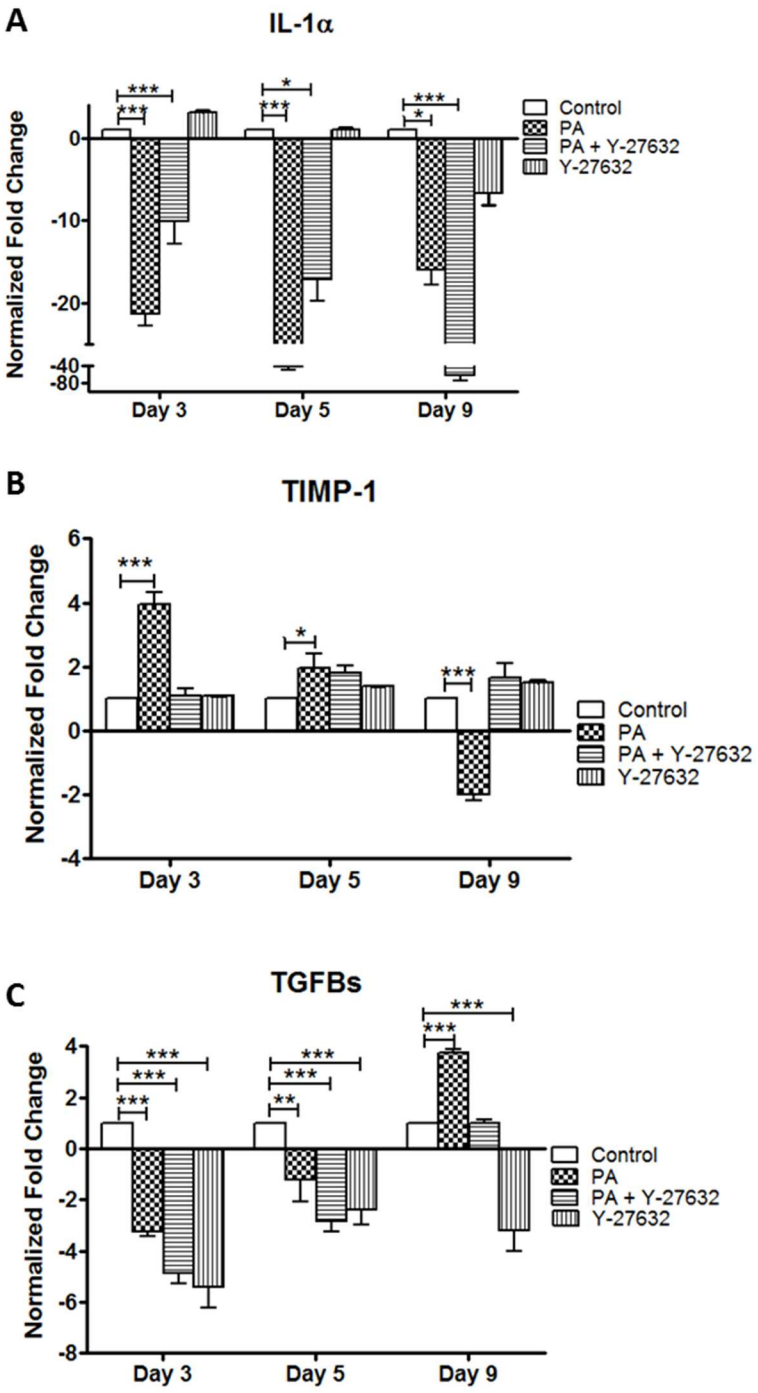

Fig.3.9. qPCR analysis of gene expression of cytokines in 3D HTM after 3, 5 and 9 days of treatments with glucocorticoid (PA) and/or ROCK inhibitor (Y-27632). (A) IL-1α. (B) TIMP-1. (C) TGFβ. * $p< 0.05$, ** $p < 0.005$ and *** $p < 0.001$.

3.4. Discussion

In this study, we have demonstrated that a bioengineered 3D HTM is responsive to PA and exhibits morphological and physiological changes, similar to those observed *in vivo* and *ex vivo* studies. It further validates the bioengineered 3D HTM's responsiveness to glaucoma-inducing agents and, in particular, to GCs. The specific cause of elevated IOP and increased outflow resistance characteristic of corticosteroid-induced glaucoma is still unknown, despite being a topic of investigation for over 50 years [181, 219]. Our studies strengthens the notion that there are several factors that, together, orchestrate the increase of outflow resistance/decrease of outflow facility at the HTM in response to corticosteroid-induced glaucoma, including increased myocilin expression and secretion, enhanced ECM deposition, intensified actin fiber crosslinking, decreased gene expression of MMPs, increased gene expression of TGFβ, and decreased phagocytosis after 9-days of PA treatment.

The bioengineered HTM presented in this work is of particular clinical-relevance, given that the outflow facility per unit area of human eyes and our bioengineered HTM are comparable. By taking into account the circumference of a human eye (assuming an eye of 12 mm diameter) with a TM of 100 μm in width, the surface area of filtering HTM (π x 12mm x 0.10mm) is ~3.8 mm^2. *In vivo* outflow facility of normal human eye is 0.3-0.4 μL/min/mmHg, therefore in terms of outflow facility per unit area, it translated to 0.078-0.106 μL/min/mmHg/mm^2. Our bioengineered 3D HTM has an outflow facility per unit area of 0.131 ± 0.003 μL/min/mmHg/mm^2, approximately 1-2 times of its *in vivo* counterpart. Therefore this bioengineered *in vitro* model is more effective at studying outflow physiology than other *in vitro* TM models developed thus far.

The density and deposition of ECM proteins in our bioengineered corticosteroid-induced glaucomatous 3D HTM model was significantly greater than in normal HTM controls. Corticosteroid-induced elevation of IOP is generally believed to be caused by increased resistance to aqueous outflow through changes caused in the TM and its ECM [207, 208, 220, 221]. In addition, characteristic extracellular fibrillary material associated with the basement membrane has been described in the HTM of corticosteroid-induced glaucoma eyes [207], in addition to amorphous granular material deposited in the extracellular spaces. The ECM is an intricate network of an array of macromolecules composed of fibrous proteins (e.g., collagen, elastin), cell binding glycoproteins (e.g. fibronectin, laminin), and proteoglycans [222]. These macromolecules link together and influence the behavior and biological characteristics of HTM cells. The major ECM components in the HTM include collagen I, III and IV, fibronectin, laminin and elastin as well as proteoglycans [222]. Increased expression of ECM proteins has been reported in humans after exposure to corticosteroids [220]. In our 3D HTM model, we have been able to qualitatively and quantitatively measure the increased expression of fibronectin, collagen IV and laminin proteins after corticosteroid treatment, which is consistent with organ perfusion models [223, 224]. Furthermore, myocilin was also expressed and elevated in our model, which reflects the *in vivo* glaucomatous HTM. Further, densitometry analysis of intracellular and secreted myocilin and fibronectin as well as secreted collagen IV, showed a biphasic dose-response to PA. The immunocytochemistry of the secreted collagen IV and fibronectin revealed different topographical/morphological patterns between the PA treated and vehicle -treated controls. Both proteins exhibited greater amounts of ECM crosslinked

fibers, suggesting increased matrix assembly, which may be in part responsible for the increased resistance across this tissue.

ECM turnover is tightly regulated by balancing assembly and degradation through MMPs, TIMPs and structural proteins. MMPs are secreted by HTM cells and are responsible for breaking down ECM proteins and remodeling the ECM [212]. MMP-2 and -3 are thought to help maintain homeostasis of the conventional outflow architecture [217, 225]. MMP-2 and MMP-3 both degrade gelatin, collagens IV and V, laminin, and fibronectin. Several studies demonstrated that agents that modulate outflow facility in perfusion cultures can affect the expression/activation of these MMPs [10, 226]. Therefore, the decrease of MMP-2 and -3 gene expression over time could account for the increased amounts of ECM observed. Initial MMP-2 increases suggest that in corticosteroid-induced glaucoma, TM cells strive to correct any overproduction of ECM. However, the persistent action of this MMP likely causes overproduction of replacement ECM and/or cleavage of ECM components which might not be readily accessible to degradation or cleavage such as TGF-βs. Over extended exposure to PA, these MMPs are down-regulated, which can leave substantial accumulated paracellular ECM at the HTM and its basement membrane, as observed by our SEM and confocal microscopy. Likewise, phagocytosis has been proposed to be involved in ECM turnover [196, 227, 228]. Therefore, the decrease in phagocytic activity after corticosteroid treatment seen during our studies, could raise irregularities in the clearance mechanisms of HTM cells and affect ECM turnover. These irregularities might account for some of the amorphous plaque-like material formed after PA treatment.

Steroids exert physiological effects through their interaction with cytoplasmic receptors, followed by DNA-binding and transcriptional modulation [229]. HTM cells contain GC receptors, and therefore, should be corticosteroid responsive. Steroids can induce increased cytoplasmic and nuclear areas [230]. Our studies suggest similar actions by PA in HTM cells, which exhibited enlarged nuclei and cytoplasm. In some instances, HTM cells lying within the fibrillary material appeared to be transformed into myofibroblasts, with prominent cytoplasmic filaments resembling actin and dense regions of the cell membrane (data not shown). PA can also cause variations in transcriptional expression of cytokines. IL-1α, known to induce MMP-3 production, was down-regulated as expected, given PA's anti-inflammatory nature and association with decreased MMP-3 gene expression. Interestingly, TIMP-1 was initially up-regulated but down-regulated over time, which may inhibit the activity of certain MMPs over the initial stages of corticosteroid exposure. TIMP-1 is a strong cytokine inhibitor of MMP-1 [231] that has been described as a potential key cytokine in ECM turnover in the conventional outflow pathway [225]. Based on our results, TIMP-1 could be inhibiting the initial production of certain MMPs in an attempt to restore homeostasis but over time might be subsequently decreased given the decrease in MMP expression/activity. The synergetic decrease of MMP-2 and TIMP-1 observed here, has been reported in previous studies focused on exogenous selenium treatments on HTM cells [225]. Another cytokine that has received increased interest for its relationship with glaucoma is TGFβ. TGFβ alters ECM metabolism by suppressing MMP-3 and in turn, increases the deposition of fibronectin [216, 217]. TGFβ is over-expressed in glaucomatous aqueous humor and is up-regulated in corticosteroid-induced animal models [232]. Our glaucomatous 3D HTM

model demonstrated that the increase in gene expression of TGFβ is a process that may take over a week, underlying the importance of long-term and time-course studies when attempting to understand the transcriptional effect of corticosteroids on endogenously secreted cytokines.

The actin cytoskeleton is physically linked to the ECM through focal adhesions [233]. Contraction or disruption of actin cytoskeleton diminished the number of adhesions between cells and ECM in several cell types [234, 235]. Rearrangements of the cytoskeleton of HTM cells are related to elements including actin microfilaments, tubulin microtubules and intermediate filaments, which may be affected by exposure to GCs. GCs reorganize and remodel the TM cytoskeleton into crosslinked actin networks (CLANs) in human anterior segments [192]. To this end, several agents have been used in different fields to study the effect of cytoskeleton modulation, including cytochalasin, latrunculins (Lat), H-7, and ROCK inhibitors. Many of these agents decrease outflow resistance through cytoskeletal reorganization of the actomyosin system (the complex of actin and myosin) when applied to the HTM [236-239]. Based on our ECIS studies, cytoskeletal arrangements greatly account for the transcellular electrical resistance across the 3D HTM tissue, which was shown by a dramatic decrease in impedance after Lat-B treatment. Although challenging PA-treated 3D HTM with the IOP-lowering agent, Lat-B, reduced the impedance, the final transcellular electrical resistance was still greater than that of vehicle-treated controls. This suggests that cytoskeleton disruption alone is not sufficient to reduce the PA-induced outflow resistance to normal. The ECIS is extremely sensitive to changes in cell morphology, which are evoked by alterations in architecture of structural components including cell-

cell and cell-ECM junctions [206, 240]. ECM accumulation on the tissue likely affected the outflow resistance resulting in the residual transcellular electrical resistance after Lat-B treatment.

Actin cytoskeleton and fibronectin matrix assembly is promoted by RhoA with contributions from ROCK I and II [241, 242]. ROCK inhibitors are currently being studied as potential therapeutics for glaucoma management. Recent studies have demonstrated their efficacy in reducing IOP in human eyes [201, 202] through alteration of the HTM cytoskeletal arrangement and cell shape [238, 243, 244]. Here, the ROCK inhibitor, Y-27632, alleviated the PA-induced increase in fibronectin and collagen IV protein (Figs. 5 A, B and C) and gene expression (Fig. 5D), which alludes to cell-ECM disruption and ECM regulations at the HTM by the ROCK I and II. Co-treatment with Y-27632 restored collagen IV protein expression to normal levels compared with PA treatment alone, similar to a recent *ex vivo* study in which DEX treatment significantly increased collagen IV and fibronectin gene expression while combining DEX/Y-27632 mitigated the increase [245]. In particular, the DEX-induced decrease in outflow facility was restored to normal levels by the combined DEX/Y-27632 in porcine anterior segment organ cultures [245]. These studies suggested the involvement of the ROCK signaling pathway in corticosteroid-induced ocular hypertension. Additionally, the presence of Y-27632 during PA treatment for 9 days reduced PA-induced alterations in cytokine (e.g., TIMP-1, TGFβ) gene expression to the normal levels of 3D HTM without any other treatment.

Interestingly, expression of myocilin and αβ-crystallin in PA-treated 3D HTM remained higher than controls in the presence of ROCK inhibitor. This was further confirmed

through qPCR analysis (Supplemental Fig. 2). Treatment with Y-27632 alone also increased myocilin, suggesting the relationship between ROCK inhibition and myocilin upregulation is complicated, which requires further investigation especially given myocilin has long been linked to glaucoma. Additionally, αB-crystallin, an understudied protein due to its lack of expression in conventional 2D cultures, is found at elevated levels in aqueous humor of POAG patients [246] Our 3D HTM model exhibits αB-crystallin expression which increased after PA treatment. The presence of Y-27632 during PA treatment does not alleviate PA-induced increase of αB-crystallin, suggesting the feasibility of studying the role of this protein in HTM physiology and pathology using our bioengineered 3D HTM model.

The primary HTM cells used in this model system remain viable and function for over 6 weeks, enabling us to examine the effects of chronic exposure to corticosteroids and study the therapeutic effects of IOP-lowering agents. Overall, we have demonstrated that this bioengineered, corticosteroid-induced glaucomatous 3D HTM perfusion model system is a clinically and physiologically relevant platform for long-term study of the physiology and pathology of human outflow pathway with respect to the HTM. Using this model, we demonstrated that glucocorticoid-induced ECM alterations and cytokine expression in HTM can be modified by co-treatment with ROCK inhibitors, leading to better understanding of the pathology of corticosteroid-induced glaucoma and new treatment regimens combining ROCK inhibitors with corticosteroids.

CHAPTER 4

TGFβ-2-induced Biological and Outflow Alterations in the Bioengineered Trabecular Meshwork are Offset by a Rho-associated Kinase Inhibitor

4.1. Introduction

The transforming growth factor β (TGFβ) family members play a key role in immune responses and tissue development such as inflammation, wound healing, extracellular matrix (ECM) accumulation, bone formation, cellular differentiation, and tumor progression. Currently, three isoforms of this family have been identified: TGFβ-1, -2 and -3. TGFβ-1 and -2 stimulate ECM production and fibrotic responses in diverse ocular tissues [247, 248]. The importance of TGFβ in ophthalmology is evident by its endogenous expression in the anterior segment, as well as its presence in the aqueous humor, which is responsible for chamber-associated immune deviation, a mechanism that protects the eye from inflammation and immune-related tissue damage.

In particular, TGFβ appears to be involved in the pathogenesis of certain glaucomas [66]. For example, TGFβ-2 is significantly elevated in the aqueous humor of patients with primary open-angle glaucoma (POAG) [249] and induces pathological changes at the trabecular meshwork (TM) and optic nerve. In POAG, the sheath of connecting fibrils or plaques as well as ECM components that are present in the cribriform region of the TM increase significantly, leading to elevated intraocular pressure (IOP) [56].

Treatment of cultured human TM (HTM) cells with TGFβ-2 could increase the expression of ECM proteins, fibronectin and tissue transglutaminase —an enzyme known to crosslink ECM proteins into complexes that can no longer be digested by proteinases [250]. In human eye organ culture perfusion studies, TGFβ-2 treatment reduced the outflow facility and increased ECM accumulation in the TM, indicating an elevation in IOP [251]. Additionally, enzyme plasminogen activator inhibitor (PAI), which inhibits most matrix metalloproteinases (MMPs), was increased as a result of TGFβ-2 treatments [252]. The fibrogenic effect caused by TGFβ-2 is believed to be mediated, in part, by activated RhoGTPase/Rho-associated kinase (ROCK). ROCK inhibitors can affect the contractile properties of TM cells, α-smooth muscle actin (α-SMA) expression, ECM accumulation in the outflow pathway and aqueous humor outflow. Several of these factors are also affected by TGFβ-2, suggesting a common pathway. However, there is a knowledge gap on how TGFβ regulates the outflow facility of TM mechanistically and how HTM-characteristic proteins are regulated in the presence of ROCK inhibitors.

To address these biological questions, we investigated effects of TGFβ-2 at a clinically relevant concentrations using a 3D bioengineered HTM model that has been previously described and validated [204]. By hypothesizing that effects elicited by TGFβ-2 can be suppressed in the presence of ROCK inhibitor, we analyzed actin expression pattern, ECM deposition, changes in HTM marker expression of myocilin and αB-crystallin, modulation of MMPs and cytokines induced by TGFβ-2 in the absence or presence of ROCK inhibitors in relationship to the regulation of outflow facility.

4.2. Materials and Methods

4.2.1. Primary Human Trabecular Meshwork Cell Culture

Primary HTM cells were isolated from the juxtacanalicular region of cadaveric ocular tissue, and cultured in a manner similar to that previously described [94] . Before use in experiments, all HTM cell strains were characterized for expression of αβ-crystalline and α-smooth muscle actin. HTM cells were initially plated in 75 cm^2 cell culture flasks with 10% fetal bovine serum (FBS) (Atlas Biologicals, Fort Collins, CO) in Improved MEM (IMEM) (Corning Cellgro, Manassas, VA) with 1% 10 mg/mL gentamicin. Fresh medium was supplied every 48 h. Cells were maintained at 37˚C in a humidified atmosphere with 5% carbon dioxide until 80-90% confluence which point cells were trypsinized using 0.25% trypsin/0.5 mM EDTA (Gibco, Grand Island, NY) and subcultured. At least three donors' human primary cell cultures were used during experiments. All studies were conducted using cells before the 5^{th} passage.

4.2.2. Scaffold Fabrication

SU-8 2010 photoresist (MicroChem Corp.) was used to develop free-standing porous microstructures that served as scaffolds on which primary HTM cells were cultured. Using photolithographic techniques and a chrome mask with defined micrometer-scale features, we fabricated SU-8 scaffolds as previously described [204]. Briefly, a release layer was spin-coated on the silicon wafer (substrate) and baked at temperatures between 120-150°C. Photoresist was spin-coated on the substrate to a final thickness of <5 μm, then baked at 95˚C and cooled to room temperature. The

photoresist was exposed to UV-light (140 mJ/cm^2) through a chrome mask containing the desired pattern, baked at 95˚C and developed in PGMEA developer (MicroChem Corp.) SU-8 scaffolds with desired features were released from the substrate, washed with isopropyl alcohol, air dried and stored at room temperature. Scaffolds were mounted on aluminum rings, sterilized using 70% ethanol and coated with 1% gelatin before seeding HTM cells.

4.2.3. 3D Culture of HTM Cells on Scaffolds and TGFβ-2 +/- Y-27632 treatment

To create 3D HTM constructs, 40,000 HTM cells were seeded on each microfabricated SU-8 scaffold, which was surrounded by an aluminum ring. After seeding, each scaffolds was placed in a well of a 24-well plate and cultured in 10% FBS-IMEM for 14 days. The aluminum ring allowed suspension of the scaffold, preventing cell contact with the bottom of the well. Medium was changed every 2-3 days. By day 14, HTM cells-scaffold constructs formed a 3D structure [204]. Samples were serum- starved in 1% FBS for 48 hrs and then treated with TGFβ-2 (2.5 ng/mL in 4 mM HCl, R&D systems, Minneapolis, MN), vehicle alone, Y-27632 (10 μM, Sigma Aldrich, ST. Louis, MO) or a combination of TGFβ-2 (2.5 ng/mL) and Y-27632 (10 μM) in 1%FBS-IMEM for 3, 6 and 9 days, as indicated.

4.2.4. Perfusion Studies

A perfusion apparatus was used as previously described [204]. After 14 days in culture, 3D HTM constructs were serum-starved in 1% FBS and treated with TGFβ-2, TGFβ-2/Y-27632, or vehicle alone for 9 days (as described above). Then 3D HTM samples were securely placed in the perfusion chamber and perfused at various rates

for 6 hrs per flow rate (2, 10, 20 and 40 µl/min or 2, 4, 6, 8, 10 µl/min). Samples were perfused in an apical-to-basal direction with perfusion medium consisting of Dulbecco's modified Eagle's medium (DMEM) (Cellgro) with 0.1% w/v gentamicin (MP Biomedicals) containing vehicle, 2.5ng/mL TGFβ-2 or TGFβ-2 with 10 µM Y-27632. The temperature was maintained at 34˚C throughout the experiment. Pressure was continuously monitored and recorded. After perfusion, the outflow facility of our bioengineered 3D HTM model was calculated from the inverse of the slope of the pressure versus flow per unit surface area. At least eight different samples per condition, including HTM cells from three donors, were studied under perfusion. In later experiments, 10 µM Y-27632 was also used as negative control.

4.2.5. Phalloidin Staining, Immunocytochemistry, and Confocal Microscopy

3D HTM samples were fixed in 4% paraformaldehyde, permeabilized with 0.2% Triton X-100, and blocked using 5% goat serum. To reveal cytoskeleton arrangement, samples were stained for F-actin using phalloidin (Life Technology) and incubated with antibody against α-SMA (Sigma-Aldrich). To confirm HTM marker expression, samples were incubated with antibodies against HTM markers, myocilin and αβ-crystallin (Table 4.1.A). To examine ECM proteins, samples were incubated with antibodies against collagen IV, fibronectin, and laminin (Abcam), as described previously [204]. Samples were co-stained with DAPI to reveal cell nuclei, followed by confocal imaging. Laser scanning confocal microscopy was performed using a Leica SP5 confocal microscope, and images were acquired at 40X and 63 X magnification using an oil-immersion objective. Confocal images were processed using Leica LasAF software, and all confocal images within a given experiment were imaged and captured using the same laser intensity and gain settings in order to be able to compare intensities across samples.

A

Name	Specie	Dilution	Company	Secondary Antibody
Alexa-488 conjugated Phalloidin	-	1/100	Life Technologies	-
α-SMA	mouse	1/800	Sigma Aldrich	Goat anti-mouse 594
Collagen type IV	Rabbit	1/200	Abcam	Goat anti-rabbit 488
Fibronectin	Mouse	1/100	Abcam	Goat anti-mouse 594
Laminin	Chicken	1/500	Abcam	Goat anti-chicken 633
Myocilin	Rabbit	1/200	Sigma Aldrich	Goat anti-rabbit 488
αB-crystallin	mouse	1/200	Abcam	Goat anti-mouse 594

B

Name	Specie	Dilution	Company	Secondary Antibody
Collagen type IV	Rabbit	1/100	Abcam	HRP goat anti-rabbit
Fibronectin	Mouse	1/100	Abcam	HRP goat anti-mouse
Myocilin	Rabbit	1/200	Sigma Aldrich	HRP goat anti-rabbit
αB-crystallin	mouse	1/500	Abcam	HRP goat anti-mouse

Table4.1. Primary antibodies. Information of antibodies used for (A) immunocytochemistry and (B) western blot analysis.

4.2.6. Protein Extraction and Western Blot Analysis

Cellular proteins were extracted with ice-cold radioimmunoprecipitation assay (RIPA) buffer (50 mM Tris-HCL, pH 7.5, 150 mM sodium chloride, 1% Triton X-100, 1% sodium deoxycholate, 0.1% sodium dodecyl sulfate, 25 mM NaF, 0.1 mM sodium orthovanadate, 10 mM NaP_4O_7, 1 nM phenylmethyl sulfonyl fluoride) containing protease inhibitors (Complete Protease Inhibitor, Roche, Manheim, Germany) on ice. Proteins were quantified by bicinchoninic acid assay (Thermo Fischer Scientific). 20 µg of proteins from each sample were separated by SDS polyacrylamide gel electrophoresis on a 4-12% gel in MOPS running buffer (Life Technologies), transferred onto a PVDF membrane and probed with the following primary antibodies rabbit anti-myocilin (Sigma Aldrich), mouse anti-αβ-crystallin, mouse anti-fibronectin, rabbit anti-collagen IV and mouse anti-β-actin (Abcam) (Table 4.1.B). HRP-conjugated goat anti-mouse or anti-rabbit secondary antibodies (Invitrogen) were used. Bound antibody was

detected using FluorChem E (Protein Simple). Protein expression was analyzed by densitometry using ImageJ, and normalized to the housekeeping gene β-actin. All experiments were performed duplicate for each of three donor cells.

4.2.7. Quantitative Real-time PCR (qPCR) Analysis

Total RNA was extracted from samples cultured for 3, 5, and 9 days with TGFβ-2, TGFβ-2/Y-27632, or without treatment using an RNeasy Plus Mini kit (Qiagen Inc., Valencia, CA). RNA concentrations were determined using a NanoDrop spectrophotometer. 20 ng of RNA per sample was used for each qPCR experiments. qPCR was carried out using TaqMan RNA-to-CT 1-Step Kit (Applied Biosystems, Carlsbad, CA) and performed on an AB StepOnePlus Real Time PCR system (Life Technologies) using primers for MMP-2, MMP-3, TIMP-1, IL-1α, TGFβ-2 and GAPDH (Table 4.2.). The temperature profile was as follows: 48˚C for 15 min (reverse transcription step), followed by an enzyme activation step of 95°C for 10 min, 40 cycles of 15 s denaturation at 95°C and 1 min anneal/extend at 60°C. Relative quantitation data analysis was performed using the comparative quantification method, ΔΔCt, with GAPDH as the endogenous reference. All samples were normalized to the vehicle-treated controls. q-PCR experiments were performed in triplicate (technical replicates) from duplicate biological experiments for each of the three donor cells. Average values are presented as mean ± SD.

4.2.8. Statistical Analysis

Data are expressed as mean ± standard deviation. The difference among vehicle-treated (controls), TGFβ-2-treated, and TGFβ-2/ Y-27632-treated 3D HTM

samples was analyzed using two-way ANOVA followed by Bonferroni post-tests (GraphPad Prism 6.02; GraphPad Software, Inc., La Jolla, CA). P values: $P < 0.05$, $P < 0.01$, and $P < 0.001$ are considered significant, very significant, and extremely significant, respectively.

NCBI Gene symbol	Ref. Sequ. number	Forward Primer	Reverse Primer
MMP2	NM_004530	CCAAGGTCAATGTCAGGAGAG	GCACCCATTTACACCTACAC
MMP3	NM_002422	TGAGTGAGTGATAGAGTGGT	TGAACAATGGACAAAGGATACAAC
TIMP1	NM_003254	GCTTGGAACCCTTTATACATCTTG	CCTTCTGCAATTCCGACCT
IL1A	NM_000575	AGTTCTTAGTGCCGTGAGTTTC	GTGACTGCCCAAGATGAAGA
TGFB2	NM_003238	ACTTTGCTGTCGATGTAGCG	GCAGAGTTCAGAGTCTTTCGT
GAPDH	NM_002046	TGTAGTTGAGGTCAATGAAGGG	ACATCGCTCAGACACCATG

Table 4.2. qPCR primers

4.3. Results

4.3.1. TGFβ-2 changes physiological outflow properties of the 3D bioengineered HTM

Given that regulation of aqueous humor flow is one of the main functions performed by the TM, we investigated the hydrodynamic behavior and transcellular pressure across the 3D HTM after treatment with TGFβ-2 over at least 9 days. We utilized a perfusion system apparatus, as previously described [204], that controls perfusion flow rate while constantly monitoring pressure changes. After treatment with 2.5ng/mL TGFβ-2 alone or in combination with 10 μM Y-27632 for 9 days, the bioengineered 3D HTM construct was place in the perfusion chamber and perfused with serum-free medium supplemented with 2.5ng/mL TGFβ-2 at various flow rates (2, 4, 6, 8 and 10 μL/minute) in an apical-to-basal orientation. Control samples were treated with vehicle and perfused at flow rates of 2, 5, 10, 15 and 20 μL/minute in the apical-to-basal orientation. Higher flow rates were required for controls to consistently record pressure changes in the low range. For both treated and untreated samples, the pressure was continuously recorded for 6 hours to assure equilibrium at each flow rate. Compared to controls, TGFβ-2 perfusion increased transcellular pressure (Fig. 4.1.A) and significantly decreased (0.18 ± 0.03 versus 0.049 ± 0.01) the outflow facility per unit area across the 3D HTM (N=10, $P<0.001$) (Fig. 4.1.B). These results confirm that TGFβ-2 is capable of drastically affecting the transcellular pressure and outflow facility of our 3D HTM.

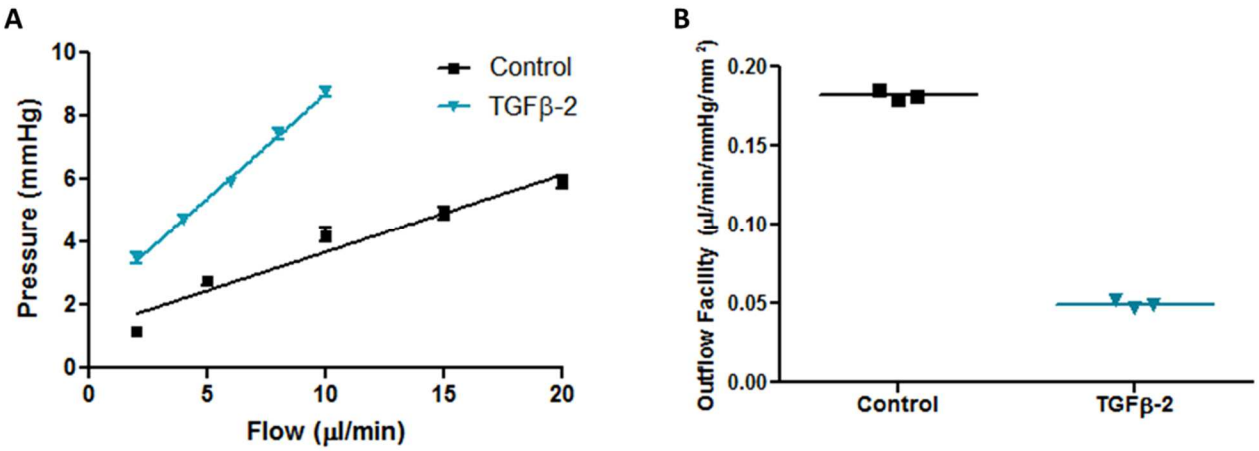

Figure 4.1. TGFβ-2 increases outflow resistance in 3D HTM cultures after 9-day treatment. (A) Pressure change as a function of flow rate. (B) Calculated outflow facility for HTM cultures treated with vehicle control (square) or TGFβ-2 (triangle).

4.3.2. TGFβ-2 enhances F-actin rearrangements and colocalizes α-smooth muscle actin to stress fibers

The cytoskeleton provides the framework for multiple cell functions including resisting deformation, coordination of forces that enable cell movement and control of shape [253]. Given the dynamic nature of the HTM, it is believed that HTM cells' cytoskeletal alterations may allow the effective control of aqueous humor outflow resistance. We applied our previously established, 3D-bioengineered HTM model to study changes in actin arrangement upon TGFβ-2 exposure. After primary HTM cells were grown on gelatin-coated SU-8 scaffolds for 14 days, as described previously [204], these 3D HTM constructs were conditioned overnight in 1% serum media and subsequently incubated for 9 days in the presence or absence of TGFβ-2 (2.5 ng/mL) While cells in vehicle-treated controls exhibited aligned actin fibers, TGFβ-2 treated samples showed increased staining of F-actin fibers that exhibited actin rearrangements

and appeared more disorganized, despite seemingly aligned nuclei (Fig. 4.2.). The actin expression was intensified in 3D HTM after treatment with TGFβ-2. No significant change in nuclei size between vehicle-treated controls (35 ± 3 μm^2, N=20) and TGFβ-2 treated samples (38 ± 4 μm^2, N=15) was observed. Given previous reports of the induction of α-SMA by this cytokine *ex vivo* and *in vitro* [254, 255], we further studied the expression of α-SMA in our model. Our studies confirm increased α-SMA after exposure to TGFβ-2 and interestingly, its colocalization with F-actin fibers. While our controls expressed diffuse α-SMA in the HTM cytosol, after TGFβ-2 treatment, this protein appears to be upregulated and arranged into fibers (Fig. 4.2.G). These changes in actin arrangements could have a direct impact on cell behavior and cell interactions with the microenvironment, including the ECM and neighboring cells.

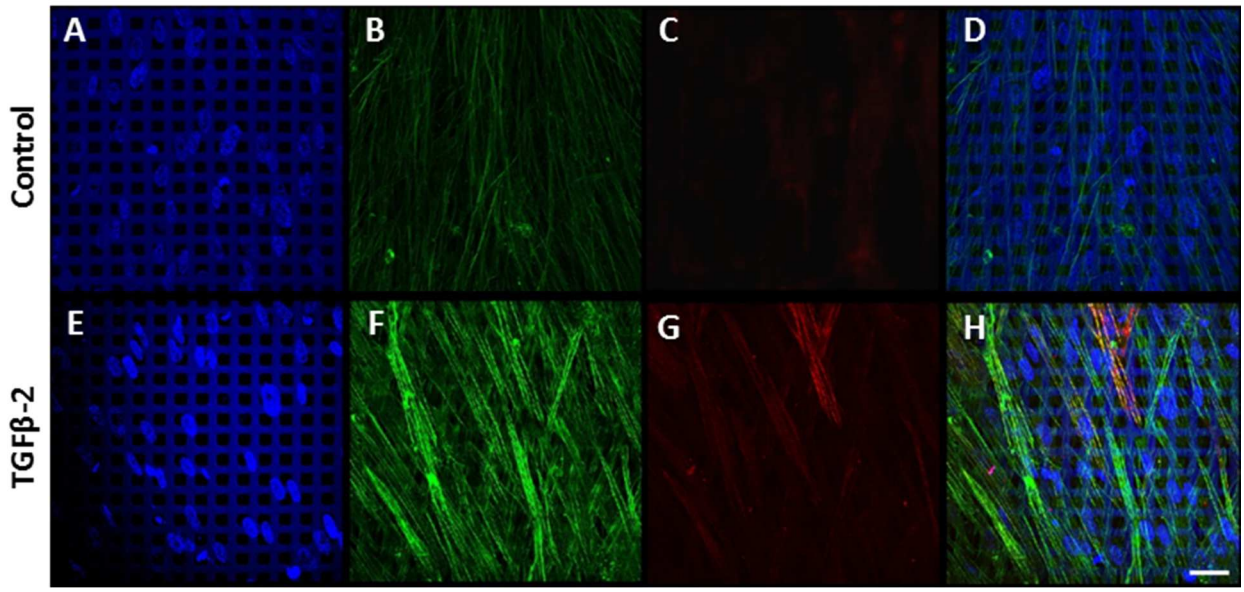

Figure 4.2. Confocal images of F-actin expression α-SMA localization in 3D HTM cultures after TGFβ-2 treatment for 9 days. (A-D) Vehicle-treated controls. (E-H) TGFβ-2 treatment. (A and E) DAPI-stained nuclei in blue. (B and F) Phalloidin-stained F-actin in green. (C and G)Immunocytochemistry of α-SMA in red. (D and H) Merged images. Scale bar = 30 μm.

4.3.3. Exposure of bioengineered 3D HTM to TGFβ-2 induces ECM deposition

Increased interest in the pathogenic, fibrotic expression of several ECM proteins in glaucomatous HTM encouraged us to evaluate the effect of TGFβ-2 on ECM protein expression in our bioengineered 3D HTM model. Fibrotic glaucomatous HTM is believed to result from the elevated amount of TGFβ-2 found in the aqueous humor [66, 256]. Exogenous treatment with TGFβ -2 increased the expression of ECM proteins, collagen type IV, fibronectin, and laminin, as shown by immunocytochemistry analysis (Fig. 4.3. A-J). After treatment with TGFβ -2, collagen IV fibers appeared highly disorganized and arranged into highly crosslinked bundles compared to vehicle-treated controls (compare Figs. 4.3.B and 4.3.G). Denser and thicker fibrous arrangements of fibronectin and laminin were seen after treatment with TGFβ -2, in which multiple fibers joined together (fibrils) longitudinally, making fibers appear thicker and denser compared to those seen in controls (compare Figs. 4.3.C and 4.3.H, Figs. 4.3.D and 4.3.I). Western blot analysis corroborated the induction of collagen IV and fibronectin in 3D HTM cultures after TGFβ-2 treatment (Fig. 4.3.K) and confirmed the significant increase in collagen IV ($N=4$, $P<0.01$) and fibronectin ($N=4$, $P<0.05$) proteins (Fig. 4.3.L). All together, these results not only support the involvement of TGFβ-2 in fibrotic HTM, as seen in several types of glaucoma, but also suggest the role of TGFβ-2 in tissue hardening that may take place as a result of crosslinked, dense arrangements of collagen IV, fibronectin and laminin.

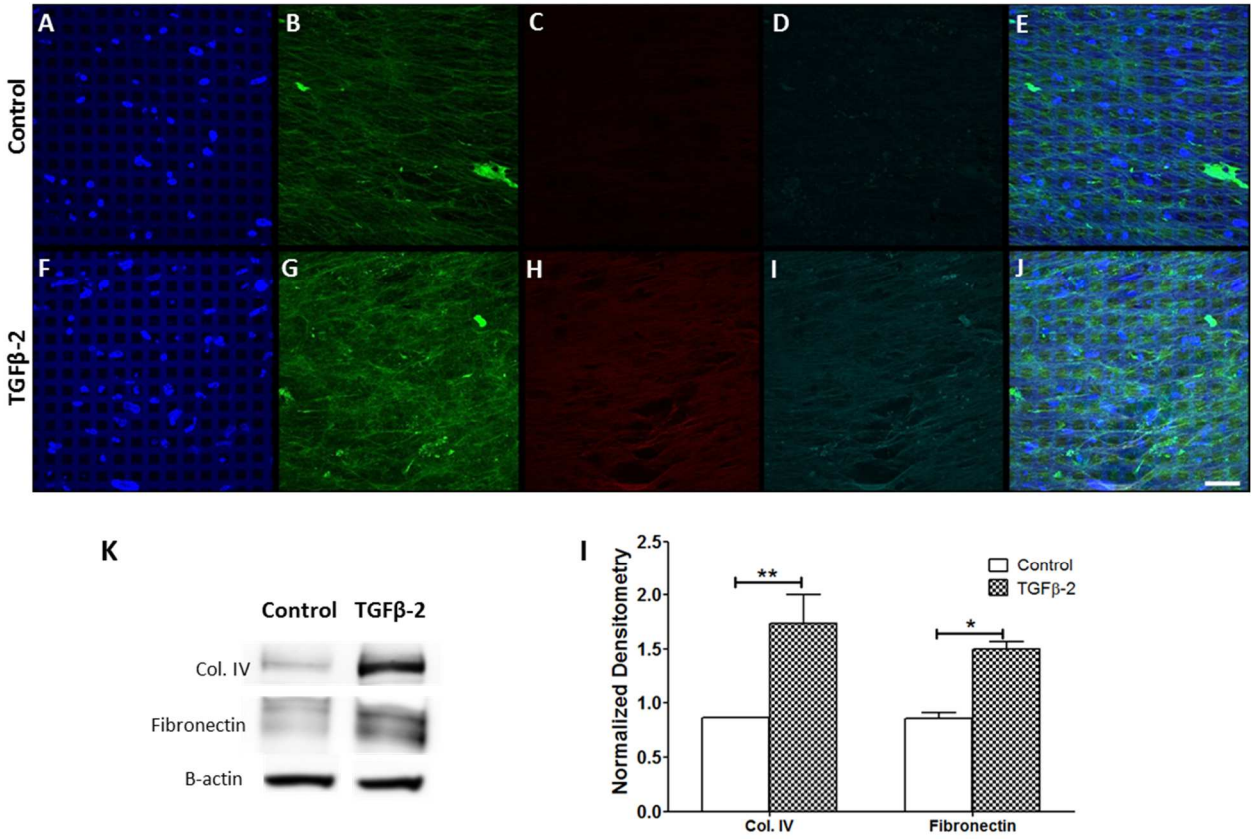

Figure 4.3. Induced expression of ECM proteins in 3D HTM cultures after perfusion with 2.5ng/mL TGFβ-2 for 9 days. (A-J) Confocal images of immunocytochemistry of 3D HTM perfused with vehicle control (A-E) or 2.5ng/mL TGFβ-2 (F-J). (A and F) DAPI-stained nuclei in blue. (B and G) Collagen IV in green. (C and H) Fibronectin in red. (D and I) laminin in cyan. (E and J) merged images. (K) Western blot. (L) Densitometry analysis of western blot of collagen IV and fibronectin (shown in K) normalized to β-actin. Scale bar = 30 μm. Asterisks indicate significance of difference from controls. **: $p<0.01$. *: $p<0.05$.

4.3.4. Extended exposure of TGFβ-2 induces expression of HTM-marker protein myocilin but not αB-crystallin

Despite decades of research in the field, myocilin and αB-crystallin are two characteristic, but poorly understood proteins that have been found in the HTM. Myocilin, a secreted protein known to interact with the ECM, apparently causes disease only in the eye [257]. αB-crystallin is a small heat shock protein with chaperone activity found mostly in the cribriform region of the HTM, the area adjacent to the inner wall of

the human Schlemm's canal (HSC), which is believed to exert the most pressure regulation [246] αB-crystallin expression increases after a few days of exposure to TGβ-2 [150]. However, the effects of extended exposure to TGFβ-2, e.g., a week or more, are unclear. We studied the effects of prolonged (9 days or more) TGFβ-2 exposure on the expression of myocilin and αB-crystallin using immunocytochemistry (Fig. 4.4.A-H) and Western blot analysis (Fig. 4.4.I and J). Confocal imaging showed an increase in myocilin protein expression in 3D HTM cultures after TGFβ-2 perfusion (Fig. 4.4.F) compared to vehicle-treated controls (Fig. 4.4.B).

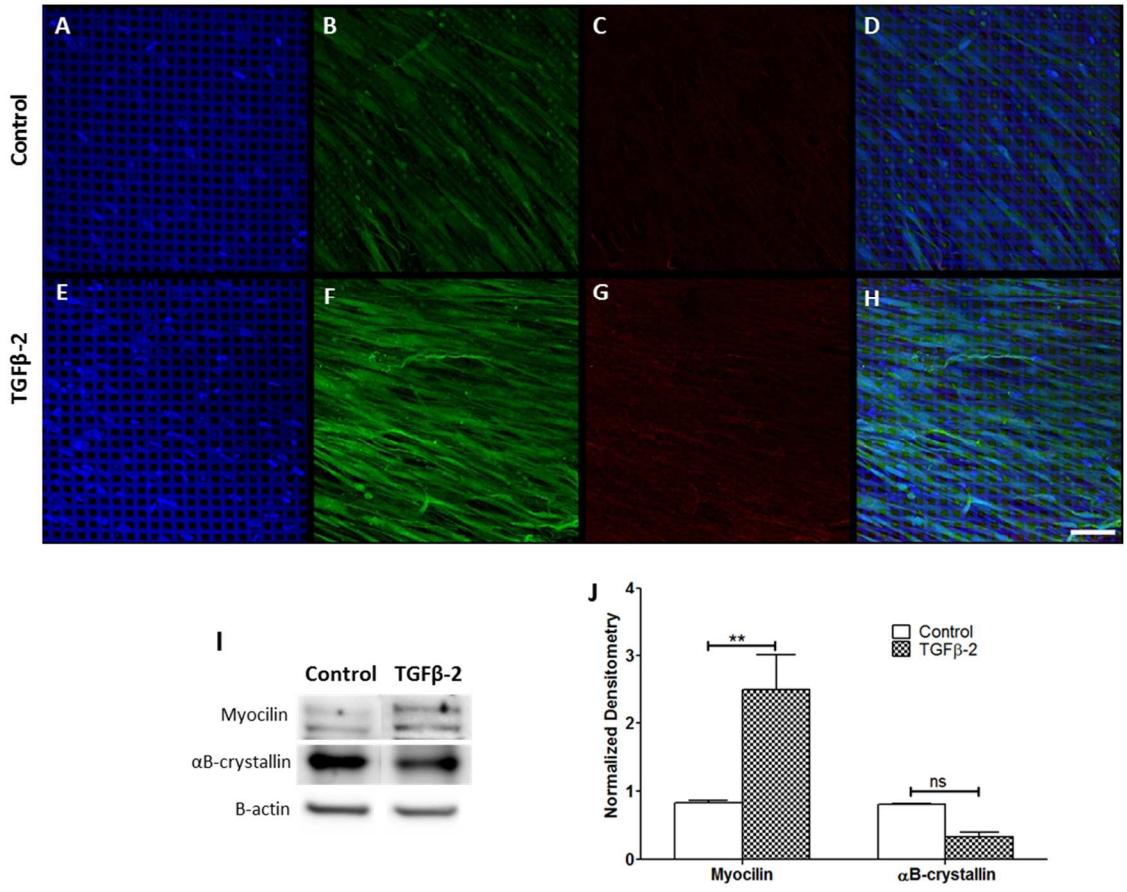

Figure 4.4. Expression of HTM marker proteins in 3D HTM cultures after treatment with 2.5 ng/mL TGFβ-2 for 9 days. (A-H) Confocal images of immunocytochemistry of myocilin (green) and αB-crystallin (red) after treatment with vehicle control (A-D) or 2.5 ng/mL TGFβ-2 (E-H). Scale bar = 100 μm. (I) Western blot. (J) Densitometry analysis of western blot of myocilin and αB-crystallin, normalized to β-actin. Asterisks indicate significance of difference from controls. **: $p<0.01$. n.s.: $p\geq0.05$.

The myocilin accumulation, induced by TGFβ-2, appeared punctate and occasionally plaque-like in areas between cells (Fig. 4.4.F). On the other hand, 3D HTM cultures treated with TGFβ-2 showed no change in αB-crystallin expression (Fig. 4.4.G) compared to control (Fig. 4.4.C). These results were confirmed by Western blot (Fig. 4.4.I) in which the densitometry analysis showed that expression of myocilin after TGFβ-2 treatment was significantly higher than control ($N=4$, $P<0.01$) while there was no significant difference in expression of αB-crystallin ($N=4$, $P>0.05$) (Fig. 4.4.J).

4.3.5. ROCK inhibitor prevents TGFβ-2-induced overexpression of ECM proteins and myocilin

ROCK inhibitors are currently being considered as a potential new class of glaucoma drugs. Despite extensive studies on their effects on the HTM, it is not clear whether ROCK inhibitors can correct TGFβ-2-induced fibrotic ECM build-up and myocilin over-expression, which have been linked to glaucoma. Therefore, we assessed the effect of co-administrating TGFβ-2 along with a ROCK inhibitor, Y-27632, on ECM protein secretion and myocilin expression. Immunocytochemistry analysis of our bioengineered 3D HTM model co-treated with TGFβ-2/Y-27632 for 9 days showed substantially decreased collagen IV and fibronectin expression compared to samples treated with TGFβ-2 alone (Fig. 4.5.A-L). In the Y-27632 co-treated samples, shorter collagen IV fibers and more aligned fibronectin fibers (Fig.4.5.I-L) were observed compared to samples treated with TGFβ-2 alone (Fig. 4.5.E-H).

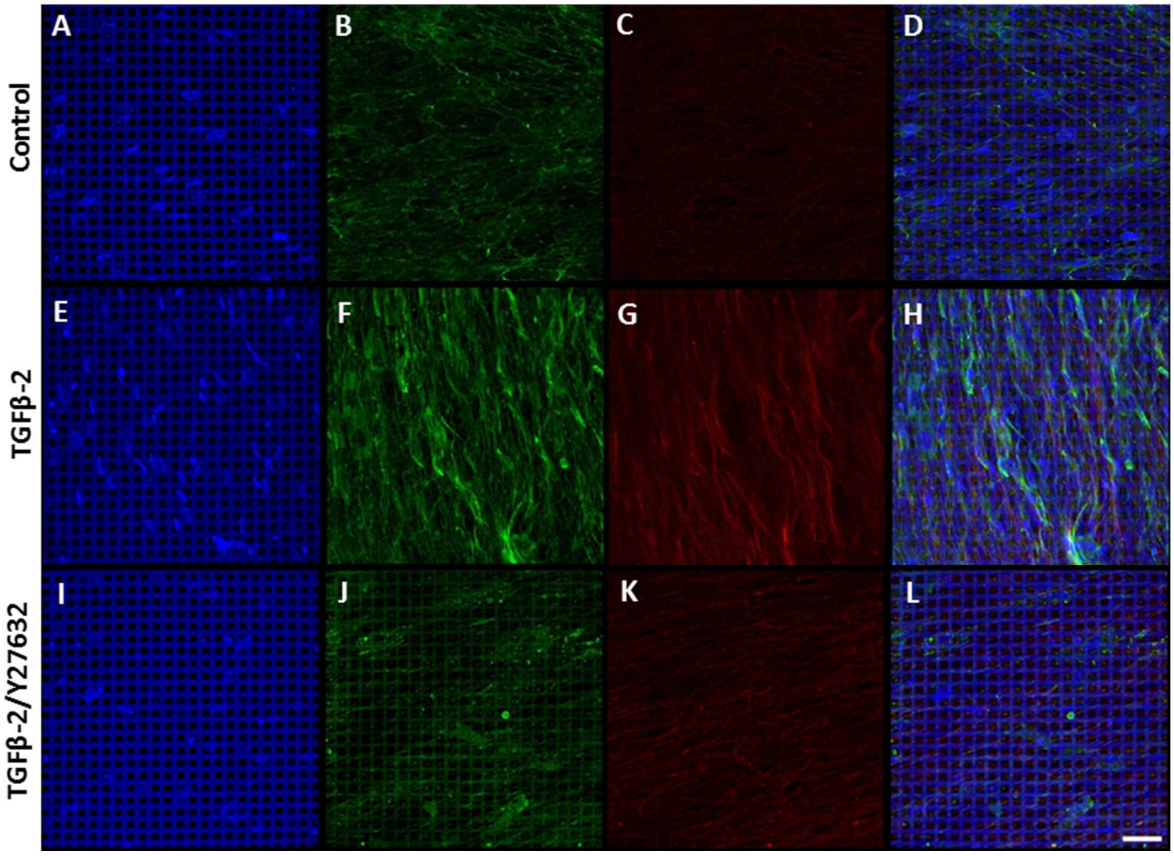

Figure 4.5. Confocal images of ECM protein expression in 3D HTM cultures after treatment with 2.5ng/mL TGFβ-2 in the absence or presence of 10 μM Y-27632 for 9 days. (A-D) Vehicle control. (E-H) TGFβ-2. (I-L) TGFβ-2/Y-27632. (A, E and I) DAPI-stained nuclei in blue. (B, F and J) Collagen IV (green). (C, G and K) Fibronectin (red). (D, H and L) merged images. Scale bar = 50 μm.

Similarly, treatment with TGFβ-2/Y-27632 combined, significantly reduced the expression of myocilin while slightly increasing the expression of αB-crystallin (Fig. 4.6.I-L) compared to treatment of TGFβ-2 alone (Fig. 4.6.E-H). Western blot analysis further confirmed these immunocytochemistry results, showing that TGFβ-2/Y-27632 treatment caused a significant decrease in ECM proteins, fibronectin ($N=5$, $P<0.05$) and collagen IV ($N=5$, $P<0.01$ for all) in comparison to TGFβ-2 alone, to the level of vehicle-treated controls or Y-27632-treated samples (Figure 4.7.), demonstrating that the presence of ROCK inhibitor could prevent the ECM accumulation caused by TGFβ-2.

Interestingly, treatment with either TGFβ-2 or Y-27632 alone induced overexpression of myocilin (Fig. 4.7.). This increase in myocilin expression was significantly suppressed by combined TGFβ-2/Y-27632 treatment when compared to vehicle-treated controls (N=6, P<0.001) and TGFβ-2 samples (N=6, P<0.001) (Fig. 4.7.). As mentioned previously, TGFβ-2 treatment slightly, but not significantly, decreased αB-crystallin expression (Fig. 3J). The presence of Y-27632 during TGFβ-2 treatment significantly increased αB-crystallin expression (N=6, P<0.05), bringing it back to the level of vehicle-treated control or Y-27632-treated samples. Compared to vehicle treated controls, TGFβ-2/Y-27632 combined treatments decreased myocilin (N=6, P<0.01) and increased fibronectin (N=5, P<0.05) expression (Fig. 4.7.). These results demonstrate that TGFβ-2 combined with the ROCK inhibitor counteracts the otherwise fibrotic effect of TGFβ-2, effectively lowering ECM protein accumulation and myocilin expression.

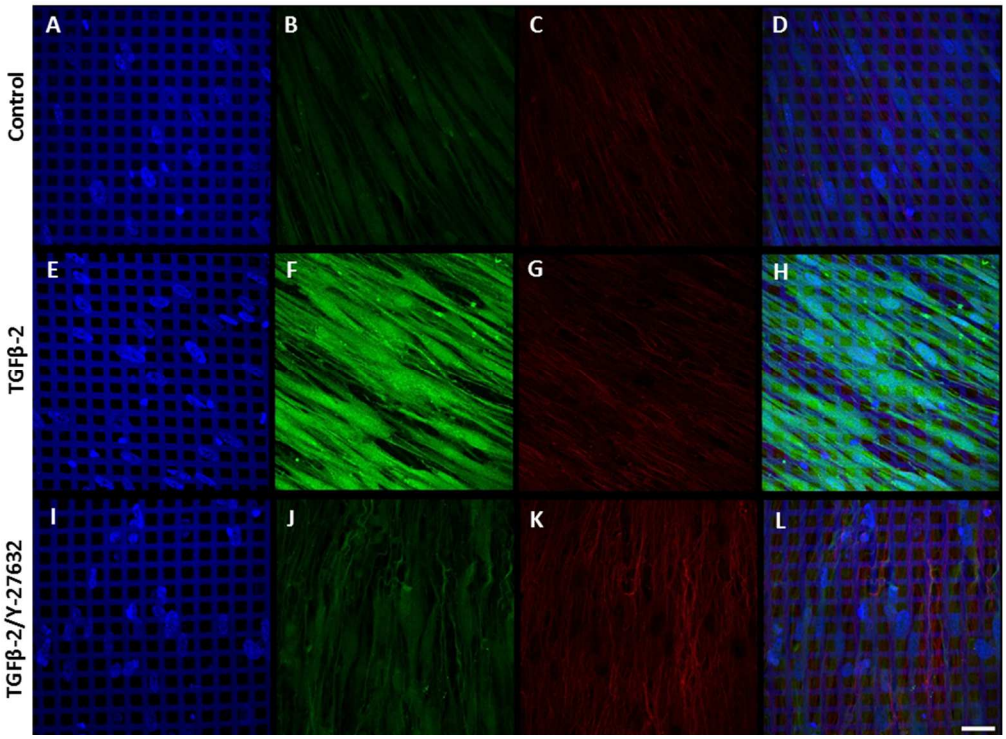

Figure 4.6. Confocal images of HTM-marker expression in 3D HTM cultures after treated with 2.5ng/mL TGFβ-2 in absence or presence of 10 μM Y-27632 for 9 days. (A-D) Vehicle control. (E-H) TGFβ-2. (I-L) TGFβ-2/Y-27632. (A, E and I) DAPI-stained nuclei in blue. (B, F and J) myocilin (green). (C, G and K) αB-crystallin (red). (D, H and L) merged images. Scale bar = 30 μm.

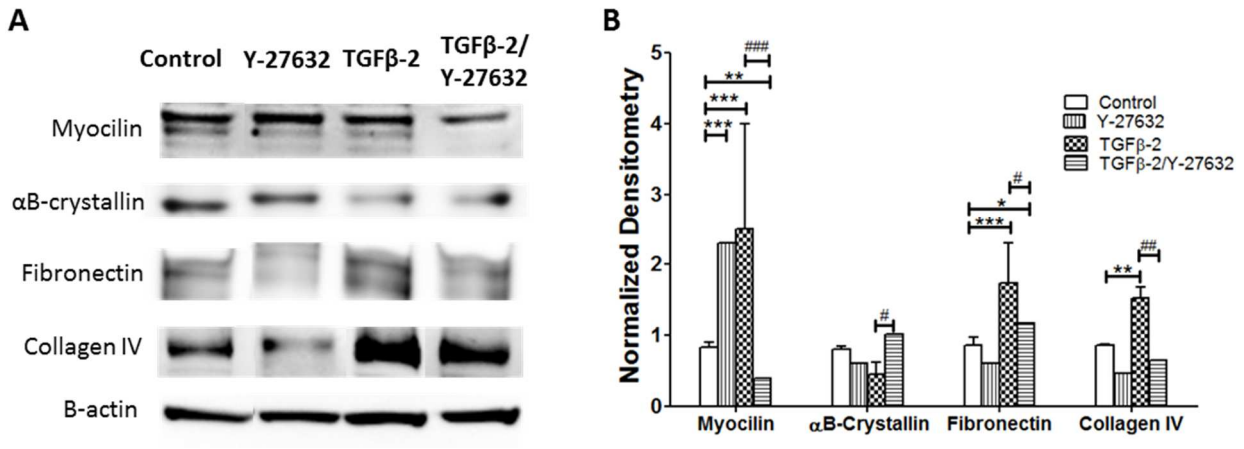

Figure 4.7. Expression of HTM-markers and ECM proteins in 3D HTM cultures treated with TGFβ-2 and/or ROCK inhibitor. (A) Western blot analysis of myocilin, αB-crystallin, fibronectin, collagen IV and β-actin for 3D-HTM scaffolds treated with vehicle-control, 10 μM Y-27632, 2.5 ng/mL TGFβ-2, or 2.5 ng/mL PA/10 μM Y-27632 for 9 days. (B) Densitometry analysis of western blot. Asterisks indicate significance of difference from controls ***p<0.001, ** p<0.01, * p<0.05. Hashmarks indicate significance of difference from TGFβ-2 treatment ### p<0.001, ## p<0.01, # p<0.05.

4.3.6. ECM Remodeling through MMPs and Cytokines in 3D HTM cultures treated with TGFβ-2 in the absence or presence of ROCK inhibitor

To explore the factors that may be responsible for modulation of the TGF-β induction of ECM and other secreted proteins by ROCK inhibitor, the transcriptional expression of several MMPs and cytokines, including tissue inhibitor of metalloproteinase-1 (TIMP-1), interleukin 1-alpha (IL-1α) and transforming growth factor-β 2 (TGFβ), were evaluated through a 9-day time course study. MMP-2 gene expression increased ~2.7-fold after a 3-day TGFβ-2 treatment compared to vehicle-treated controls (P<0.001) (Fig. 4.8.A). This increase was further enhanced to ~7.1-fold in TGFβ-2/Y-27631 co-treatment while Y-27631 treatment alone did not change MMP-2 gene expression. After 5 days in culture, TGFβ-2 treatment showed no significant difference in MMP-2 gene expression from vehicle-treated control while in TGFβ-2/Y-27631 co-treated samples, MMP-2 gene expression remained high (~5.1-fold increase

compared to control, P<0.001). Interestingly, MMP-2 expression decreased after 9 days treatment with Y-27631, TGFβ-2, or TGFβ-2/Y-27632 (P<0.001 for all treatments compared to control) (Fig. 4.8.A). MMP-3 expression showed no significant difference between control and TGFβ-2/Y-27632 treated cultures at day 3, while down-regulation in TGFβ-2 treated samples (~9.4-fold decrease, P<0.001) was observed. By day 5, MMP-3 expression was down-regulated ~15.3-fold (P<0.001) for TGFβ-2 treatment compared to control; the TGFβ-2 downregulation was suppressed by co-treatment with Y-27632 (Fig. 4.8.B). By day 9 of treatment, TGFβ-2 and TGFβ-2/Y-27632 significantly decreased MMP-3 mRNA expression by ~52- (P<0.001) and ~13-fold (P<0.05), respectively.

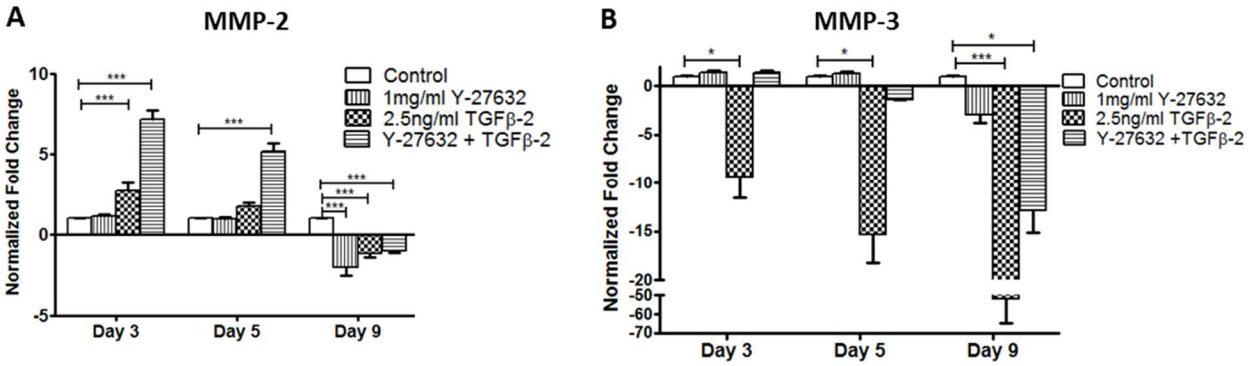

Figure 4.8. qPCR analysis of gene expression of MMPs in 3D HTM cultures after 3, 5 and 9 days of treatments with TGFβ-2 and/or ROCK inhibitor (Y-27632). (A) MMP-2. (B) MMP-3. Asterisks indicate significance of difference from controls ***p<0.001, ** p<0.01, * p<0.05.

HTM cells secrete several cytokines that modulate cell behavior and ECM turnover in the conventional outflow pathway. Increased cytokine expression has been observed in the aqueous humor of glaucoma patients, including TIMP-1 [215] and TGFβ [216, 217]. In addition, IL-1α is an inflammatory cytokine that has been shown to be involved in regulating outflow facility [86]. Therefore, studying cytokine expression

could provide insight into the pathology of glaucoma as pertaining to TGFβ-2. TIMP-1 mRNA expression was up-regulated ~7- fold after 3 days of TGFβ-2 ($P<0.001$) or TGFβ-2/Y-27632 ($P<0.001$) treatment. On day 5, TIMP-1 gene expression levels were still higher than controls, ~4-fold increased by TGFβ-2 ($P<0.001$) or TGFβ-2/Y-27632 combined ($P<0.001$). By day 9, TIMP-1 was down-regulated by ~2.5-fold ($P<0.001$) after TGFβ-2 and by ~1.5 ($P<0.001$) in TGFβ-2/Y-27632 treatments (Figure 4.9.A). Y-27632 treatment alone did not affect expression of TIMP-1, nor did the presence of Y-27632 change TGFβ-2-induced gene expression of TIMP-1. On the other hand, IL-1α gene expression exhibited no significant change after treatment with Y-27632, TGFβ-2, or Y-27632/TGFβ-2 for 3 and 5 days (Figure 4.9.B). On day 9, IL-1α mRNA expression decreased by ~7.7-fold for TGFβ-2 treated samples ($P<0.001$) while co-treatment with Y-27632 during TGFβ-2 treatment further down-regulated this gene by ~23-fold ($P<0.001$) (Fig. 4.9.B). Both treatments exhibited a time-dependent effect on IL-1α mRNA expression. As TGFβ-2 can also be produced and secreted by HTM cells, we evaluated its expression in the presence of exogenous TGFβ-2. TGFβ-2 gene expression was down-regulated throughout days 3, 5 and 9 of exogenous TGFβ-2 treatment by 7.4-, 4.4- and 3.2-fold, respectively. TGFβ-2/Y-27632 co-treatment initially (day-3) up-regulated TGFβ-2 gene expression by 1.3-fold and later, during 5 and 9 days of treatment, down-regulated TGFβ-2 mRNA expression by 1.4- and 1.6-fold, respectively compared to control (Fig. 4.9.C); however, in comparison with TGFβ-2 treatment alone, the expression in the co-treated cultures has much closer to control levels. Overall, these data demonstrate a complex ECM regulation that takes place as a result of elevated exogenous TGFβ-2 or TGFβ-2/Y-27632 exposure at the TM.

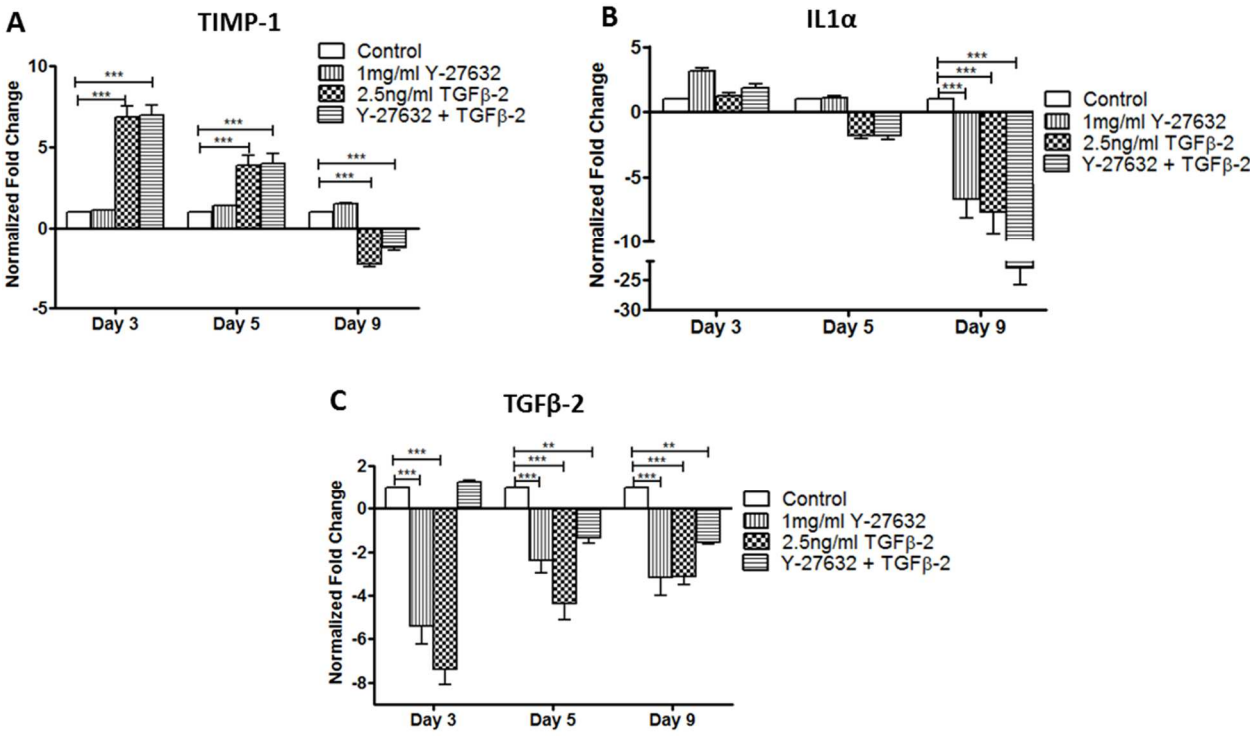

Figure 4.9. qPCR analysis of gene expression of cytokines in 3D HTM cultures after 3, 5 and 9 days of treatments with TGFβ-2 and/or ROCK inhibitor (Y-27632). (A) TIMP-1. (B) IL-1α. (C) TGFβ-2. Asterisks indicate significance of difference from controls ***p<0.001, ** p<0.01, * p<0.05.

4.3.7. ROCK inhibitor prevents TGFβ-2-induced elevated flow resistance

Given the dramatic changes in protein and cytokine expression resulting from the combined treatment with TGFβ-2 and ROCK inhibitor, we examined the effect of combined treatment on outflow facility through perfusion studies. As Y-27632 alone increases outflow facility, we compared vehicle-treated controls, TGFβ-2 treatment, Y-27632 alone, and Y-27632 in conjunction with TGFβ-2 in 3D HTM cultures. Compared to vehicle-treated controls, TGFβ-2/Y-27632 perfusion maintained a similar outflow facility as shown in Figure 4.9 (N=6, ns). Vehicle- and Y-27632-treated cultures showed an outflow facility of 0.184 ± 0.003 μL/min/mmHg/mm^2 and 0.23 ± 0.04 μL/min/mmHg/mm^2, respectively. On the other hand, TGFβ-2 treatment significantly

lowered the outflow facility of the bioengineered 3D HTM cultures to 0.049 ± 0.004 μL/min/mmHg/mm^2 (P<0.001) and TGFβ-2/Y-27632 treatment returned the outflow facility to 0.176 ± 0.008μL/min/mmHg/mm^2 (Fig. 4.10). These data demonstrate that the bioengineered 3D HTM regulates flow in a similar fashion as aqueous humor outflow regulation seen in *in vivo* and *ex vivo* HTM after TGFβ-2 treatment, by increasing pressure and decreasing the outflow facility across this tissue. In addition, combined TGFβ-2/Y-27632 treatment maintained "normal" outflow regulation comparable to the vehicle-treated bioengineered HTM. Altogether these data demonstrate that TGFβ-2 is capable of modulating outflow of the bioengineered 3D HTM comparably to *in vivo* and *ex vivo* HTM, and the presence of ROCK inhibitor Y-27632 during TGFβ-2 treatment can prevent TGFβ-2-induced elevation of transcellular pressure and maintain the outflow facility close to control levels. These data provide insight into the use of ROCK inhibitors to treat elevated IOP in glaucoma patients who have elevated TGFβ-2 in their aqueous humor.

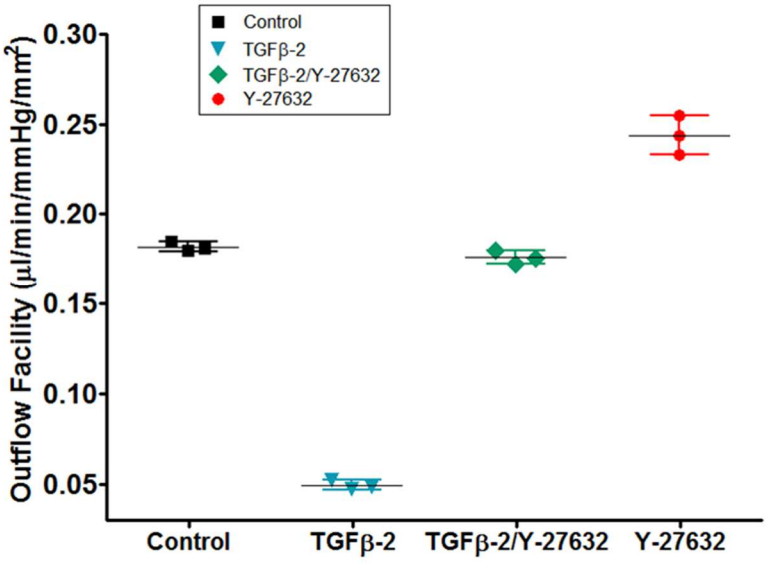

Figure 4.10. ROCK inhibitor neutralizes TGFβ-2-induced decrease of outflow facility in 3D HTM. Calculated outflow facility of perfused vehicle control (square), TGFβ-2 (inverted triangle), TGFβ-2/Y-27632 (rhombus), and Y-27632 (circle).

4.4. Discussion

In this study, we demonstrated that our bioengineered 3D HTM model responds to TGFβ-2 treatment similarly to *in vivo* or *ex vivo,* including elevated transcellular pressure, decreased outflow facility, and increased ECM accumulation. These data validate the utility of the 3D HTM model for perfusion studies of biological agents believed to affect the TM, in a physiologically relevant setting, which are otherwise difficult to conduct using *ex vivo organ cultures*. Using a bioengineered 3D HTM model system, we further demonstrated that TGFβ-2 affects a range of proteins that can elicit tissue hardening and outflow facility changes, including ECM, F-actin, and α-SMA. Lastly, we explored the potential of ROCK inhibitor in conjunction with TGFβ-2 to rescue the homeostatic behavior of HTM through MMPs and inflammatory cytokines.

The actin cell machinery polymerizes to form different network organizations that provide cells with mechanical elements and properties [258]. Filamentous actin such as stress fibers also connects the cytoskeleton to the ECM via focal adhesion sites. Treatment with TGFβ-2 caused cytoskeletal actin changes including polymerization of F-actin fibers and increased expression of α-SMA. After treatment, a majority of these F-actin fibers appeared to be organized into bundles, F-actin fibers at close proximity in relation to other fibers. Actin bundles have innate compressive mechanical properties that can be measured by their buckling force which is directly proportional to the number of actin filaments that make up a bundle [258]. In this way, tissues can increase their compressive force/strength through their actin arrangement. Based on our results, the induction of actin bundles suggests a more rigid cytoskeleton arrangement that can provide greater compressive forces to their microenvironment. Treatment of our 3D

HTM model with TGFβ-2 for 9 days also induced α-SMA overexpression and its rearrangement. α-SMA is a mechanosensitive protein, reported to be induced in response to critically stiffened cell mircroenvironments [259] and by exogenous TGFβs. Furthermore, α-SMA is co-localized or recruited to stress actin fibers under high tension, and localization of this protein from the cytosol to the stress fibers can be mediated under specific topographic cues that affect the structure of focal adhesions [260]. In this study, we observed increased expression of ECM proteins collagen IV, fibronectin and laminin, along with elevated expression of α-SMA after TGFβ-2 exposure. These induced ECM proteins together could substantially increase the stiffness of the immediate cell substrate, inducing the colocalization of α-SMA to the stress actin fibers as observed. Furthermore, fibronectin, via feedback activation, induces α-SMA expression [254]. Therefore, the increased expression of fibronectin seen in this work could also be involved in the increased α-SMA expression. Collectively, these observations further support the interplay between HTM cell contractile hardware and ECM-synthesis/deposition in the aqueous humor outflow pathway. In addition, the elicited expression of α-SMA and ECM proteins by TGFβ-2 suggests transdifferentiation of HTM cells into myofibroblast-like cells expressing fibrogenic and fibroblast-like markers, as recently reported by others[261, 262].

Increased ECM deposition in the TM is associated with POAG. Cell-ECM interactions play a key role in regulating outflow in the eye [18, 263]. The overproduction of ECM components such as fibronectin and collagen IV by HTM cells under pathological conditions has been described previously. For instance, we have shown that steroid treatment upregulates secreted and cell-associated ECM proteins,

including fibronectin, collagen type IV, and laminin in a 3D bioengineered HTM model [See Chapter 3]. Exposure to high glucose concentrations also induces fibronectin production by HTM cells [264]. In this work, ECM overproduction, including collagen IV, fibronectin, and laminin, was induced by TGFβ-2. These proteins are the major components of the HTM basement membrane and are found throughout the conventional outflow tract. ECM proteins are dynamically remodeled by several enzymes including MMPs. HTM cells constitutively express significant levels of MMPs, such as stromelysin-1 (MMP-3) and gelatinase A (MMP-2); expression can be further elevated in response to a variety of stimuli such as mechanical stretching and biologically active cytokines [211, 265]. Exposure to TGFβ-2 enhances accumulation of the pro form of MMP-3 and decreases active MMP-3 in the TM [266]. The unbalanced expression of MMP-3 may result in decreased proteolytic degradation and increased accumulation of ECM components such as fibronectin, a known MMP-3 substrate [267]. Indeed, in this study, exposure to TGFβ-2 led to a significant increase in fibronectin expression and decreased gene expression of MMP-3. Conversely, the active form of MMP-2 increased after three days of TGFβ-2 treatment [268]. Similar results were obtained in these studies, but over an extended 9 days of treatment, MMP-2 mRNA expression decreased, dropping well below the control levels. The initial increase in MMP-2 was accompanied by TIMP-1 induction. A direct relationship between MMP-2 and TIMP-1 has been described after cyclic mechanical stretching of bovine TM cells [269]. In our model, TGFβ-2 induces actin and ECM changes that can exert biomechanical stress on HTM cells leading to ECM turnover. Therefore, it is expected

that HTM cells may react to these stimuli by modulating MMP and cytokine expression; this response is attenuated during longer term exposure to TGFβ-2.

The initial (day 3) up-regulation of TIMP-1, along with the sustained down-regulation of MMP-3 during TGFβ-2 treatment could account for the accumulation of ECM proteins. The early upregulation of MMP-2 suggests an active ECM remodeling during early TGFβ-2 exposure, perhaps due to TM cells attempting to counteract protein overproduction. With extended exposure to TGFβ-2, MMPs and TIMPs are down-regulated, potentially leaving considerable paracellular accumulation of ECM proteins and myocilin at the HTM basement membrane. A similar trend in MMP gene expression was observed after extended TGFβ-2/Y-27632 co-treatment, but towards the beginning (day 3-5) MMP-2 was enhanced to a greater extent (over 2-fold) compared to TGFβ-2 treatment alone. This potent induction of MMP-2 gene expression could be sufficient to prevent or even disrupt proper assembly of proteins including myocilin and/or ECM proteins that require focal-adhesions. By the same token, given that IL-1α has been shown to regulate MMPs in the TM or organ cultures [86], down-regulation of this gene could induce the down-regulation of MMPs seen towards later days in this study.

RhoA/Rho kinase signaling activity affects the expression of ECM proteins and α-SMA [254], in addition to its well-recognized role in actin cytoskeletal organization. Using ROCK inhibitor, Y-27632, in combination with TGFβ-2, we assessed its effects on the expression of collagen IV, fibronectin, laminin, myocilin and αB-crystallin. This combination significantly decreased expression of ECM proteins as well as myocilin back to vehicle-treated controls levels, but failed to reduce αB-crystallin expression

compared to TGFβ-2 treatment. Interestingly, treatment with Y-27632 alone for 9 days upregulated myocilin and maintained unchanged levels of αB-crystallin compared to controls (Fig. 6). These results reinforce the anti-fibrotic nature, as related to ECM proteins, of ROCK inhibitors. On the other hand, these findings raise questions as to the relationship between myocilin, the ROCK pathway, and TGFβ-2 and elucidate their probable interplay. Based on this work and current literature, there are several changes caused by TGFβ-2 that may induce TM hardening eliciting elevated IOP (Fig. 4.11). Overall this work supports the idea that misregulated accumulation of ECM proteins, and perhaps myocilin, may influence the biomechanical properties and stiffness of TM cells, and therefore, aqueous humor outflow facility.

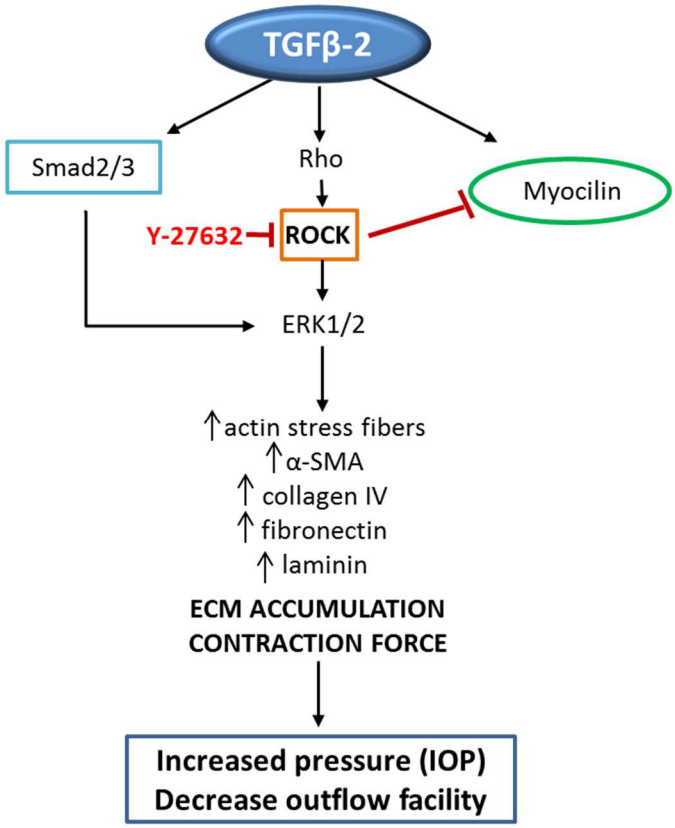

Figure 4.11. Schematic illustration of the effects elicited by TGFβ-2 that may induce IOP elevation. ROCK-signaling appears to regulate ECM synthesis/deposition and contractile activity by actin modulations. In the presence of TGFβ-2, bidirectional molecular interplay, potentially transcriptionally independent, appears to takes place between ROCK and myocilin.

CHAPTER 5

RECREATING THE CONVENTIONAL OUTFLOW TRACT USING 3D CO-CULTURE OF HTM AND HSC-LIKE CELLS

5.1. Introduction

The human conventional outflow tract is populated by two cell types, the trabecular meshwork (TM) and Schlemm's canal (SC). Before entering the venous system, the aqueous humor (AH) has to pass through the TM and then enter the inner wall of the SC [98]. Together, these structures are responsible for providing resistance to the outflow of the AH and maintain intraocular pressure (IOP) in the human eye [59]. The primary site of resistance in the conventional outflow tract is believed to reside, specifically, in the TM's juxtacanalicular region (JCT) and the inner lining of the SC [16, 270-273]. Cells of these regions, HTM and HSC, have many unique features and individual responsibilities that contribute to the overall generation and regulation of outflow resistance in both healthy and diseased conventional outflow tract. Several decades of extensive research, based on 2-D primary cell cultures of HTM and HSC cells, have contributed to better understanding the potential physiological and biological contributions of each cell type separately in the conventional outflow tract [99, 102, 274-279]. Although isolation of human trabecular meshwork (HTM) cells is now a fairly common technique implemented in several laboratories around the world, human Schlemm's canal (HSC) cell isolation has lagged behind. Thus far, HSC cells have only been isolated by a few groups using techniques that are not easily reproducible or have

limited success [98, 280, 281]. It possesses a major challenge when attempting to screen agents that can modulate these cells during the glaucoma drug discovery/pre-clinical testing process, due to the need of large amount of HSC cells as well as cell variability.

The SC cells are a unique type of cells. Although originated and directly connected to the blood vasculature system, they express an uncommon hybrid molecular phenotype, expressing proteins that are characteristics of both lymphatic and blood vessels [51, 52]. Recent advances in understanding developmental SC have demonstrated that most of the key features of the mature SC take place during postnatal processes. This process is described in detail in CHAPTER 1 section 1.3.2. In summary, soon after birth, SC cells are initially sprouts that emanate from the limbal vascular plexus and radial vessels (Fig. 1.4 A), then acting as active tip cells; they form tip cell clusters where not all of these cells are directly connected to the blood vessel (Fig. 1.4 B). Several tip cell clusters are formed from each parental sprout that emanated from the vessels and eventually all clusters combine to form a continuous flattened chain of cells that then becomes branched resembling vasculogenesis [51]. The unified flattened clusters transition into a tube and fuse with the TM. AH begins to flow through the tissue and has been shown to positively regulate the development and differentiation of the HSC [52]. During this process SC cells begin to express lymphatic markers, such as prospero homeobox protein 1 (PROX1), and a flattened core runs centrally (Fig. 1.4 D) [51]. Eventually higher level of lymphatic markers is expressed in the inner wall of the SC rather than its outer wall counterpart accompanying differentiation of the unique cell types in each wall (Fig. 1.4. F) [51]. Unlike cells in the

HSC outer wall, the inner wall cells adjacent to the HTM JCT, are long and thin, and are readily deformed by pressure changes in the eye. These differences between outer and inner wall cells of the HSC likely reflect inner wall cells specialization for mechanical sensing and AH outflow.

In this work, the possibility to use human microvascular endothelial cells (HMVECs) as an alternative source of HSC cells was explored. Given the vessel-vascular origin of HSC cells we chose to use HMVECs and attempted to differentiate them to HSC-like cells. In an effort to better mimic the conventional outflow tract, we bioengineered a 3-D co-culture construct which combines HTM and HMVEC cells. Moreover, this novel co-culture model was compared to its HSC counterpart and demonstrated similar protein markers, vacuole formation and does not hinder HTM-marker expression.

5.2. Materials and Methods

5.2.1. Primary Human Trabecular Meshwork Cell Culture

HTM cells were isolated from donor tissue rings discarded after penetrating keratoplasty. Isolation of the cells was performed under an IRB exempt protocol approved by the SUNY Downstate IRB. Isolation and culture conditions were as previously described [93, 96]. Before use in experiments, all HTM cell strains were characterized by expression of αβ-crystalline and α-smooth muscle actin. HTM cells were initially plated in 75 cm^2 cell culture flasks with 10% fetal bovine serum (FBS) (Atlas Biologicals, Fort Collins, CO) in Improved MEM (IMEM) (Corning Cellgro, Manassas, VA) with 1% 10mg/mL gentamicin. Fresh medium was supplied every 48

hrs. Cells were maintained at 37˚C in a humidified atmosphere with 5% carbon dioxide until 80-90% confluence which point cells were trypsinized using 0.25% trypsin/0.5 mM EDTA (Gibco, Grand Island, NY) and subcultured. At least three donors' human primary cell cultures were used during experiments. All studies were conducted using cells before the 5th passage.

5.2.2. Primary Human Microvascular Endothelial Cell Culture

Primary human microvascular endothelial cells isolated from neonatal dermis, were purchased from LifeTechnologies (Carlsbad, CA). The HTM cells were initially plated in Attachment Factor (LifeTechnologies, Carlsbad, CA) –coated 25 cm^2 cell culture flasks and cultured in 131 Medium supplemented with Microvascular Growth Supplement (MVGS) (Life Technologies, Carlsbad, CA). Fresh culture medium was supplied every 48 hrs. Cells were maintained at 37°C in a humidified atmosphere with 5% carbon dioxide until 80%-90% confluence at which point cells were trypsinized using 0.25% Trypsin/0.5 mM EDTA and subcultured. All studies were conducted using cells before the 4th passage.

5.2.3. Primary Human Schlemm's Canal Cell Culture

Primary human Schlemm's canal cells were isolated as previously described [98]. HSC cells were initially plated in 75 cm^2 cell culture flasks with 10% Premium Select Fetal bovine serum (PFBS; Atlanta Biologicals, Lawrenceville, GA) in Dulbecco's modified Eagle's medium (DMEM; Life Technologies, Carlsbad, CA) supplemented with penicillin (100 units/mL), streptomycin (0.1 mg/mL), and L-glutamine (0.292 mg/mL; Life Technologies, Carlsbad, CA). Fresh medium was supplied every 48 hrs. Cells were

maintained at 37˚C in a humidified atmosphere with 5% carbon dioxide until 80-90% confluence which point cells were trypsinized using 0.25% trypsin/0.5 mM EDTA (Gibco, Grand Island, NY) and subcultured. At two donors' human primary cell cultures were used during experiments. All studies were conducted using cells before the 4th passage.

5.2.4. Biomimetic Scaffold Fabrication

SU-8 2010 (MicroChem Corp.) was used to develop free-standing biomimetic porous microstructures that served as scaffolds on which primary HTM cells were cultured. Scaffolds were fabricated using standard photolithographic techniques as previously described [204] (Fig. 5.1). Briefly; a release layer was spin-coated on the wafer and baked at 150˚C. SU-8 2010 was applied by spin-coating to final thickness of 5 µm, then baked at 95˚C and cooled to room temperature. The resist was UV-exposed through a mask containing the desired pattern, baked at 95˚C and developed in PGMEA developer (MicroChem Corp.). SU-8 scaffolds with the desired features were released from the substrate, washed with acetone and sterilized using 70% ethanol. Given the abundant expression of hyaluronic acid (HA) at the HSC and previous studies reported by our laboratory on HSC cell attachment [282], sterile SU-8 scaffolds with 12 µm pores were coated with HA-based hydrogel coating. Briefly, Hystem-C hydrogel kit (ESI BIO, Alameda, CA) which contained thiol-modified sodium hyaluronate ("Glycosil"), thiol-modified gelatin ("Gelin S") and polyethelyne glycol diacrylate ("Extralink") were prepared in solution as per manufacturer's instructions. To form the hydrogel, Glycosil and Gelin S (1:1) were mixed, followed by addition of Extralink at 1:4 volume ratios (Extralink : Gelin S+ Glycosil). Porous SU-8 scaffolds were then dipped in the final

hydrogel solution; excess solution was removed from the scaffolds and allowed to gel at room temperature for 10-20 minutes.

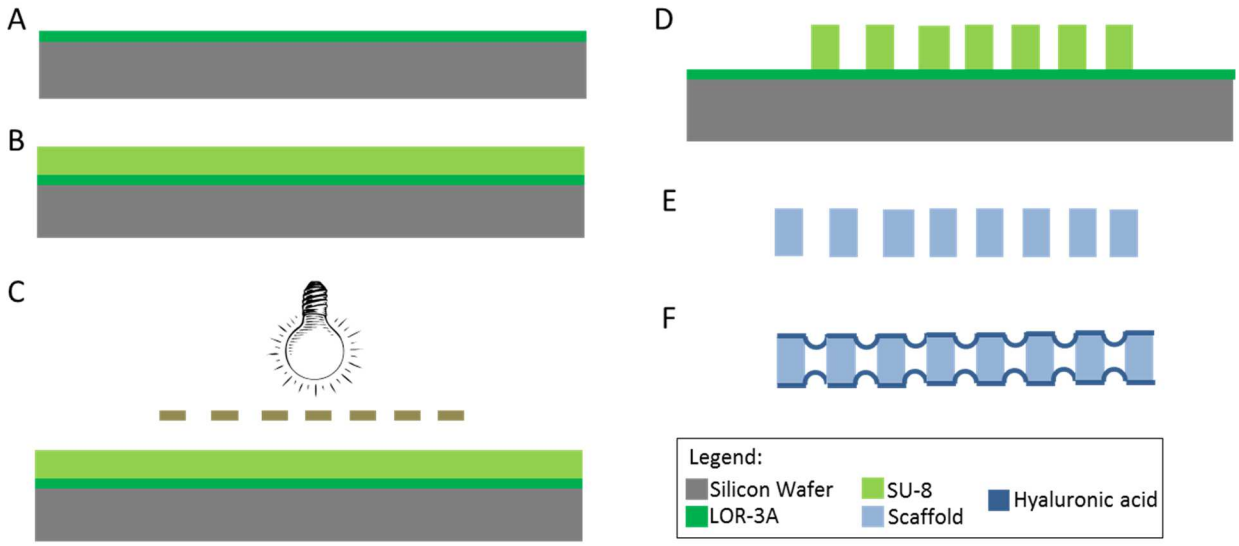

Figure 5.1. Fabrication of HA-coated SU-8 scaffolds. (A) Previously cleaned silica wafer is treated with LOR-3A. (B) SU-8 2010 coating. (C) UV-exposure using chrome mask. (D) Post-exposure bake. (E) Development and scaffold release from substrate. (F) SU-8 scaffolds coated with hyaluronic acid-based polymer

5.2.5. Culture of HSC and HMVEC Cells on Biomimetic Scaffolds

40,000 HMVEC or HSC cells were seeded on HA-coated SU-8 scaffolds and cultured for 7 or 14 days. HMVEC and HSC cells were cultured in 131 Medium supplemented with MVGS (LifeTechnologies, Carlsbad, CA) or DMEM supplemented with 10% PFBS, respectively. Additional media were used during experiments aimed towards studying the effect of biochemical stimuli on HMVEC cultures, including; 10% bovine aqueous humor in DMEM and HTM cell conditioned medium.

5.2.6. 3D Culture of HTM/HMVEC and HTM/HSC on Scaffolds

To create 3D constructs, 40,000 HTM cells were seeded on each microfabricated SU-8 scaffold in a well of a 24-well plate and cultured in 10% FBS-DMEM for 7 days. Medium was changed every 2-3 days. HTM constructs were then inverted and HMVEC or HSC cells (40,000 cells/sample) were seeded and cultured for additional 7 to 14 days.

5.2.7. Scanning Electron Microscopy

HTM, HMVEC, HSC, HTM/HSC and HTM/HMVEC samples were fixed with 3% glutaraldehyde solution in 0.1 M phosphate buffer containing 0.1 M sucrose for 2 hrs at room temperature. The samples were then rinsed three times in 0.1 M phosphate buffer, dehydrated in a graded ethanol series (50%, 70%, 80%, 95% and 100% ethanol) and slowly infiltrated with a graded hexamethyldisilazane (HMDS)-ethanol series (25%, 50%, 75%, 100% HMDS for 5, 5, 10, and 10 minutes; respectively) for drying, and then samples were sputter-coated to prevent charging. Samples were observed under a LEO 1550 field emission scanning electron microscope (SEM) (Leo Electron Microscopy Ltd, Cambridge, UK) as described previously [204]. All images were taken using the same electron beam energy.

5.2.8. Immunocytochemistry Followed by Confocal Microscopy

After 7 or 14 days in culture, constructs were fixed, permeablized, and stained for F-actin cytoskeleton using phalloidin (Life Technologies) or incubated with antibodies against HTM markers myocilin, and αB-crystallin, HSC-marker PECAM-1, VE-cadherin and fibulin-2, and ECM proteins, collagen type IV, fibronectin and laminin (Abcam)

(Table 5.1.), as described previously [204]. Appropriate secondary antibodies were used for each protein (Table 5.1.). Laser scanning confocal microscopy was performed using a Leica SP5 confocal microscope, and images were acquired at 40 X and 63 X magnifications with an oil-immersion objective. Confocal images were processed using Leica LasAF software, and all confocal images within a given experiment were captured using the same laser intensity and gain settings in order to be able to compare intensities across samples.

Name	Specie	Dilution	Company	Secondary Antibody
Alexa-488 conjugated Phalloidin	-	1/100	Life Technologies	-
CD-31 (PECAM-1)	mouse	1/200	Abcam	Goat anti-mouse 594
Fibulin-2	Goat	1/200	Santa Cruz Biotechnology	Donkey anti-goat 647
VE-cadherin	Rabbit	1/500	Cell Signaling	Goat anti-rabbit 488
Collagen type IV	Rabbit	1/500	Abcam	Goat anti-rabbit 488
Fibronectin	Mouse	1/200	Abcam	Goat anti-mouse 594
Laminin	Chicken	1/500	Abcam	Goat anti-chicken 633

Table 5.1. Primary antibodies used during this study.

5.2.9. Vacuole Induction

A perfusion apparatus was used as previously described [204]. HTM/HSC and HTM/HMVEC samples were securely placed in the perfusion chamber and perfused at 5 µl/min for 2 hrs. Samples were perfused in a basal-to-apical direction with perfusion medium consisting of Dulbecco's modified Eagle's medium (DMEM) (Cellgro) with 0.1% gentamicin (MP). The temperature was maintained at 34˚C. The perfusate was then switch to 3% glutaraldehyde solution in 0.1 M phosphate buffer containing 0.1 M sucrose (SEM fixative). Fixed samples were then dehydrated and prepared for SEM imaging as described in section 5.2.7. Vacuole/ pore size were measured using the

embedded LEO electron microscopy image software. Four different samples per condition including HSC cells from two donors and HTM from three donors were studied for these experiments.

5.2.10. Quantitative Real-Time PCR (qPCR) Analysis

Total RNA was extracted from samples using an RNeasy Plus Mini kit (Qiagen Inc., Valencia, CA). RNA concentrations were determined using a NanoDrop spectrophotometer. 50 ng of RNA per sample was used for each qPCR experiments. qPCR was carried out using TaqMan RNA-to-CT™ 1-Step Kit (Applied Biosystems, Carlsbad, CA) and performed on an AB StepOnePlus Real Time PCR system (Life Technologies, Carlsbad, CA) using primers for αB-crystallin, PECAM-1, fibulin-2, collagen type IV, fibronectin, laminin and GAPDH (Table 5.2.).The temperature profile was as follows: 48˚C for 15 min (reverse transcription step), followed by an enzyme activation step of 95°C for 10 min, 40 cycles of 15 s denaturation at 95°C and 1 min anneal/extend at 60°C. Relative quantitation data analysis was performed using the comparative quantification method, ΔΔCt, with GAPDH as the endogenous reference. All samples were normalized to GAPDH. q-PCR experiments were performed in triplicate (technical replicates) and from duplicate biological experiments using three donor cells. Average values are presented as mean ± SD.

NCBI Gene symbol	Ref. Sequ. number	Forward Primer	Reverse Primer
CRYAB	NM_001885	CAATCACATCTCCCAACACCT	CTGGTTTGACACTGGACTCTC
PECAM-1	NM_000442	ATTGCTCTGGTCACTTCTCC	CAGGCCCATTGTTCCC
FBLN2	NM_001165035	CCAGGCACTCGTCATTGTC	CCAACTCTGTCCATTCTATCCC
COL4A1	NM_001845	CCTTTGTGCCATTGCATCC	GAACAAAAGGGACAAGAGGAC
FN1	NM_054034	GTCCTTGTGTCCTGATCGTTG	AGGCTGGATGATGGTAGATTG
LAMA4	NM_001105206	AGTGCTCTCCTGTTGTGTTC	GAATGTGTGCCCTGCGA
GAPDH	NM_002046	TGTAGTTGAGGTCAATGAAGGG	ACATCGCTCAGACACCATG

Table 5.2. Primer sequences used in qPCR analysis.

5.2.11. Statistical Analysis

Data were expressed as the average ± standard deviation. The difference between HTM/HSC and HTM/HMVEC samples was analyzed using two-way ANOVA followed by Bonferroni post-tests (GraphPad Prism 6.02; GraphPad Software, Inc., La Jolla, CA). P values $P<0.05$ and $P<0.001$ considered significant and highly significant, respectively.

5.3. Results

5.3.1. Cultivation and characterization of HMVECs grown on micropatterned, well-defined, porous SU-8 scaffolds

Given that HSC cells have a mesodermal and vascular origin, we attempted to exploit HMVEC differentiation as a potential HSC-like cell source during the development of a more complex system that mimics the conventional outflow tract in addition to the HTM. We first characterize HMVECs in terms of their morphology and protein expression. Compared to HTM and HSC cells, HMVECs present polygonal, cobblestone-like morphology and form a thin cell monolayer with distinct junctions formed between cells, while HTM and HSC cells were elongated and have rougher cell topography (Fig. 5.2). Furthermore, HTM cell layer was distinctively thicker than HMVEC and HSC layer, appearing less translucent under the same electron beam energy in the SEM.

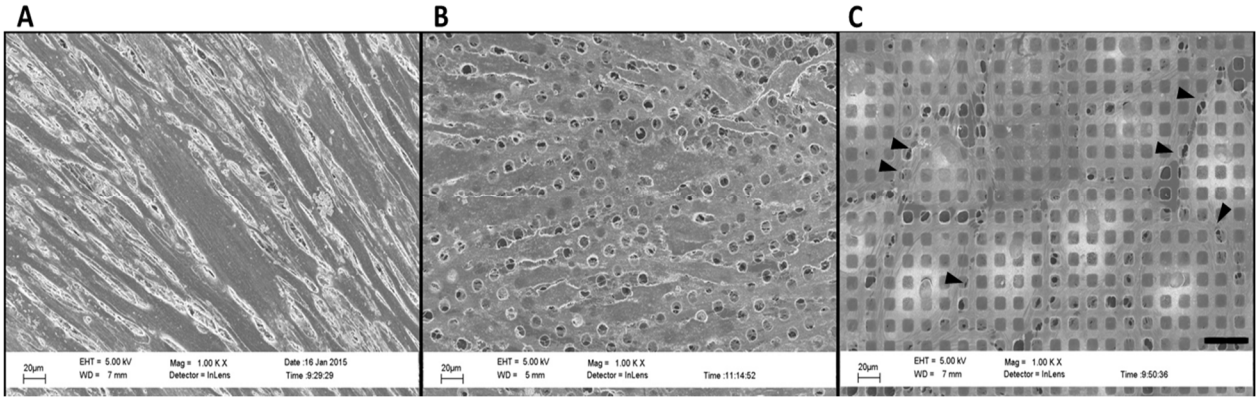

Figure 5.2. HTM, HSC and HMVEC cells cultured on HA-coated SU-8 scaffolds. Scanning electron micrographs of cells cultured on scaffolds for 14 days. (A) HTM cells. (B) HSC cells. (C) HMVEC cells. Arrow heads: cell junctions.

HMVEC's polygonal morphology was confirmed by phalloidin-stained F-actin expression, revealing the stress actin fibers that make up the cytoskeleton. Many of

these actin fibers appeared crosslinked, forming vertices and bundles and interconnecting multiple F-actin fibers at one point (Fig. 5.3A). Analysis of HMVEC protein expression demonstrated that these cells maintained their vascular markers and expressed adheren proteins such as PECAM-1 (Fig. 5.3). PECAM-1 was expressed throughout these cells and mostly also in the intercellular spaces or junctions between cells. Fibulin-2, a secreted glycoprotein, was also expressed by HMVECs and its pattern appeared similar to that of PECAM-1. Cross-section of HMVEC layer revealed fibulin-2 diffused throughout the thickness of the cell layer and mostly basal and extracellular expression compared to PECAM-1 (Fig. 5.3B). These results demonstrated the feasibility of culturing HMVECs on HA-coated SU-8 scaffolds, maintaining their innate cobblestone morphology and endothelial markers. The morphology of these cells cultured alone differed greatly from HTM and HSC cells (Fig. 5.2.).

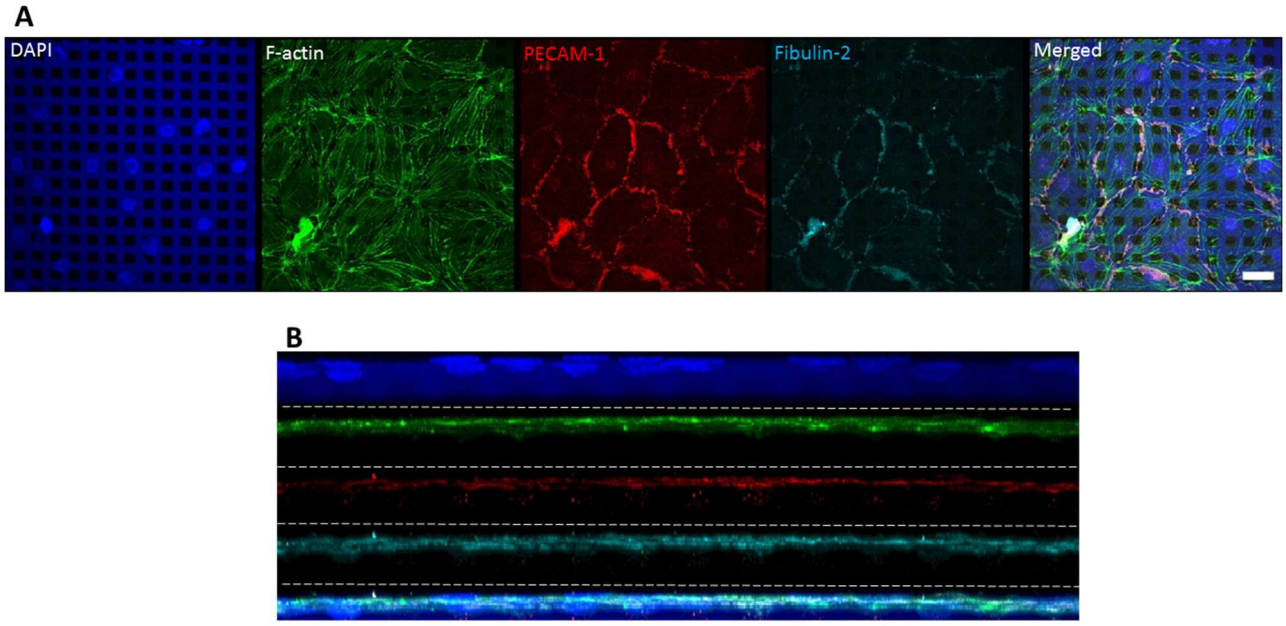

Figure 5.3. Characterization of HMVECs grown on SU-8 scaffolds. (A) Top-down Z-stack and (B) cross-sectional confocal imaging of phalloidin-stained F-actin cytoskeleton (green), PECAM-1 (red) and fibulin-2 (cyan) co-stained with DAPI (blue) of HMVECs cultured on scaffolds for 14 days.

5.3.2. Differential expression of HSC-marker proteins in HMVECs cultured on SU-8 scaffolds

We further compared HMVEC and HSC cell-marker expression to investigate their similarities and differences. To characterize the common markers between these two cell types, we used immunocytochemistry against HSC-markers after 7 days of cell culture, including VE-cadherin, PECAM-1 and fibulin-2 (Fig. 5.4). Additionally, as a negative control and to distinguish potential contamination during isolation of HSCs, we stained cells for the HTM specific marker αB-crystallin. HSC cells expressed VE-cadherin greatly in the nuclei as well as at the edges of the cells, with a spindle-like appearance mostly found towards the thin edges of the cells (Fig. 5.4A top panel). HMVECs expressed VE-cadherin in a different pattern, mostly towards the edges of these round cells (Fig. 5.4A bottom panel). In particular, no nuclear expression of VE-cadherin was observed in HMVECs. The opposite was revealed when comparing PECAM-1 expression in HMVEC and HSC cells. Mostly nuclear expression of this protein was observed in HMVECs while HSCs expressed cytoplasmic diffused PECAM-1, delineating the elongated morphology of these cells (Fig. 5.4B). FIbulin-2 was also expressed in both cell types (Fig. 5.4B). In HSCs, fibulin-2 was expressed extracellularly all through the scaffolds. HMVECs expressed fibulin-2 to a lesser extent than that seen in HSCs, and it appeared to be mostly secreted under the nuclear areas of these cells. αB-crystallin, used as negative control since this protein is expressed in HTM, was not expressed by neither HSCs nor HMVECs. The results presented in this section demonstrated that despite morphological differences, HMVECs express HSC-markers. There are differences in the expression pattern of VE-cadherin, PECAM-1

and fibulin-2. It is important to keep in mind when studying the functional aspects of these cells during our following studies.

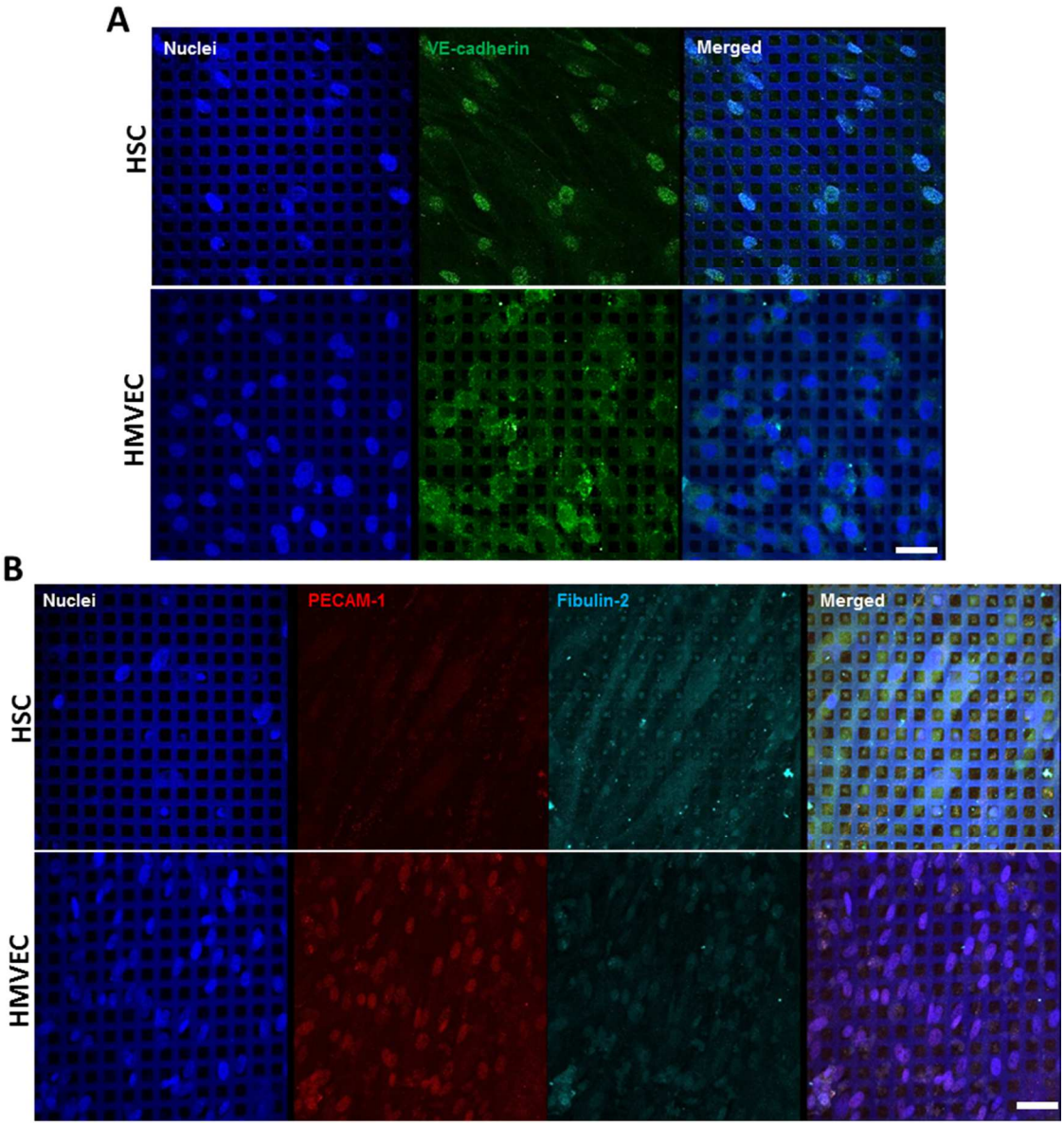

Figure 5.4. HMVE cells express HSC-markers with differ patterns. HSC (A and B top panels) and HMVEC (A and B bottom panels) cells cultured on SU-8 scaffolds. Immunocytochemistry stained with VE-cadherin (A; in green), PECAM-1 (B; in red) and fibulin-2 (B; in cyan). Scale bar = 30 μm.

5.3.3. Feasibility of differentiating HMVECs into HSC-like cells using exogenous biochemical cues

In order to explore the possibility to use HMVECs as an alternative source of HSC cells, we first examined the effect of exogenous biochemical cues on HMVEC growth and potential HSC-like morphogenesis, including HMVEC medium, HTM medium, HTM cell-conditioned medium, and aqueous humor. HMVEC medium was used as a negative control, which is the standard medium for endothelial cell maintenance and is composed of medium 131, supplemented with MVGS (4.9% FBS, 1 µg/mL hydrocortisone, 3 ng/mL human fibroblast growth factor, 10 µg/mL heparin, 1 ng/ml human epidermal growth factor and 0.08 mM dibutyryl cyclic AMP). HTM medium, which is used to maintain HTM morphology and function and composed of 10% FBS in DMEM, was used to see if it is sufficient to induce HSC-like morphology. Given that HTM cells are known to secrete several cytokines and growth factors into their microenvironment, cell-conditioned medium was also used to provide biochemical cues for potential HMVEC differentiation. Additionally, aqueous humor, known to provide nutrients to TM, was used to offer *in vivo*-like biochemical cues at 10% bovine aqueous humor in DMEM. After 7 days of culture, SEM analysis demonstrated HMVECs reached confluence and retained their innate cobblestone morphology in HMVEC medium (Fig. 5.5A), HTM medium (Fig. 5.5B) and HTM cell-conditioned medium (Fig. 5.5C). As far as AH is concerned, HMVECs achieved elongated morphology similarly to HSC cells (Fig. 5.5D). However, cells failed to reach confluence (only about 20-30% cell coverage). Additionally, HMVECs grown in HTM cell-

conditioned medium and aqueous humor were also noted to appear slightly thicker than those grown in HMVEC medium and HTM medium under same imaging conditions.

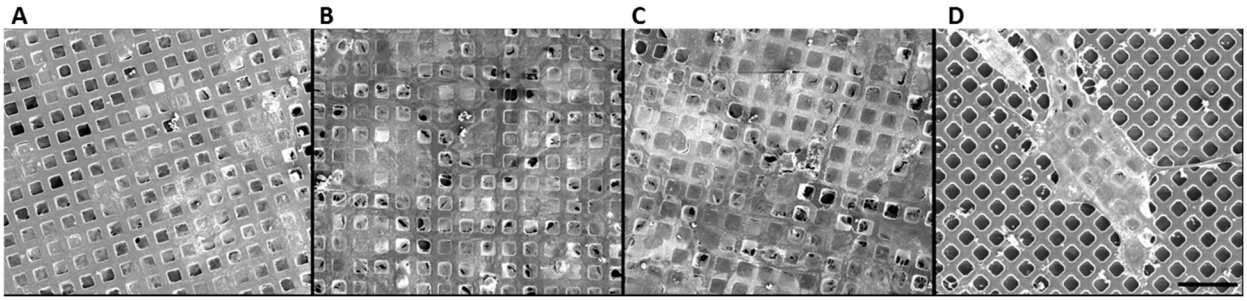

Figure 5.5. **Effect of media on HMVECs differentiation.** Scanning electron micrographs of HMVECs cultured with different media for 7 days in an attempt to induce cell-morphology changes. (A) 131 media. (B) HTM media. (C) HTM cell-conditioned media. (D) Aqueous humor.
Scale bar = 50 µm.

Furthermore, HMVECs grown on scaffolds in different media were stained with phalloidin to reveal cytoskeleton and immunostained with antibodies against PECAM-1 and fibulin-2. On day 7 the F-actin cytoskeleton of HMVECs in HMVEC medium appeared to be organized into short, unaligned stress fibers while PECAM-1 and fibulin-2 delineated cobblestone-like junctions and were also found diffused throughout cytoplasm (Fig. 5.6A). HTM medium induced cell retraction, in which some cells appeared slightly elongated with gaps between cells, exhibiting diffuse and nuclear expression of PECAM-1 and fibulin-2 (Fig. 5.6B). Similarly to HMVEC medium, HTM cell-conditioned medium induced short, unaligned stress fibers and increased cortical F-actin staining, in which PECAM-1 and fibulin-2 outlined cell junctions and revealed larger polygonal cell shapes compared to cells cultured in HMVEC medium (Fig. 6C). Aqueous humor induced F-actin filament remodeling, and as presented on our SEM findings, caused HMVECs to elongate but failed to reach cell confluence (Fig. 5.6D).

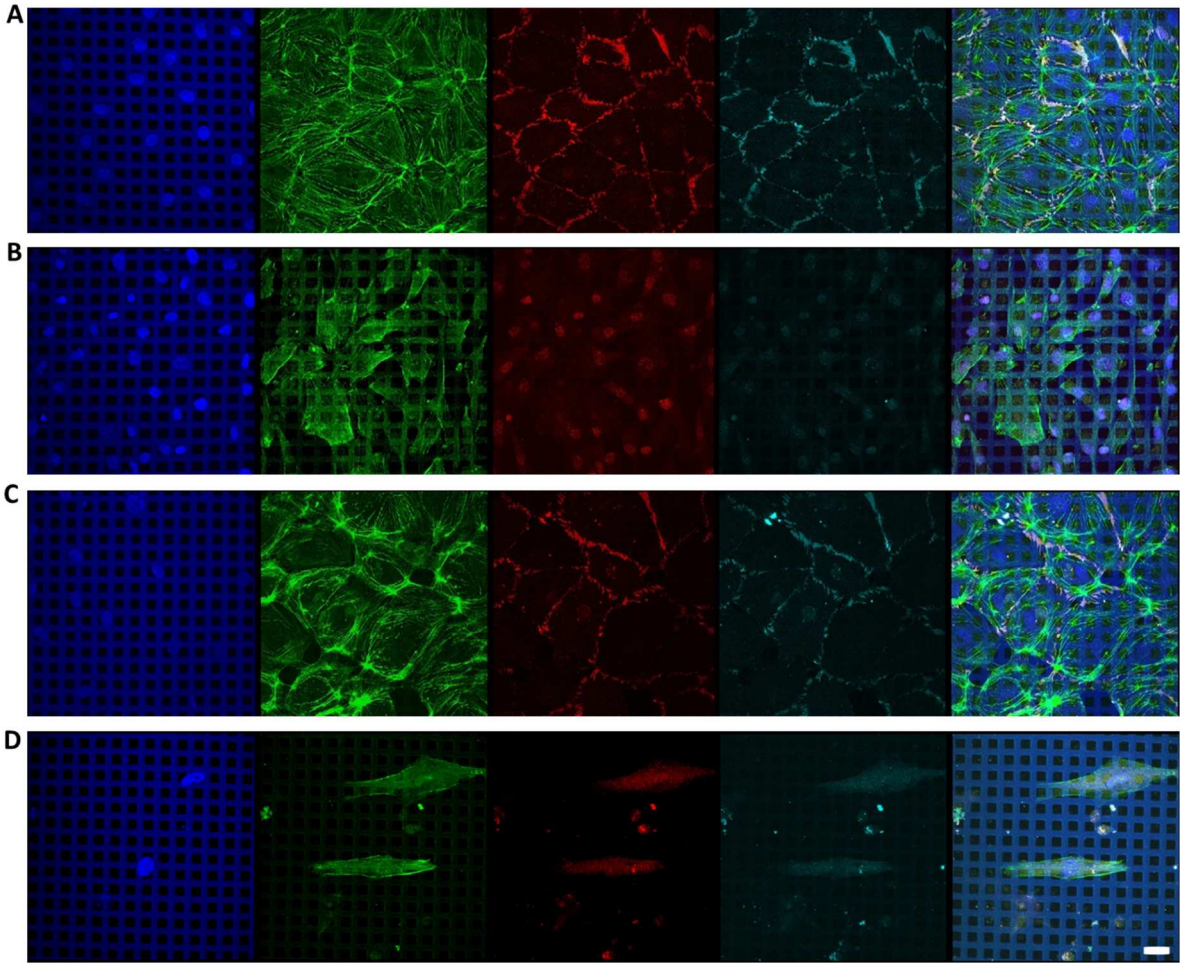

Figure 5.6. Effect of media on HMVECs expression of HSC-markers after 7 days. Confocal images of HMVECs cultured with (A) HMVEC medium, (B)HTM medium, (C)HTM cell-conditioned medium, and (D) aqueous humor. Blue: DAPI stained nuclei. Green: F-actin. Red: PECAM-1. Cyan: fibulin-2. Scale bar = 30 μm

By day 14, HMVEC medium and HTM medium induced formation of dissorganized longer stress fibers, some of which formed into denser microfilamentous fibers (Fig 5.7 A-B) compared to the arrangement described by day 7 of culture. In addition, PECAM-1 and fibulin-2 expression, bordering the cell shape, was intensified in HMVEC medium and was greatly decreased in HTM medium. HTM cell-conditioned medium in contact with HMVECs for 14 days maintained cortical F-actin expression and preserved PECAM-1 and fibulin-2 at cell junctions (Fig. 5.7C). On the other hand,

HMVECs in aqueous humor at day 14 remained elongated with stress actin fibers running along the full length of the cell, some of which appeared punctate, at the same time, cells presented diffuse expression of PECAM-1 and fibulin-2 with slightly higher nuclear expression (Fig. 5.7D). Confluence was not reached even after 14 days of culture in aqueous humor suggesting that although AH can induce HMVEC morphological changes, it may hamper cells proliferation dramatically. Therefore, all together, these results suggest that biochemical cues alone are not sufficient to effectively and consistently induce HSC-like differentiation of HMVECs into a HSC-like monolayer.

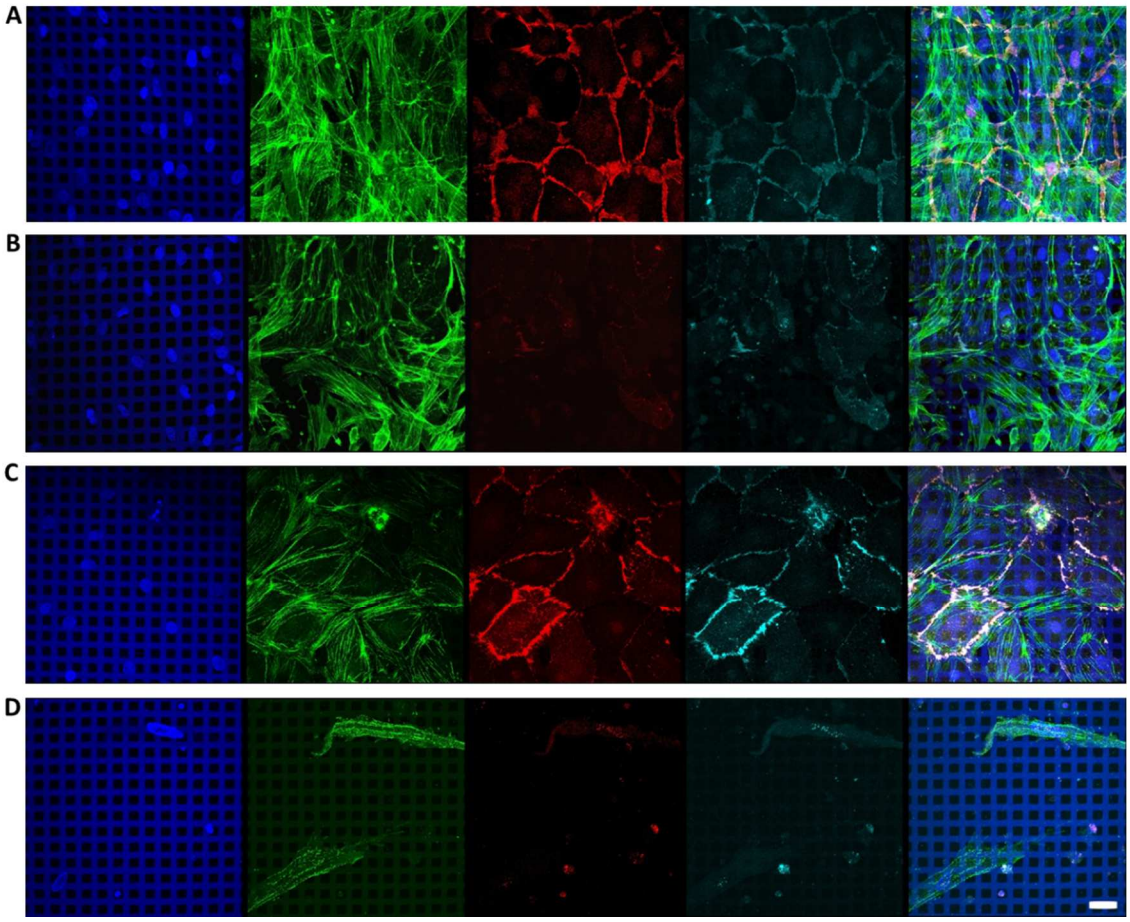

Figure 5.7. Effect of media on HMVECs expression of HSC-markers after 14 days. HMVECs cultured with HMVEC medium (A), HTM medium (B), HTM cell-conditioned medium (C), and aqueous humor (D). Blue: DAPI stained nuclei. Green: F-actin. Red: PECAM-1. Cyan: fibulin-2. Scale bar = 30 μm

5.3.4. Differentiation of HMVECs to HSC-like cells by co-culture with HTM on SU-8 scaffolds

Co-culture of distinct cell types in a combined culture, can provide a more physiological way of obtaining *in vivo*-like tissue morphology and function [283], allow for the study of the interaction and signaling between different cell types [284] and stimulate cell differentiation [285]. Interested in investigating whether contacts or interactions between HMVECs and HTM cells could induce differentiation of HMVECs into HSC-like cells, we attempted to co-culture these cells and monitored cell morphology via SEM on day 7 and day 14 of co-culture. After 7 days of HTM/HMVEC co-culture (Fig. 5.8 B and C) HMVECs appeared similar to mono-cultured cells (Fig. 8A). It was noted that co-cultured HMVEC cell layer was slightly thicker than mono-cultured controls. By day 14 of co-culture, striking differences were noted between HMVECs grown alone (Fig. 5.8D) and those co-cultured with HTM cells (Fig. 5.8 E and F). While mono-cultured HMVECs maintained polygonal morphology and thin cell layer appearance, HTM/HMVEC co-culture induced morphological changes on HMVECs which appeared elongated and the cell-layer was increasingly thicker.

Based on these results we established a HTM/HMVEC co-culture protocol which was used for the remaining of our studies (Fig. 5.9A). HTM cells were first cultured for 7 days on one side of the HA-coated SU8-scaffolds (from day -7 to day 0). On day 0 the scaffold is inverted and HMVECs were cultured on the opposite side to which HTM cells were cultured on. After allowing HMVEC cell attachment and initial growth, on day 7, constructs were again inverted to emulate the *in vivo* tissue architecture where HTM cells in the apical-to-basal direction, while HSCs are in the basal-to-apical direction.

The cross-section of the 3D HTM/HMVEC constructs distinctively showed cell layers on each side of the scaffold (Fig. 5.9B). To corroborate these results, the co-cultured constructs were stained with phalloidin. Through confocal Z-stacks we were able to visualize the side-view profile of the co-cultured samples demonstrating cell layers at both sides of the scaffolds (Fig. 5.9C). Cell processes that originated from each cell layer were observed running down the pores of the scaffolds in all of the samples. Some of these processes appeared to connect to each other, while others were shorter and did not reach the opposite cell layer.

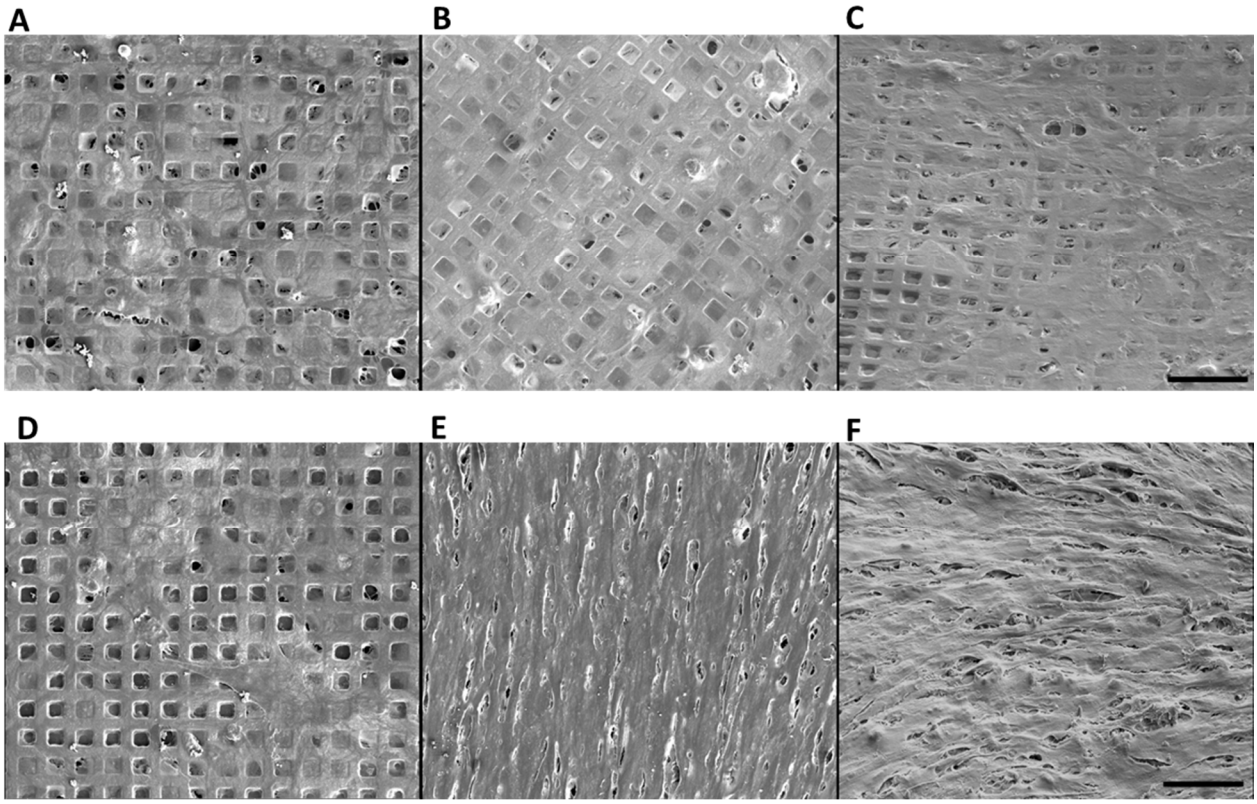

Figure 5.8. Scanning electron micrographs of HMVECs under co-culture with HTM for 7 and 14 days. (A-C) Day 7. (D-F) Day 14. (A and D) HMVEC alone as the control. (B and E) Top view and (C and F) tilted view of HMVECs co-cultured with HTM cells. Scale bar = 50 μm.

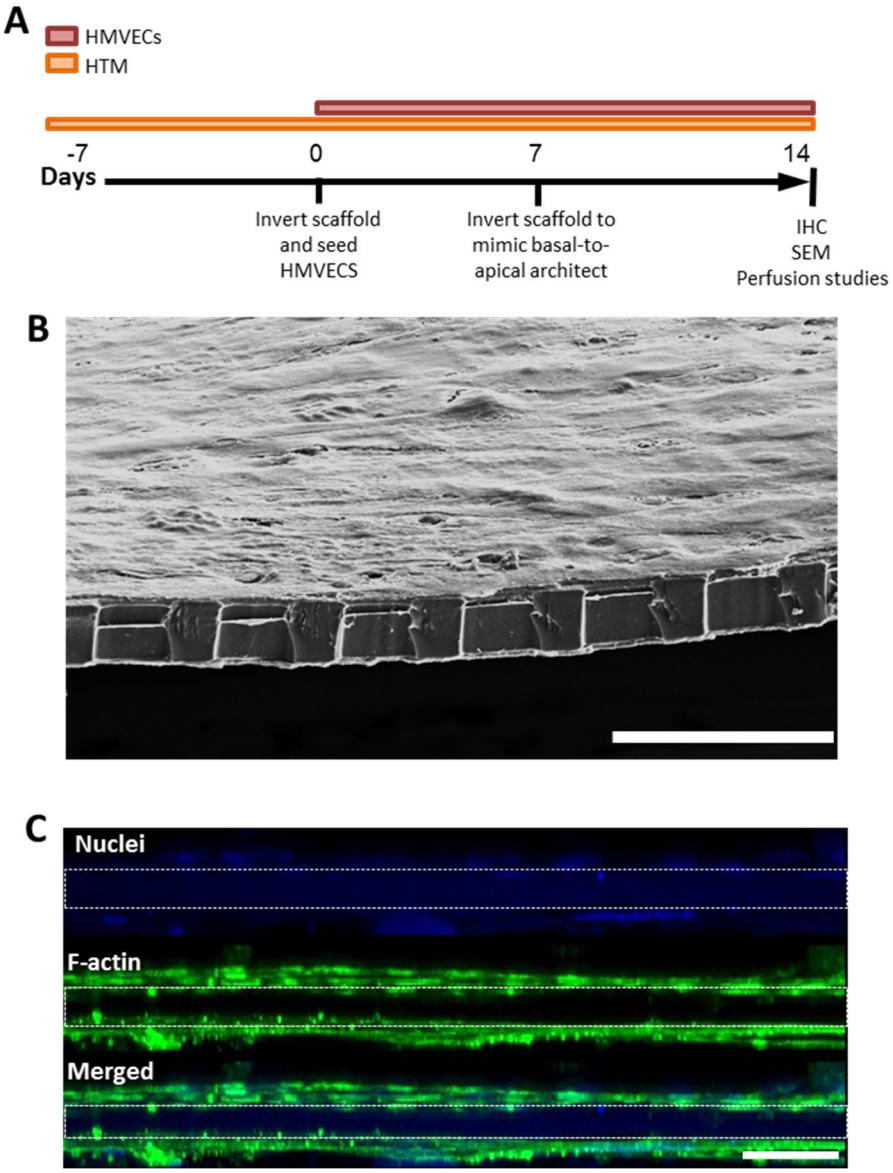

Figure 5.9. 3D Co-culture of HTM and HMVECs on HA-coated SU-8 scaffold demonstrated the feasibility of co-culturing these two cell types. (A) Schematic procedure used for HTM/HMVEC co-culture. (B) Scanning electron micrograph of co-cultured HTM/HMVECs on day 14. (C) Cross-sectional confocal imaging of phalloidin-stained F-actin cytoskeleton (green) of 3D co-culture HTM/HMVEC construct co-stained with DAPI (blue) to reveal total cell population.; demonstrating feasibility to co-culture these two cell types. Dotted lines indicate the location of the scaffold. Scale bar = 30 μm.

To confirm that the co-culture of HTM cells with HMVECs was not inducing detrimental differentiation of the HTM cells, expression of HTM markers such as myocilin and αB-crystallin were analyzed on the co-cultured constructs. Through

confocal imaging we visualized the expression of these two markers and by side-view rendering, we confirm the location of myocilin and αB-crystallin was limited to the HTM cell layer on the HTM/HMVEC constructs (Fig. 5.10). These data demonstrate the feasibility of co-culturing HMVECs and HTM cells, and suggests that interactions, perhaps cell-cell contact, can induce morphological changes of HMVECs from cobblestone-like to an elongated denser cell-shape.

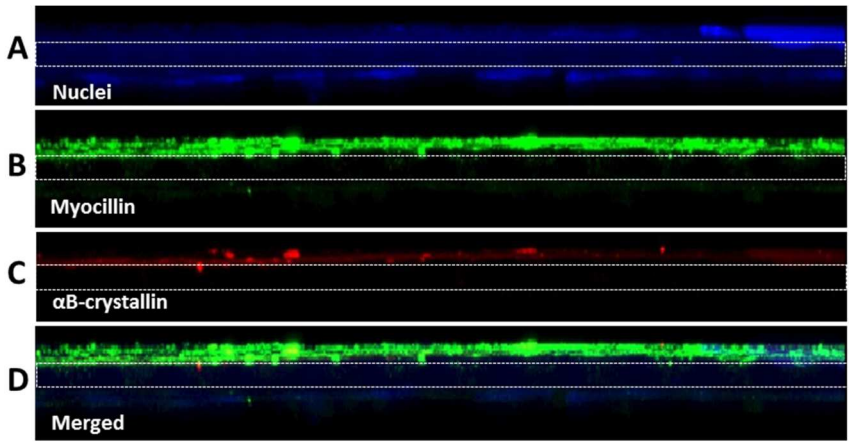

Figure 5.10. The 3D Co-culture HTM/HMVEC construct maintained HTM-marker expression revealed by cross-sectional confocal imaging. (A) DAPI-stained nuclei (blue). (B) Myocilin (green). (C) αB-crystallin (red). (D) Merged image. Dotted lines indicate the location of the scaffold. Scale bar = 30 μm.

5.3.5. Comparison of 3D co-culture of HTM/HMVEC with HTM/HSC

To investigate the feasibility of using the HTM/HMVEC construct as a platform to evaluate novel glaucoma therapeutics that target the conventional outflow tract, we further characterized HTM/HMVEC co-culture and directly compared it to its HTM/HSC co-culture counterpart. Therefore, we began by comparing, side-by-side the topography and cell morphology of these cells after 14 days of co-culture. HSC cells co-cultured with HTM cells grew to confluence, covering the SU-8 scaffold, and presented

elongated, spindle-like shape (Fig. 5.11A). Similarly, HMVECs co-cultured with HTM cells also covered the scaffold exhibited elongated shape (Fig. 5.11B). Vacuole and pore formation by HSC cells have recently gained a great deal of focus as potential key mechanism for regulation of outflow resistance [275]. Therefore, we attempted to induce vacuole/pore formation by perfusing the HSC and/or HMVEC cell layer in our co-cultured constructs in the basal-to-apical direction. SEM analysis demonstrated that both, HSC and HMVEC layers form vacuoles/pores after perfusion (Fig. 5.11 C and D). The vacuoles observed on the HSC layer had dimensions of 4.25 ± 1.05 μm, 4.51 ± 0.7 (length, width) (N=15, over 2 experiments) while HMVECs presented vacuoles of 6.25 ± 0.53 μm in length by 4.56 ± 1.1 μm in width (N=12 over 3 experiments). All vacuoles observed had small orifices at the surface which might be due to the electron beam that caused the opening to widen during imaging.

We next compared the expression of VE-cadherin, PECAM-1 and fibulin-2 between co-cultured HTM/HSC and HTM/HMVEC constructs. Side-view rendering of confocal z-stack images allowed us to visualize the expression of these markers. Both constructs expressed VE-cadherin, PECAM-1 and fibulin-2 at the HSC (Fig. 5.12A) and HMVEC (Fig. 5.12B) cell layer. PECAM-1 and fibulin-2 expression appeared to be slightly higher on the HTM/HMVEC samples, while VE-cadherin expression appeared to be intensified in HTM/HSC constructs. To determine whether these qualitative differences were significant and to confirm the presence of the HTM layer in the co-cultured samples, we performed qPCR analysis of gene expression of HTM-marker of αB-crystallin, HSC markers of PECAM-1 and fibulin-2 and house-keeping gene of GAPDH (Table 1) in HTM alone, HTM/HSC and HTM/HMVEC 3D constructs. The αB-

crystallin gene was expressed in all samples, corroborating the presence of the HTM layer in co-cultured constructs (Fig. 5.13). PECAM-1 and fibulin-2 genes were not expressed in 3D HTM constructs. On the contrary, as expected, HTM/HSC and HTM/HMVEC 3D constructs indeed expressed PECAM-1 and fibulin-2 genes (Fig. 5.13). No statistical significant differences were found in the levels of gene expression between HTM/HSC and HTM/HMVEC constructs.

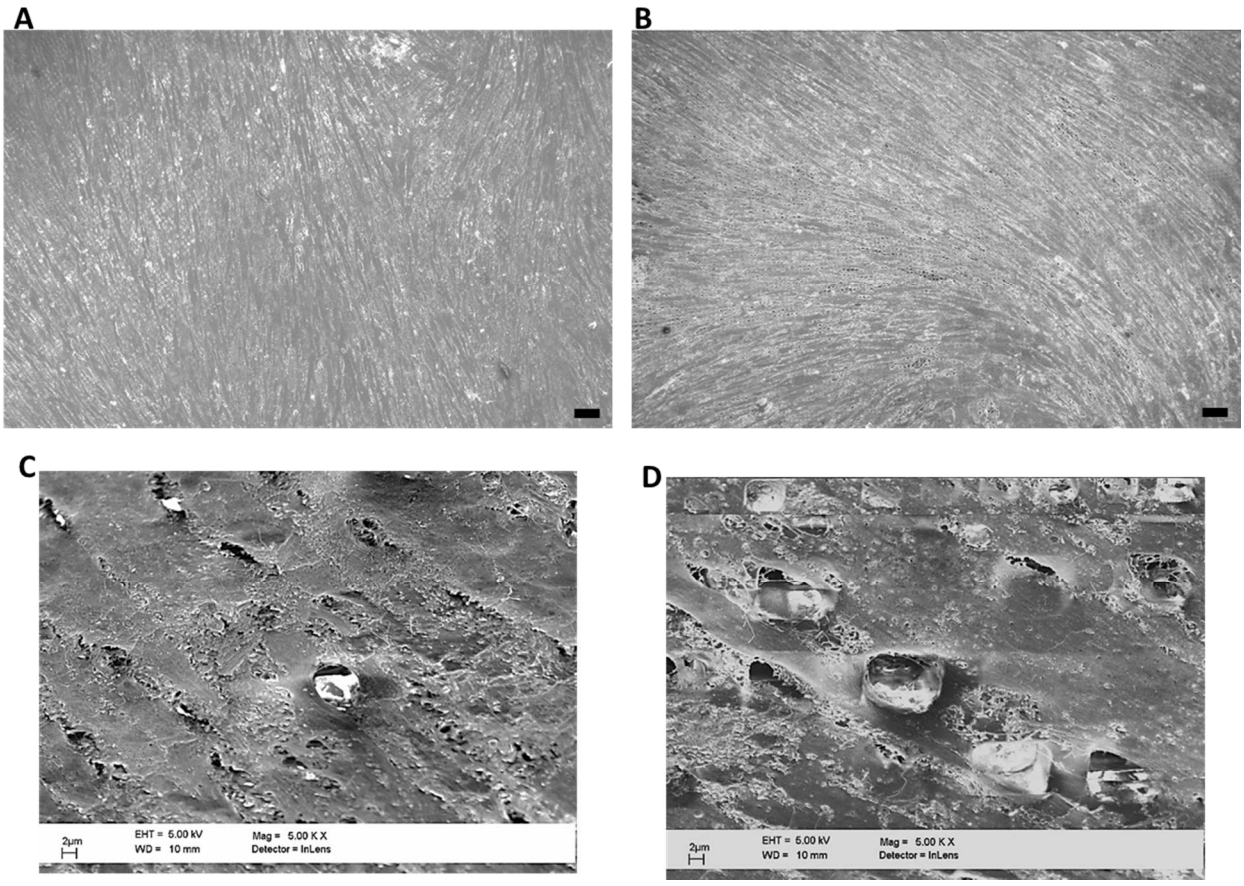

Figure 5.11. SEM of HSCs and HMVECs co-cultured with HTM cells for 14 days. (A) HSC and (B) HMVEC cell layer. Scale bar = 100 µm. Pore formation at (C) HSC and (D) HMVEC cells subjected to perfusion at 5 µl/min. Scale bar = 2µm.

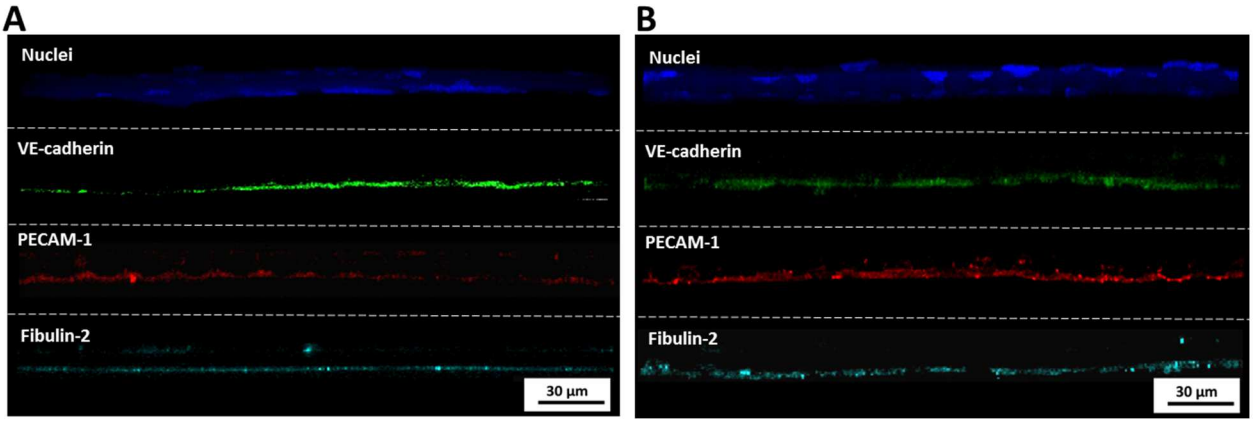

Figure 5.12. The 3D Co-culture HTM/HMVEC construct maintained HSC-marker expression revealed by cross-sectional confocal imaging. (A) HSC cells co-cultured with HTM cells grown on the HA-coated SU-8 scaffold for 14 days. (B) HMVECs co-cultured with HTM cells grown on the HA-coated SU-8 scaffold for 14 days. Blue: DAPI stained nuclei. Green: VE-cadherin. Red: PECAM-1. Cyan: fibulin-2. Scale bar = 30 µm.

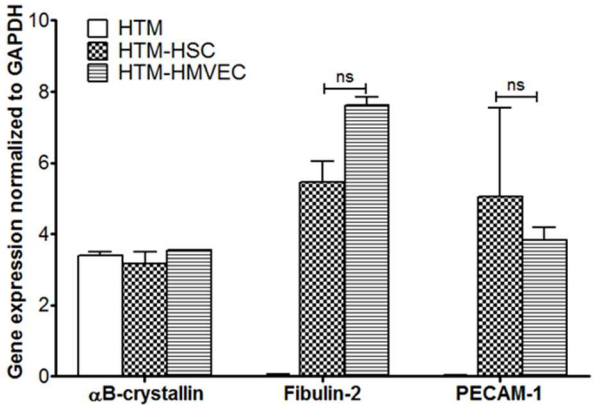

Figure 5.13. Gene expression of HTM and HSC markers in 3D co-cultured HTM/HMVEC constructs. qPCR analysis confirmed that 3D Co-culture HTM/HMVEC constructs maintained HTM- and HSC-marker expression in comparison to HTM alone and HTM/HSC co-culture for 14 days.

Additionally, expression of ECM proteins such as collagen IV, fibronectin and laminin were confirmed in the HTM/HMVEC co-cultured constructs (Fig. 5.14A). We further compared the gene expression of these ECM proteins in HTM/HSC and HTM/HMVEC samples. Our results showed that HTM/HMVEC constructs express less collagen IV (N=3, $P<0.001$) and fibronectin (N=3, $P<0.05$) than HTM/HSC co-cultures.

Altogether, these data suggests the HTM/HMVEC and HTM/HSC co-culture have striking phenotypical similarities, posing a novel tool to study the differentiation of blood endothelial cells to HSC-like and a higher-throughput platform to investigate novel intraocular pressure lowering agents/targets.

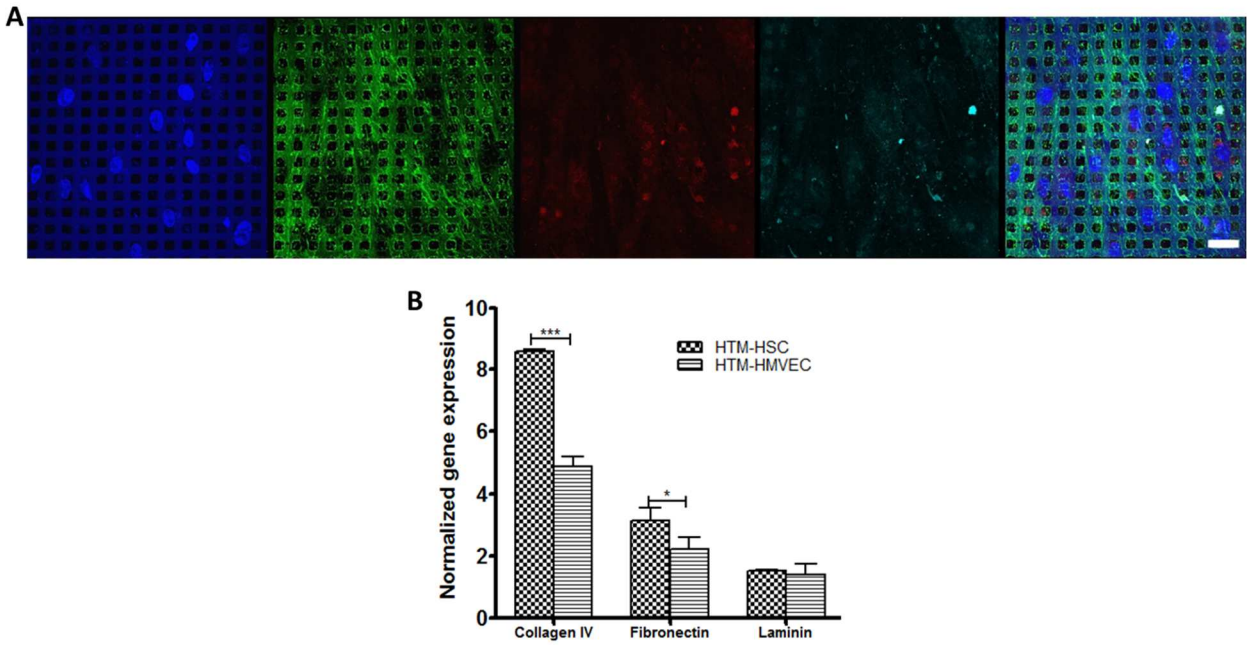

Figure 5.14. Immunocytochemistry and gene expression of ECM proteins found in the conventional outflow tract. (A) HTM/HMVEC coculture construct stained with collagen IV (green), fibronectin (red) and laminin (cyan). Scale bar = 30 μm. (B) qPCR analysis of ECM proteins in 3D co-cultured HTM/HSC and HTM/HMVEC constructs on day 14 (N=3).

5.4 Discussion

In this study, human microvascular endothelial cells, cultured on well-defined porous microstructures, are evaluated for their potential to be an alternative cell source to Schlemm's canal cells for high throughput *in vitro* studies, including drug screening. In addition we developed a co-culture model of the conventional outflow tract using HTM/HMVECs that resembles the recently developed HTM/HSC co-culture construct developed in our laboratory [286].

HMVECs have been shown to exhibit contact-inhibition growth, but when stimulated, these cells have the potential to form sprouts, proliferate, migrate and form new blood vessels [287], resembling aspects of HSC development. To our advantage, HMVECs have demonstrated i*n vitro* differentiation into branching tube-like structures in response to their media environment [288], making them suitable for differentiation purposes. HMVECs have an innate polygonal shape while HSCs are elongated and spindle-like. Despite their morphological differences, these two cell types express, with different expression patterns, similar protein such as VE-cadherin, CD-34, PECAM-1 and fibulin-2 [98, 99, 278, 289, 290]. Our initial attempt to differentiate HMVECs relied on biochemical cues or soluble factors to induce changes in these cells while maintaining vascular markers of interest. Interestingly, AH completely remodeled HMVEC cell morphology and induced a different expression pattern of HSC-protein markers compared to the other treatments. Aqueous humor outflow has been connected to the acquisition of lymphatic markers by HSC cells during development [51]. It has recently been shown that flow of AH regulates morphogenesis and lymphatic fate of HSC by increasing protein levels of PROX1 and vascular endothelial

growth factor receptor 3 (VEGFR3) [52]. In addition it has been suggested that Kruppel-like factor 4 (Klf4), a key shear stress responsive transcription factor, may be affected by AH flow and could be directly related to the observed increase of PROX1 expression [52]. The results in this work suggest that AH on its own, even without flow, could induce changes in the developing (vascular) HSC cells, which could prompt their adult elongated morphology.

Despite the HMVEC morphology change induced by AH, it greatly inhibited cell proliferation; therefore a co-culture technique, in an attempt to elicit morphological changes and proper cell proliferation was implemented. Given recent reported success in co-culturing HTM/HSC cells on porous microstructures, a similar method, optimized for this particular purpose was used for the HTM/HMVEC co-cultures. To our surprise, direct co-culture with HTM cells, stimulated drastic changes in HMVECs morphology and protein expression by day 14, resembling the HSC layer and fully covering the scaffold. These findings suggest that additional cell-cell contact between vascular and HTM cells may be involved in differentiation and fully development of the HSC. Mature HTM cells are known to secrete and express several factors and proteins that are believed to be involved in the conventional outflow tract homeostasis, which could perhaps also induce proper HSC development. Some of these factors/proteins include vascular endothelial growth factor (VEGF) [291] and matrix GLA (MGP) [292]. TM cells actively secrete endogenous VEGF, and on the other hand, HSC cells during development, while acquiring their lymphatic characteristics, express increased levels of VEGFR3. Vascular cells express receptor tyrosine kinases (RTK) including VEGFR, which is required for normal development and maintenance of the vascular bed; in

particular VEGFR3 is unique in that it is exclusively expressed in lymphatic endothelium [293]. Therefore, it is plausible to speculate that the VEGF secreted by TM cells could interact or prompt increase VEGFR3 expression in HMVECs, and enhance their differentiation into HSC-like cells. Furthermore, matrix GLA protein (MGP), a protein that is expressed by TM cells believed to play a protective role against calcification and aid cell differentiation, could also be involved in HMVEC phenotypical changes described after co-culture.

Also important to note is that the protein myocilin which is known to be expressed and secreted by TM [68, 294], and to a less extend by SC cells [295], was not expressed at detectable levels by HMVEC cell layer in co-culture. On the other hand, HTM/HSC construct expressed myocilin on both cell layers, raises questions on the role of myocilin in HSC cells. Additional side-by-side biological and functional studies between HTM/HMVEC and HTM/HSC models could help understand myocilin's function in the conventional outflow tract and its role in the inner wall of the HSC.

The microfabricated scaffolds on which HMVECs and HSCs were cultured during this work has allowed for the expression of several markers, which are otherwise loss when cultured on glass or 2D cultures. For example, loss of VE-cadherin and PECAM-1 expression in cultured cells has been previously reported [99, 278]. Furthermore, current *in vitro* models have tried to replicate and monitor HSCs vacuoles formation in response to flow, but unfortunately these systems induce overly large vacuoles than those reported *in vivo* [296]. This discrepancy is believed to be caused by the differences in pressure drop across the *in vitro* HSC cell layer and that occurring across the inner wall cells *in vivo,* this last one is expected to be greater given that the HTM

JCT layer adjacent to HSC cells could increase the pressure drop. To that end, the vacuole/pore formation that is reported here, using HTM/HSC and HTM/HMVEC co-culture constructs, are within the dimensions reported for *in vivo* primate HSC vacuoles [296], highlighting the importance of the HTM layer and need of more realistic *in vitro* model systems of the conventional outflow tract. The co-culture model described in this work could fill this need and allow for more realistic studies of the conventional outflow tract. Likewise, the culture protocol developed during this work rescued these markers in HSC cells which could help further studies related to this cell type. Overall, the co-culture platform presented here could have great implications in the better understanding of various biological phenomenon that take place in the conventional outflow tract including HSC development/lymphatic transition, HTM-HSC and HTM-HMVEC cell-cell that can induce several functional events, and may also be used as a higher-throughput platform that can help find novel targets and treatments for glaucoma.

SUMMARY

I. Conclusions

The TM plays a crucial role in AH outflow and hence IOP-regulation in the eye. The microenvironment within the TM and SC are important for normal AH flow and the development of a pressure gradient that facilitates outflow. Engineering an *in vitro* model of the trabecular outflow tract, that resemble the AH flow dynamics, would allow improved studies of the biology and pathophysiology of glaucomatous HTM, empowering the discovery of mechanisms that will reverse elevation of IOP. Such model would provide a new venue for effective screening of combinatorial libraries of potential therapeutic agents and glaucoma treatments. The TM is a dynamic 3D tissue that is composed of TM cells surrounded by their ECM and adjacent to a discontinuous basement membrane on which SC inner wall endothelial cell monolayer laid. The ECM proteins that surround the TM cells and form SC basement membrane are modulated by several biological factors which help control pressure across the outflow tract. In addition, cell-ECM interactions also induce cytoskeletal rearrangements that can also be responsible to modulate the TM dynamics. The complex mechanics and biology involved in the TM has presented an obstacle for research scientist and pharmaceutical industry who are attempting to better understand this tissue to develop efficient glaucoma-medications.

In this dissertation, we have demonstrated (1) the construction and validation of an *in vitro* HTM model that can be used for investigation of outflow

physiology and responsiveness to biological agents using micropatterned, well-defined, porous SU-8 scaffolds, (2) the capability of establishing a bioengineered *in vitro* steroid-induced glaucomatous HTM model, (3) the regulation of ECM accumulation that can induce pressure elevation by a steroid or TGFβ-2 induction in the absence or presence of the ROCK inhibitor Y-27632, (4) the feasibility of engineering a HTM/HMVEC co-culture construct to mimic the conventional outflow tract by phenotypical differentiation of HMVEC induced by co-culture with pre-cultivated HTM on scaffolds. The bioengineered HTM exhibited several *in vivo* and *ex vivo*-like characteristics, including expression of HTM-markers, ECM architecture surrounding the HTM cells, and in particular, responsiveness to IOP-modulating agents; latruncunlin-B, steroid, TGFβ-2 and ROCK inhibitor. As shown in Fig. 6.1, the outflow facility per unit area of the bioengineered 3D HTM increased in response to latruncunlin-B and ROCK inhibitor while steroid and TGFβ-2 decreased outflow facility, which is in a similar fashion to those being seen *ex vivo*. This work lays a solid foundation for future high-throughput screening tool for glaucoma medications that target the trabecular meshwork and provides the ophthalmic field with a new tool to explore the conventional outflow tract biology.

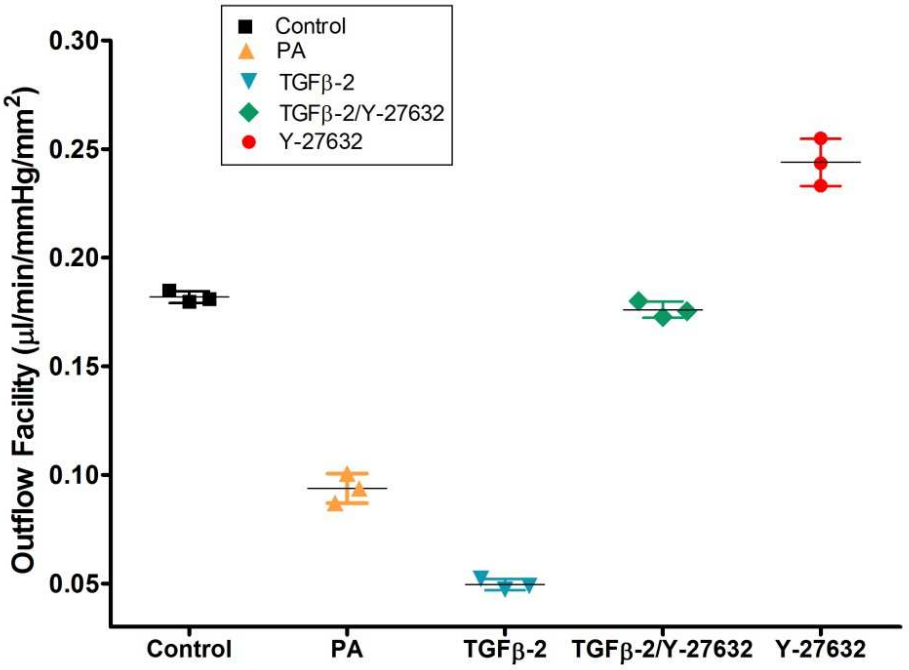

Figure 6.1. Outflow facility modulation of 3D bioengineered HTM in response to pharmacological agents

II. Future Directions

In the future, it is essential to: scale-up the perfusion system to be able to perform a high-throughput screening of IOP-modulating drugs using the bioengineered HTM, study the pathway(s) affected by the induction of myocillin by ROCK inhibitor, perform perfusion studies on HTM/HMVEC construct, and it is imperative to further explore biology behind the phenotypical changes of HMVEC after HTM co-culture

II.I. Construction of multi-chamber array perfusion system that incorporates the Bioengineered trabecular Outflow-Tract for simultaneous drug screening

A multi-chamber array that can serve as perfusion units for bioengineered HTMs can be fabricated using 3-D printing and micro-CNC machinery (Fig. 6.2 A and B). Such array would require to be incorporated to a perfusion system that allows independent pressure and flow control (Fig. 6.2C). Given the particular sensitivity required to capture small pressure changes that agents could cause across the tissue, a sensor capable of detecting 0.1 mmHg would be ideal. Additionally, flow rate control can be refined from our current system by utilizing pressure driven flow, although it is important to also keep in mind the dimensions of tubing and chambers to be utilized since they would have an effect on the flow dynamics.

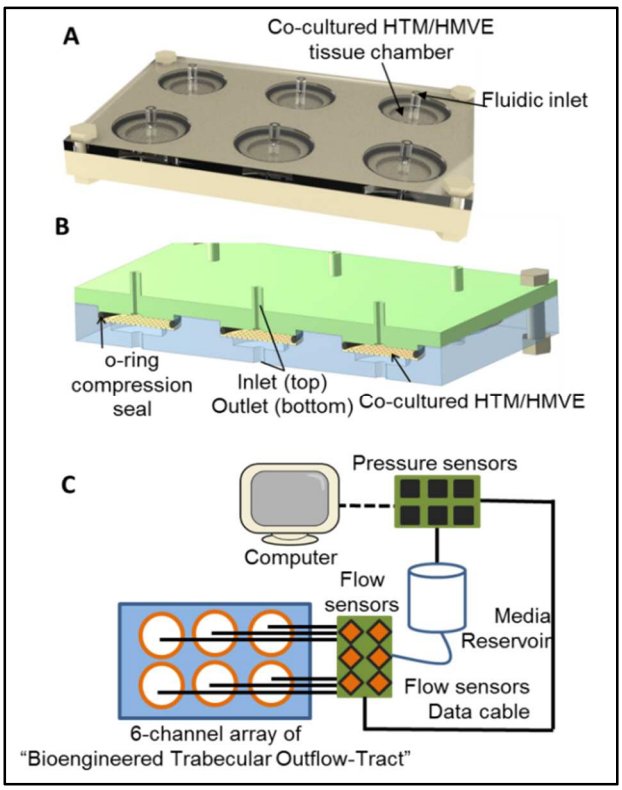

Figure 6.2. Schematic of 6-chamber array perfusion system. (A)Top view and (B) Cross-sectional view of plate. (C) Proposed integrated system for high- throughput drug screening.

II.II. Myocilin induction by ROCK inhibitor

Trabecular meshwork cells secrete myocilin into the aqueous humor, where it is believed to may play a role in extracellular matrix-mediated cell adhesion and cell motility. Our studies have shown an increase in myocilin gene and protein expression after ROCK inhibitor treatment. Compared to myocilin gene expression induction by steroids(<100-fold up-regulation), ROCK inhibitor induced myocillin to a much lower degree (~6-fold gene up-regulation) but when compared protein-level expression, ROCK inhibitor treatment induced significantly more myocilin protein expression than during steroid treatment($P<0.001$) (CHAPTER 3). These data suggests potential translational-dependent induction of myocilin by ROCK inhibitor.

Given the growing interest in ROCK inhibitors as new class of glaucoma drugs, it is of high importance to further study the implication of these agents in myocilin elevation, since it could elicit additional side effects that could hinder the IOP lowering effect of these drugs in patients. A study that could perhaps be done in this topic could involve the silencing or overexpression of genes related within the ROCK-pathway in order to analyzing their effect, if any, in myocilin expression. Such analysis could give use insight into whether the increase of myocilin after ROCK inhibitor is independent of the ROCK-pathway.

II.III. Physiological drug response of the 3D HTM/HMVEC construct

To corroborate the proper physiological behavior of our bioengineered 3D HTM/HMVEC construct, drug responsiveness through perfusion studies must be evaluated. Such studies would not only provide insight into functional flow regulation, but would also allow calculation of outflow facility of our 3D co-culture construct. The outflow facility of the bioengineered HTM describe in most of this dissertation was slightly higher than that of *in vivo* outflow facility, it is possible that the added complexity of the HMVEC monolayer to this model could lower the outflow facility to levels comparable to *in vivo*.

II.IV. Investigate the differentiation of HMVEC into HSC-like cells

In CHAPTER 5 phenotypical changes of HMVEC cells were described, such transformation requires further investigation. In the last few years several advances in understanding the development of the SC have demonstrated that this tissue originates from blood vessels and during the postnatal period, acquires lymphatic

markers including Prox-1 and FOXC2 [52]. Adult SC expresses vascular marker including Tie2, Kdr (Vegfr2), EfnB2, PECAM-1, CD-34 and VE-cadherin, while also expressing the lymphatic markers it acquired postnatal. Analysis of lymphatic and vascular markers expression during different time periods of the HTM/HMVEC co-culture could hold the answer to the HMVEC transformation. Additionally, AH flow has been correlated to the morphogenesis and lymphatic fate of the SC. Park et.al have shown that the incremental increase of AH outflow that takes place postnatal, enhances SC differentiation, increasing the expression of Prox-1 and VEGFR3. In a same manner, it is plausible that the HMVEC morphological/phenotypical transformation we described during HTM co-culture may be speed up if the construct is supplemented with AH.

Furthermore, analysis of the mechanistic events that lead to morphological changes during HTM/HMVEC co-culture could provide additional detail into possible HTM cell- HSC cell interactions that could further assist the postnatal SC differentiation. Pathways that are suggested for further investigation in this co-culture construct include VEGF, myocilin, αB-crystallin and actin.

References

1. Vaajanen, A., H. Vapaatalo, and O. Oksala, *A modified in vitro method for aqueous humor outflow studies in enucleated porcine eyes.* Journal of ocular pharmacology and therapeutics : the official journal of the Association for Ocular Pharmacology and Therapeutics, 2007. **23**(2): p. 124-31.
2. Sens, C., et al., *Synthesis, structure, and acid-base and redox properties of a family of new Ru(II) isomeric complexes containing the trpy and the dinucleating Hbpp ligands.* Inorganic chemistry, 2003. **42**(25): p. 8385-94.
3. Anda, C., et al., *Systematic evaluation of molecular recognition phenomena. 3. Selective diphosphate binding to isomeric hexaazamacrocyclic ligands containing xylylic spacers.* Inorganic chemistry, 2003. **42**(25): p. 8545-50.
4. Russell, P., et al., *Response of human trabecular meshwork cells to topographic cues on the nanoscale level.* Investigative ophthalmology & visual science, 2008. **49**(2): p. 629-35.
5. Fautsch, M.P., et al., *Primary trabecular meshwork cells incubated in human aqueous humor differ from cells incubated in serum supplements.* Investigative ophthalmology & visual science, 2005. **46**(8): p. 2848-56.
6. Schlunck, G., et al., *Substrate rigidity modulates cell matrix interactions and protein expression in human trabecular meshwork cells.* Investigative ophthalmology & visual science, 2008. **49**(1): p. 262-9.
7. Koga, T., et al., *Rho-associated protein kinase inhibitor, Y-27632, induces alterations in adhesion, contraction and motility in cultured human trabecular meshwork cells.* Experimental eye research, 2006. **82**(3): p. 362-70.
8. Peterson, J.A., et al., *Effect of latrunculin-B on outflow facility in monkeys.* Experimental eye research, 2000. **70**(3): p. 307-13.
9. Ethier, C.R., A.T. Read, and D.W. Chan, *Effects of latrunculin-B on outflow facility and trabecular meshwork structure in human eyes.* Investigative ophthalmology & visual science, 2006. **47**(5): p. 1991-8.
10. Bahler, C.K., et al., *Prostaglandins increase trabecular meshwork outflow facility in cultured human anterior segments.* American journal of ophthalmology, 2008. **145**(1): p. 114-9.
11. Bahler, C.K., et al., *Trabecular bypass stents decrease intraocular pressure in cultured human anterior segments.* American journal of ophthalmology, 2004. **138**(6): p. 988-94.
12. Gasiorowski, J.Z. and P. Russell, *Biological properties of trabecular meshwork cells.* Experimental eye research, 2009. **88**(4): p. 671-5.
13. Johnson, D.H., *Trabecular meshwork and uveoscleral outflow models.* Journal of glaucoma, 2005. **14**(4): p. 308-10.
14. Tamm, E.R., *The trabecular meshwork outflow pathways: structural and functional aspects.* Experimental eye research, 2009. **88**(4): p. 648-55.
15. Tektas, O.Y. and E. Lutjen-Drecoll, *Structural changes of the trabecular meshwork in different kinds of glaucoma.* Experimental eye research, 2009. **88**(4): p. 769-75.
16. Overby, D.R., W.D. Stamer, and M. Johnson, *The changing paradigm of outflow resistance generation: towards synergistic models of the JCT and inner wall endothelium.* Experimental eye research, 2009. **88**(4): p. 656-70.
17. Johnson, M., *'What controls aqueous humour outflow resistance?'.* Experimental eye research, 2006. **82**(4): p. 545-57.
18. Keller, K.E., et al., *Extracellular matrix turnover and outflow resistance.* Experimental eye research, 2009. **88**(4): p. 676-82.

19. Last, J.A., et al., *Elastic modulus determination of normal and glaucomatous human trabecular meshwork.* Investigative ophthalmology & visual science, 2011. **52**(5): p. 2147-52.
20. McLaren, J.W., *Measurement of aqueous humor flow.* Experimental eye research, 2009. **88**(4): p. 641-7.
21. Heijl, A., et al., *Reduction of intraocular pressure and glaucoma progression: results from the Early Manifest Glaucoma Trial.* Archives of ophthalmology, 2002. **120**(10): p. 1268-79.
22. Abu-Hassan, D.W., T.S. Acott, and M.J. Kelley, *The Trabecular Meshwork: A Basic Review of Form and Function.* Journal of ocular biology, 2014. **2**(1).
23. Kwon, Y.H., et al., *Primary open-angle glaucoma.* The New England journal of medicine, 2009. **360**(11): p. 1113-24.
24. Alward, W.L., *Biomedicine. A new angle on ocular development.* Science, 2003. **299**(5612): p. 1527-8.
25. Quigley, H.A., *Open-angle glaucoma.* The New England journal of medicine, 1993. **328**(15): p. 1097-106.
26. Quigley, H.A. and A.T. Broman, *The number of people with glaucoma worldwide in 2010 and 2020.* The British journal of ophthalmology, 2006. **90**(3): p. 262-7.
27. Quigley, H.A., *Number of people with glaucoma worldwide.* The British journal of ophthalmology, 1996. **80**(5): p. 389-93.
28. Quigley, H.A. and S. Vitale, *Models of open-angle glaucoma prevalence and incidence in the United States.* Investigative ophthalmology & visual science, 1997. **38**(1): p. 83-91.
29. Thylefors, B. and A.D. Negrel, *The global impact of glaucoma.* Bulletin of the World Health Organization, 1994. **72**(3): p. 323-6.
30. Quigley, H.A., *Glaucoma.* Lancet, 2011. **377**(9774): p. 1367-77.
31. Burr, J.M., et al., *The clinical effectiveness and cost-effectiveness of screening for open angle glaucoma: a systematic review and economic evaluation.* Health technology assessment, 2007. **11**(41): p. iii-iv, ix-x, 1-190.
32. Traverso, C.E., et al., *Direct costs of glaucoma and severity of the disease: a multinational long term study of resource utilisation in Europe.* The British journal of ophthalmology, 2005. **89**(10): p. 1245-9.
33. Lewis, T.L. and C.L. Chronister, *Etiology and pathophysiology of primary open-angle glaucoma*. Primary care of the glaucomas, 2nd Edition, ed. T.L. Lewis and M. Fingeret2001, New York: McGraw.
34. Shaarawy, T.M., et al., *Glaucoma: Medical Diagnosis and Therapy*. Vol. 1. 2009, Philadelphia: Elsevier, Ltd.
35. Bahrami, H., *Causal inference in primary open angle glaucoma: specific discussion on intraocular pressure.* Ophthalmic epidemiology, 2006. **13**(4): p. 283-9.
36. Kass, M.A., et al., *The Ocular Hypertension Treatment Study: a randomized trial determines that topical ocular hypotensive medication delays or prevents the onset of primary open-angle glaucoma.* Archives of ophthalmology, 2002. **120**(6): p. 701-13; discussion 829-30.
37. Heijl, A., et al., *Intraocular pressure reduction with a fixed treatment protocol in the Early Manifest Glaucoma Trial.* Acta ophthalmologica, 2011. **89**(8): p. 749-54.
38. Gould, D.B., R.S. Smith, and S.W. John, *Anterior segment development relevant to glaucoma.* The International journal of developmental biology, 2004. **48**(8-9): p. 1015-29.
39. Sowden, J.C., *Molecular and developmental mechanisms of anterior segment dysgenesis.* Eye, 2007. **21**(10): p. 1310-8.
40. Smith, R.S., et al., *The mouse anterior chamber angle and trabecular meshwork develop without cell death.* BMC developmental biology, 2001. **1**: p. 3.

41. Johnston, M.C., et al., *Origins of avian ocular and periocular tissues.* Experimental eye research, 1979. **29**(1): p. 27-43.
42. Trainor, P.A. and P.P. Tam, *Cranial paraxial mesoderm and neural crest cells of the mouse embryo: co-distribution in the craniofacial mesenchyme but distinct segregation in branchial arches.* Development, 1995. **121**(8): p. 2569-82.
43. Reme, C. and S.L. d'Epinay, *Periods of development of the normal human chamber angle.* Documenta ophthalmologica. Advances in ophthalmology, 1981. **51**(3): p. 241-68.
44. Cvekl, A. and E.R. Tamm, *Anterior eye development and ocular mesenchyme: new insights from mouse models and human diseases.* BioEssays : news and reviews in molecular, cellular and developmental biology, 2004. **26**(4): p. 374-86.
45. Wulle, K.G., *Electron microscopic observations of the development of Schlemm's canal in the human eye.* Transactions - American Academy of Ophthalmology and Otolaryngology. American Academy of Ophthalmology and Otolaryngology, 1968. **72**(5): p. 765-73.
46. Wulle, K.G., *Electron microscopy of the fetal development of the corneal endothelium and Descemet's membrane of the human eye.* Investigative ophthalmology, 1972. **11**(11): p. 897-904.
47. Mao, M., et al., *Anterior segment dysgenesis and early-onset glaucoma in nee mice with mutation of Sh3pxd2b.* Investigative ophthalmology & visual science, 2011. **52**(5): p. 2679-88.
48. Baulmann, D.C., et al., *Pax6 heterozygous eyes show defects in chamber angle differentiation that are associated with a wide spectrum of other anterior eye segment abnormalities.* Mechanisms of development, 2002. **118**(1-2): p. 3-17.
49. Ding, Q.J., et al., *Induction of trabecular meshwork cells from induced pluripotent stem cells.* Investigative ophthalmology & visual science, 2014. **55**(11): p. 7065-72.
50. Du, Y., et al., *Multipotent stem cells from trabecular meshwork become phagocytic TM cells.* Investigative ophthalmology & visual science, 2012. **53**(3): p. 1566-75.
51. Kizhatil, K., et al., *Schlemm's canal is a unique vessel with a combination of blood vascular and lymphatic phenotypes that forms by a novel developmental process.* PLoS biology, 2014. **12**(7): p. e1001912.
52. Park, D.Y., et al., *Lymphatic regulator PROX1 determines Schlemm's canal integrity and identity.* The Journal of clinical investigation, 2014. **124**(9): p. 3960-74.
53. VanderWyst, S.S., et al., *Structural basement membrane components and corresponding integrins in Schlemm's canal endothelia.* Molecular vision, 2011. **17**: p. 199-209.
54. Goel, M., et al., *Aqueous humor dynamics: a review.* The open ophthalmology journal, 2010. **4**: p. 52-9.
55. Lutjen-Drecoll, E., *Functional morphology of the trabecular meshwork in primate eyes.* Progress in Retinal and Eye Research, 1999. **18**(1): p. 91-119.
56. Lutjen-Drecoll, E., R. Futa, and J.W. Rohen, *Ultrahistochemical studies on tangential sections of the trabecular meshwork in normal and glaucomatous eyes.* Investigative ophthalmology & visual science, 1981. **21**(4): p. 563-73.
57. Lutjen-Drecoll, E., *Anatomy of aqueous humor formation and drainage*, in *Duane's Foundations of Clinical Ophthalmolgy*, S.M. Podos and M. Yanoff, Editors. 2001, J..B. Lippincott: Philadelphia. p. 1-30.
58. Tan, J.C., et al., *In situ autofluorescence visualization of human trabecular meshwork structure.* Investigative ophthalmology & visual science, 2012. **53**(4): p. 2080-8.
59. Grant, W.M., *Experimental aqueous perfusion in enucleated human eyes.* Archives of ophthalmology, 1963. **69**: p. 783-801.
60. Bill, A., *Blood circulation and fluid dynamics in the eye.* Physiological reviews, 1975. **55**(3): p. 383-417.

61. Buller, C., D.H. Johnson, and R.C. Tschumper, *Human trabecular meshwork phagocytosis. Observations in an organ culture system.* Investigative ophthalmology & visual science, 1990. **31**(10): p. 2156-63.
62. Johnson, M. and K. Erickson, *Mechanisms and routes of aqueous humor drainage*, in *Principles and Practice of Ophthalmology*, D.M. Albert and F.A. Jacobiec, Editors. 2000, W.B. Saunders Co.: Philadelphia. p. 2577-2595.
63. Acott, T.S. and M.J. Kelley, *Extracellular matrix in the trabecular meshwork.* Experimental eye research, 2008. **86**(4): p. 543-61.
64. Lutjen-Drecoll, E., *Functional morphology of the trabecular meshwork.* Progress in Retinal and Eye Research, 1999(18): p. 91-119.
65. Fuchshofer, R., et al., *Biochemical and morphological analysis of basement membrane component expression in corneoscleral and cribriform human trabecular meshwork cells.* Investigative ophthalmology & visual science, 2006. **47**(3): p. 794-801.
66. Lutjen-Drecoll, E., *Morphological changes in glaucomatous eyes and the role of TGFbeta2 for the pathogenesis of the disease.* Experimental eye research, 2005. **81**(1): p. 1-4.
67. Lutjen-Drecoll, E., *Morphology of aqueous outflow pathway viewed by quick freeze deep etch*, in *The Glaucoma*, R. Ritch, M.B. Shields, and T. Krupin, Editors. 1996, Mosby-Year Book Inc.: St. Louis. p. 89-124.
68. Ueda, J., K. Wentz-Hunter, and B.Y. Yue, *Distribution of myocilin and extracellular matrix components in the juxtacanalicular tissue of human eyes.* Investigative ophthalmology & visual science, 2002. **43**(4): p. 1068-76.
69. Tawara, A., H.H. Varner, and J.G. Hollyfield, *Distribution and characterization of sulfated proteoglycans in the human trabecular tissue.* Investigative ophthalmology & visual science, 1989. **30**(10): p. 2215-31.
70. Gong, H., T.F. Freddo, and M. Johnson, *Age-related changes of sulfated proteoglycans in the normal human trabecular meshwork.* Experimental eye research, 1992. **55**(5): p. 691-709.
71. Kielty, C.M., M.J. Sherratt, and C.A. Shuttleworth, *Elastic fibres.* Journal of cell science, 2002. **115**(Pt 14): p. 2817-28.
72. Grierson, I. and W.R. Lee, *Junctions between the cells of the trabecular meshwork.* Albrecht von Graefes Archiv fur klinische und experimentelle Ophthalmologie. Albrecht von Graefe's archive for clinical and experimental ophthalmology, 1974. **192**(2): p. 89-104.
73. Grierson, I. and W.R. Lee, *The fine structure of the trabecular meshwork at graded levels of intraocular pressure. (1) Pressure effects within the near-physiological range (8-30 mmHg).* Experimental eye research, 1975. **20**(6): p. 505-21.
74. Grierson, I., et al., *Associations between the cells of the walls of Schlemm's canal.* Albrecht von Graefes Archiv fur klinische und experimentelle Ophthalmologie. Albrecht von Graefe's archive for clinical and experimental ophthalmology, 1978. **208**(1-3): p. 33-47.
75. Grierson, I., et al., *The trabecular wall of Schlemm's canal: a study of the effects of pilocarpine by scanning electron microscopy.* The British journal of ophthalmology, 1979. **63**(1): p. 9-16.
76. Siegner, A., et al., *alpha B-crystallin in the primate ciliary muscle and trabecular meshwork.* European journal of cell biology, 1996. **71**(2): p. 165-9.
77. Morrison JC., A.T., *Anatomy and physiology of aqueous humor outflow*, in *Glaucoma: Science and Practice*2003, Thieme Medical Publishers Inc: New York. p. 34-41.
78. Lutjen-Drecoll, E. and J.W. Rohen, *Morphology of aqueous outflow pathways in normal and glaucomatous eyes*, in *The Glaucomas*, R. Ritch, M.B. Shields, and T. Krupin, Editors. 1996, Mosby-Year Book Inc: St. Louis. p. 89-124.
79. Bill, A. and K. Hellsing, *Production and drainage of aqueous humor in the cynomolgus monkey (Macaca irus).* Investigative ophthalmology, 1965. **4**(5): p. 920-6.

80. Gabelt, B.T. and P.L. Kaufman, *Aqueous humor hydrodymanics*, in *Adler's Physiology of the Eye*, W.M. Hart, Editor 2003, Mosby: St. Louis, MO.
81. Mark, H.H., *Aqueous humor dynamics in historical perspective.* Survey of ophthalmology, 2010. **55**(1): p. 89-100.
82. Brubaker, R.F., *Measurement of uveoscleral outflow in humans.* Journal of glaucoma, 2001. **10**(5 Suppl 1): p. S45-8.
83. Ethier, C.R., et al., *Calculations of flow resistance in the juxtacanalicular meshwork.* Investigative ophthalmology & visual science, 1986. **27**(12): p. 1741-50.
84. Ethier, C.R., A.T. Read, and D. Chan, *Biomechanics of Schlemm's canal endothelial cells: influence on F-actin architecture.* Biophysical journal, 2004. **87**(4): p. 2828-37.
85. Vittal, V., et al., *Changes in gene expression by trabecular meshwork cells in response to mechanical stretching.* Investigative ophthalmology & visual science, 2005. **46**(8): p. 2857-68.
86. Bradley, J.M., et al., *Effect of matrix metalloproteinases activity on outflow in perfused human organ culture.* Investigative ophthalmology & visual science, 1998. **39**(13): p. 2649-58.
87. Keller, K.E., J.M. Bradley, and T.S. Acott, *Differential effects of ADAMTS-1, -4, and -5 in the trabecular meshwork.* Investigative ophthalmology & visual science, 2009. **50**(12): p. 5769-77.
88. Keller, K.E., et al., *Segmental versican expression in the trabecular meshwork and involvement in outflow facility.* Investigative ophthalmology & visual science, 2011. **52**(8): p. 5049-57.
89. Keller, K.E., M.J. Kelley, and T.S. Acott, *Extracellular matrix gene alternative splicing by trabecular meshwork cells in response to mechanical stretching.* Investigative ophthalmology & visual science, 2007. **48**(3): p. 1164-72.
90. Johnstone, M.A. and W.G. Grant, *Pressure-dependent changes in structures of the aqueous outflow system of human and monkey eyes.* American journal of ophthalmology, 1973. **75**(3): p. 365-83.
91. Grierson, I. and W.R. Lee, *Pressure effects on flow channels in the lining endothelium of Schlemm's canal. A quantitative study by transmission electron microscopy.* Acta ophthalmologica, 1978. **56**(6): p. 935-52.
92. Brubaker, R.F., *Determination of episcleral venous pressure in the eye. A comparison of three methods.* Archives of ophthalmology, 1967. **77**(1): p. 110-4.
93. Polansky, J.R., et al., *Human trabecular cells. I. Establishment in tissue culture and growth characteristics.* Investigative ophthalmology & visual science, 1979. **18**(10): p. 1043-9.
94. Stamer, W.D., et al., *Isolation and culture of human trabecular meshwork cells by extracellular matrix digestion.* Current eye research, 1995. **14**(7): p. 611-7.
95. Pang, I.H., et al., *Preliminary characterization of a transformed cell strain derived from human trabecular meshwork.* Current eye research, 1994. **13**(1): p. 51-63.
96. Steely, H.T., et al., *The effects of dexamethasone on fibronectin expression in cultured human trabecular meshwork cells.* Investigative ophthalmology & visual science, 1992. **33**(7): p. 2242-50.
97. Alvarado, J.A., et al., *Endothelia of Schlemm's canal and trabecular meshwork: distinct molecular, functional, and anatomic features.* American journal of physiology. Cell physiology, 2004. **286**(3): p. C621-34.
98. Stamer, W.D., et al., *Isolation, culture, and characterization of endothelial cells from Schlemm's canal.* Investigative ophthalmology & visual science, 1998. **39**(10): p. 1804-12.
99. Perkumas, K.M. and W.D. Stamer, *Protein markers and differentiation in culture for Schlemm's canal endothelial cells.* Experimental eye research, 2012. **96**(1): p. 82-7.
100. Overby, D.R., et al., *Altered mechanobiology of Schlemm's canal endothelial cells in glaucoma.* Proceedings of the National Academy of Sciences of the United States of America, 2014. **111**(38): p. 13876-81.

101. S., B., M. Krebs, and P. M.B., *3D Natural Biopolymer Scaffold for In Vitro Modeling of the Trabecular Meshwork*, in *ARVO*2015: Denver, CO.
102. Millard, L.H., D.F. Woodward, and W.D. Stamer, *The role of the prostaglandin EP4 receptor in the regulation of human outflow facility.* Investigative ophthalmology & visual science, 2011. **52**(6): p. 3506-13.
103. Shearer, T.W. and C.E. Crosson, *Adenosine A1 receptor modulation of MMP-2 secretion by trabecular meshwork cells.* Investigative ophthalmology & visual science, 2002. **43**(9): p. 3016-20.
104. Sumida, G.M. and W.D. Stamer, *Sphingosine-1-phosphate enhancement of cortical actomyosin organization in cultured human Schlemm's canal endothelial cell monolayers.* Investigative ophthalmology & visual science, 2010. **51**(12): p. 6633-8.
105. Tripathi, R.C., et al., *Trabecular cells express receptors that bind TGF-beta 1 and TGF-beta 2: a qualitative and quantitative characterization.* Investigative ophthalmology & visual science, 1993. **34**(1): p. 260-3.
106. Wax, M.B., et al., *Characterization of beta-adrenergic receptors in cultured human trabecular cells and in human trabecular meshwork.* Investigative ophthalmology & visual science, 1989. **30**(1): p. 51-7.
107. Keller, K.E. and T.S. Acott, *The Juxtacanalicular Region of Ocular Trabecular Meshwork: A Tissue with a Unique Extracellular Matrix and Specialized Function.* Journal of ocular biology, 2013. **1**(1): p. 3.
108. Acott, T.S., et al., *Trabecular repopulation by anterior trabecular meshwork cells after laser trabeculoplasty.* American journal of ophthalmology, 1989. **107**(1): p. 1-6.
109. Hosseini, M., et al., *IL-1 and TNF induction of matrix metalloproteinase-3 by c-Jun N-terminal kinase in trabecular meshwork.* Investigative ophthalmology & visual science, 2006. **47**(4): p. 1469-76.
110. Latina, M.A. and C. Park, *Selective targeting of trabecular meshwork cells: in vitro studies of pulsed and CW laser interactions.* Experimental eye research, 1995. **60**(4): p. 359-71.
111. Johnson, D.H., *Human trabecular meshwork cell survival is dependent on perfusion rate.* Investigative ophthalmology & visual science, 1996. **37**(6): p. 1204-8.
112. Johnson, D.H. and R.C. Tschumper, *Human trabecular meshwork organ culture. A new method.* Investigative ophthalmology & visual science, 1987. **28**(6): p. 945-53.
113. Johnson, D.H. and R.C. Tschumper, *The effect of organ culture on human trabecular meshwork.* Experimental eye research, 1989. **49**(1): p. 113-27.
114. Acott, T.S., et al., *Intraocular pressure homeostasis: maintaining balance in a high-pressure environment.* Journal of ocular pharmacology and therapeutics : the official journal of the Association for Ocular Pharmacology and Therapeutics, 2014. **30**(2-3): p. 94-101.
115. Mao, W., et al., *Perfusion-cultured bovine anterior segments as an ex vivo model for studying glucocorticoid-induced ocular hypertension and glaucoma.* Investigative ophthalmology & visual science, 2011. **52**(11): p. 8068-75.
116. Kumar, J. and D.L. Epstein, *Rho GTPase-mediated cytoskeletal organization in Schlemm's canal cells play a critical role in the regulation of aqueous humor outflow facility.* Journal of cellular biochemistry, 2011. **112**(2): p. 600-6.
117. Erickson-Lamy, K., J.W. Rohen, and W.M. Grant, *Outflow facility studies in the perfused bovine aqueous outflow pathways.* Current eye research, 1988. **7**(8): p. 799-807.
118. Boussommier-Calleja, A., et al., *Pharmacologic manipulation of conventional outflow facility in ex vivo mouse eyes.* Investigative ophthalmology & visual science, 2012. **53**(9): p. 5838-45.

119. Knepper, P.A., J.A. Collins, and R. Frederick, *Effects of dexamethasone, progesterone, and testosterone on IOP and GAGs in the rabbit eye.* Investigative ophthalmology & visual science, 1985. **26**(8): p. 1093-100.
120. Gong, H. and T.F. Freddo, *The washout phenomenon in aqueous outflow--why does it matter?* Experimental eye research, 2009. **88**(4): p. 729-37.
121. Johnson, M., et al., *The pressure and volume dependence of the rate of wash-out in the bovine eye.* Current eye research, 1991. **10**(4): p. 373-5.
122. Scott, P.A., et al., *Comparative studies between species that do and do not exhibit the washout effect.* Experimental eye research, 2007. **84**(3): p. 435-43.
123. Erickson, K.A. and P.L. Kaufman, *Comparative effects of three ocular perfusates on outflow facility in the cynomolgus monkey.* Current eye research, 1981. **1**(4): p. 211-6.
124. Brubaker, R.F., *Goldmann's equation and clinical measures of aqueous dynamics.* Experimental eye research, 2004. **78**(3): p. 633-7.
125. Langer, R., *Perspectives and challenges in tissue engineering and regenerative medicine.* Advanced materials, 2009. **21**(32-33): p. 3235-6.
126. Andersson, H. and A. van den Berg, *Microfabrication and microfluidics for tissue engineering: state of the art and future opportunities.* Lab on a chip, 2004. **4**(2): p. 98-103.
127. Cautinho, D., et al., *Micro- and Nanotechnology in Tissue Engineering*, in *Tissue Engineering*, N. Pallua and C.V. Suscheck, Editors. 2011, Springer. p. 3-29.
128. Dvir, T., et al., *Nanotechnological strategies for engineering complex tissues.* Nature nanotechnology, 2011. **6**(1): p. 13-22.
129. Koegler, W.S. and L.G. Griffith, *Osteoblast response to PLGA tissue engineering scaffolds with PEO modified surface chemistries and demonstration of patterned cell response.* Biomaterials, 2004. **25**(14): p. 2819-30.
130. Bettinger, C.J., R. Langer, and J.T. Borenstein, *Engineering substrate topography at the micro- and nanoscale to control cell function.* Angewandte Chemie, 2009. **48**(30): p. 5406-15.
131. Bettinger, C.J., et al., *Biocompatibility of biodegradable semiconducting melanin films for nerve tissue engineering.* Biomaterials, 2009. **30**(17): p. 3050-7.
132. Barber, R.W. and D.R. Emerson, *Biomimetic design of artificial micro-vasculatures for tissue engineering.* Alternatives to laboratory animals : ATLA, 2010. **38 Suppl 1**: p. 67-79.
133. Giordano, R.A., et al., *Mechanical properties of dense polylactic acid structures fabricated by three dimensional printing.* Journal of biomaterials science. Polymer edition, 1996. **8**(1): p. 63-75.
134. Hsu, S.H., et al., *Oriented Schwann cell growth on microgrooved surfaces.* Biotechnology and bioengineering, 2005. **92**(5): p. 579-88.
135. Yu, X., et al., *Biomaterials for Bone Regenerative Engineering.* Advanced healthcare materials, 2015.
136. Amini, A.R., C.T. Laurencin, and S.P. Nukavarapu, *Bone tissue engineering: recent advances and challenges.* Critical reviews in biomedical engineering, 2012. **40**(5): p. 363-408.
137. Betancourt, T. and L. Brannon-Peppas, *Micro- and nanofabrication methods in nanotechnological medical and pharmaceutical devices.* International journal of nanomedicine, 2006. **1**(4): p. 483-95.
138. Gonzalez, J.M., Jr., M. Heur, and J.C. Tan, *Two-photon immunofluorescence characterization of the trabecular meshwork in situ.* Investigative ophthalmology & visual science, 2012. **53**(7): p. 3395-404.
139. Kim, B., *Multidisciplinary Engineered Approaches to Investigate Human Trabecular Meshwork Endothelial Cells in Regulation of Intraocular Pressure*, in *Biomedical Engineering*2011, The Ohio State University: Columbus.

140. Tian, B., et al., *Cytoskeletal involvement in the regulation of aqueous humor outflow.* Investigative ophthalmology & visual science, 2000. **41**(3): p. 619-23.
141. Voskerician, G., et al., *Biocompatibility and biofouling of MEMS drug delivery devices.* Biomaterials, 2003. **24**(11): p. 1959-67.
142. Kotzar, G., et al., *Evaluation of MEMS materials of construction for implantable medical devices.* Biomaterials, 2002. **23**(13): p. 2737-50.
143. Mata A., F.A.J., Roy S., *Fabrication of multi-layer SU-8 microstructure.* Journal of Mcromechanics and Microengineering, 2006. **30**(27): p. 4610-4617.
144. Hennemeyer M, W.F., Kerstan S, Schurzinger K, Gigler AM, Stark RW, *Cell proliferation assays on plasma activated SU-8.* Microelectronic Engineering, 2008(85): p. 1298-1301.
145. Iborra, A., et al., *Expression of complement regulatory proteins [membrane cofactor protein (CD46), decay accelerating factor (CD55), and protectin (CD59)] in endometrial stressed cells.* Cellular immunology, 2003. **223**(1): p. 46-51.
146. Lee, J.T. and K.L. Chow, *SEM sample preparation for cells on 3D scaffolds by freeze-drying and HMDS.* Scanning, 2012. **34**(1): p. 12-25.
147. Fugel C., T.E.R., Lutjen-Drecoll E., Stefani F., *Age-related loss of a smooth muscle actin in normal and glaucomatous human trabecular meshwork of different age groups.* Glaucoma, 1992(1): p. 165-173.
148. Shen, X., et al., *Rho GTPase and cAMP/protein kinase A signaling mediates myocilin-induced alterations in cultured human trabecular meshwork cells.* The Journal of biological chemistry, 2008. **283**(1): p. 603-12.
149. Wentz-Hunter, K., et al., *Extracellular myocilin affects activity of human trabecular meshwork cells.* Journal of cellular physiology, 2004. **200**(1): p. 45-52.
150. Welge-Lussen, U., et al., *AlphaB-crystallin in the trabecular meshwork is inducible by transforming growth factor-beta.* Investigative ophthalmology & visual science, 1999. **40**(10): p. 2235-41.
151. Gasier, H.G., et al., *Cumulative responses of muscle protein synthesis are augmented with chronic resistance exercise training.* Acta physiologica, 2011. **201**(3): p. 381-9.
152. Spector, I., et al., *Latrunculins: novel marine toxins that disrupt microfilament organization in cultured cells.* Science, 1983. **219**(4584): p. 493-5.
153. McKee, C.T., et al., *The effect of biophysical attributes of the ocular trabecular meshwork associated with glaucoma on the cell response to therapeutic agents.* Biomaterials, 2011. **32**(9): p. 2417-23.
154. Alvarado, J.A., I. Wood, and J.R. Polansky, *Human trabecular cells. II. Growth pattern and ultrastructural characteristics.* Investigative ophthalmology & visual science, 1982. **23**(4): p. 464-78.
155. Resch, Z.T., et al., *Aqueous humor rapidly stimulates myocilin secretion from human trabecular meshwork cells.* Experimental eye research, 2010. **91**(6): p. 901-8.
156. Llobet, A., V. Beaumont, and L. Lagnado, *Real-time measurement of exocytosis and endocytosis using interference of light.* Neuron, 2003. **40**(6): p. 1075-86.
157. Falco, G., et al., *Polycyclic aromatic hydrocarbons in foods: human exposure through the diet in Catalonia, Spain.* Journal of food protection, 2003. **66**(12): p. 2325-31.
158. Perkins, T.W., et al., *Trabecular meshwork cells grown on filters. Conductivity and cytochalasin effects.* Investigative ophthalmology & visual science, 1988. **29**(12): p. 1836-46.
159. Costas, M., et al., *Dinuclear copper(I) complexes with hexaaza macrocyclic dinucleating ligands: structure and dynamic properties.* Inorganic chemistry, 2003. **42**(14): p. 4456-68.
160. Domingo, J.L., et al., *Polychlorinated naphthalenes in foods: estimated dietary intake by the population of Catalonia, Spain.* Environmental science & technology, 2003. **37**(11): p. 2332-5.

161. Bocio, A., et al., *Polybrominated diphenyl ethers (PBDEs) in foodstuffs: human exposure through the diet.* Journal of agricultural and food chemistry, 2003. **51**(10): p. 3191-5.
162. Llobet, A., A. Cooke, and L. Lagnado, *Exocytosis at the ribbon synapse of retinal bipolar cells studied in patches of presynaptic membrane.* The Journal of neuroscience : the official journal of the Society for Neuroscience, 2003. **23**(7): p. 2706-14.
163. Sens, C., et al., *Synthesis, structure, and spectroscopic, photochemical, redox, and catalytic properties of ruthenium(II) isomeric complexes containing dimethyl sulfoxide, chloro, and the dinucleating bis(2-pyridyl)pyrazole ligands.* Inorganic chemistry, 2003. **42**(6): p. 2040-8.
164. Llobet, J.M., et al., *Levels of polychlorinated biphenyls in foods from Catalonia, Spain: estimated dietary intake.* Journal of food protection, 2003. **66**(3): p. 479-84.
165. Gasull, X., et al., *Cell membrane stretch modulates the high-conductance Ca2+-activated K+ channel in bovine trabecular meshwork cells.* Investigative ophthalmology & visual science, 2003. **44**(2): p. 706-14.
166. Llobet, J.M., et al., *Human exposure to dioxins through the diet in Catalonia, Spain: carcinogenic and non-carcinogenic risk.* Chemosphere, 2003. **50**(9): p. 1193-200.
167. Llobet, J.M., et al., *Concentrations of arsenic, cadmium, mercury, and lead in common foods and estimated daily intake by children, adolescents, adults, and seniors of Catalonia, Spain.* Journal of agricultural and food chemistry, 2003. **51**(3): p. 838-42.
168. Peredkov, A.L.B.a.S.S., *Use of SU-8 photoresist for very high aspect ratio x-ray lithography.* Microelectronic Engineering, 2000. **53**: p. 493-496.
169. Llobet, A., X. Gasull, and A. Gual, *Understanding trabecular meshwork physiology: a key to the control of intraocular pressure?* News in physiological sciences : an international journal of physiology produced jointly by the International Union of Physiological Sciences and the American Physiological Society, 2003. **18**: p. 205-9.
170. Freddo, T.F., et al., *Influence of mercurial sulfhydryl agents on aqueous outflow pathways in enucleated eyes.* Investigative ophthalmology & visual science, 1984. **25**(3): p. 278-85.
171. Spencer, W.H., J. Alvarado, and T.L. Hayes, *Scanning electron microscopy of human ocular tissues: trabecular meshwork.* Investigative ophthalmology, 1968. **7**(6): p. 651-62.
172. Kater, K.M., N.S. Kuhrik, and M. Kuhrik, *Corralling atrial fibrillation with 'maze' surgery.* The American journal of nursing, 1992. **92**(7): p. 34-8.
173. Moradell, S., et al., *Platinum complexes of diaminocarboxylic acids and their ethyl ester derivatives: the effect of the chelate ring size on antitumor activity and interactions with GMP and DNA.* Journal of inorganic biochemistry, 2003. **96**(4): p. 493-502.
174. Brody, S., et al., *Characterizing nanoscale topography of the aortic heart valve basement membrane for tissue engineering heart valve scaffold design.* Tissue engineering, 2006. **12**(2): p. 413-21.
175. Liliensiek, S.J., et al., *The scale of substratum topographic features modulates proliferation of corneal epithelial cells and corneal fibroblasts.* Journal of biomedical materials research. Part A, 2006. **79**(1): p. 185-92.
176. Diehl, K.A., et al., *Nanoscale topography modulates corneal epithelial cell migration.* Journal of biomedical materials research. Part A, 2005. **75**(3): p. 603-11.
177. Thomasy, S.M., et al., *Substratum stiffness and latrunculin B regulate matrix gene and protein expression in human trabecular meshwork cells.* Investigative ophthalmology & visual science, 2012. **53**(2): p. 952-8.
178. Wood, J.A., et al., *Substratum compliance regulates human trabecular meshwork cell behaviors and response to latrunculin B.* Investigative ophthalmology & visual science, 2011. **52**(13): p. 9298-303.

179. Nilsson, M.I., et al., *Insulin resistance syndrome blunts the mitochondrial anabolic response following resistance exercise.* American journal of physiology. Endocrinology and metabolism, 2010. **299**(3): p. E466-74.
180. Gabelt, B.T. and P.L. Kaufman, *Aqueous Humor Hydrodynamics*, in *Adler's Physiology of the Eye*, W.M. Hart, Editor 2003, Mosby: St. Louis, MO.
181. Bernstein, H.N., D.W. Mills, and B. Becker, *Steroid-induced elevation of intraocular pressure.* Archives of ophthalmology, 1963. **70**: p. 15-8.
182. Garbe, E., et al., *Inhaled and nasal glucocorticoids and the risks of ocular hypertension or open-angle glaucoma.* JAMA : the journal of the American Medical Association, 1997. **277**(9): p. 722-7.
183. Cubey, R.B., *Glaucoma following the application of corticosteroid to the skin of the eyelids.* The British journal of dermatology, 1976. **95**(2): p. 207-8.
184. Garrott, H.M. and M.J. Walland, *Glaucoma from topical corticosteroids to the eyelids.* Clinical & experimental ophthalmology, 2004. **32**(2): p. 224-6.
185. Kalina, R.E., *Increased intraocular pressure following subconjunctival corticosteroid administration.* Archives of ophthalmology, 1969. **81**(6): p. 788-90.
186. Behbehani, A.H., et al., *Cataract and ocular hypertension in children on inhaled corticosteroid therapy.* Journal of pediatric ophthalmology and strabismus, 2005. **42**(1): p. 23-7.
187. Becker, B. and D.W. Mills, *Corticosteroids and Intraocular Pressure.* Archives of ophthalmology, 1963. **70**: p. 500-7.
188. Jones, R., 3rd and D.J. Rhee, *Corticosteroid-induced ocular hypertension and glaucoma: a brief review and update of the literature.* Current opinion in ophthalmology, 2006. **17**(2): p. 163-7.
189. Kersey, J.P. and D.C. Broadway, *Corticosteroid-induced glaucoma: a review of the literature.* Eye, 2006. **20**(4): p. 407-16.
190. Bernstein, H.N. and B. Schwartz, *Effects of long-term systemic steroids on ocular pressure and tonographic values.* Archives of ophthalmology, 1962. **68**: p. 742-53.
191. Fautsch, M.P., et al., *Recombinant TIGR/MYOC increases outflow resistance in the human anterior segment.* Investigative ophthalmology & visual science, 2000. **41**(13): p. 4163-8.
192. Clark, A.F., et al., *Dexamethasone alters F-actin architecture and promotes cross-linked actin network formation in human trabecular meshwork tissue.* Cell motility and the cytoskeleton, 2005. **60**(2): p. 83-95.
193. Hoare, M.J., et al., *Cross-linked actin networks (CLANs) in the trabecular meshwork of the normal and glaucomatous human eye in situ.* Investigative ophthalmology & visual science, 2009. **50**(3): p. 1255-63.
194. Read, A.T., D.W. Chan, and C.R. Ethier, *Actin structure in the outflow tract of normal and glaucomatous eyes.* Experimental eye research, 2007. **84**(1): p. 214-26.
195. Tripathi, B.J., R.C. Tripathi, and H.H. Swift, *Hydrocortisone-induced DNA endoreplication in human trabecular cells in vitro.* Experimental eye research, 1989. **49**(2): p. 259-70.
196. Matsumoto, Y. and D.H. Johnson, *Dexamethasone decreases phagocytosis by human trabecular meshwork cells in situ.* Investigative ophthalmology & visual science, 1997. **38**(9): p. 1902-7.
197. Matsumoto, Y. and D.H. Johnson, *Trabecular meshwork phagocytosis in glaucomatous eyes.* Ophthalmologica. Journal international d'ophtalmologie. International journal of ophthalmology. Zeitschrift fur Augenheilkunde, 1997. **211**(3): p. 147-52.
198. Tripathi, R.C. and B.J. Tripathi, *Functional anatomy of the anterior chamber angle*. Duane's biomedical foundations of ophthalmology, ed. T. W.W. and J. E.A. Vol. 1. 1989, Philadelphia (PA): JB Lippincott Co.
199. Tian, B. and P.L. Kaufman, *Effects of the Rho kinase inhibitor Y-27632 and the phosphatase inhibitor calyculin A on outflow facility in monkeys.* Experimental eye research, 2005. **80**(2): p. 215-25.

200. Tokushige, H., et al., *Effects of topical administration of y-39983, a selective rho-associated protein kinase inhibitor, on ocular tissues in rabbits and monkeys.* Investigative ophthalmology & visual science, 2007. **48**(7): p. 3216-22.
201. Tanihara, H., et al., *Intraocular pressure-lowering effects and safety of topical administration of a selective ROCK inhibitor, SNJ-1656, in healthy volunteers.* Archives of ophthalmology, 2008. **126**(3): p. 309-15.
202. Williams, R.D., et al., *Ocular hypotensive effect of the Rho kinase inhibitor AR-12286 in patients with glaucoma and ocular hypertension.* American journal of ophthalmology, 2011. **152**(5): p. 834-41 e1.
203. Tanihara, H., et al., *Phase 2 randomized clinical study of a Rho kinase inhibitor, K-115, in primary open-angle glaucoma and ocular hypertension.* American journal of ophthalmology, 2013. **156**(4): p. 731-6.
204. Torrejon, K.Y., et al., *Recreating a human trabecular meshwork outflow system on microfabricated porous structures.* Biotechnology and bioengineering, 2013. **110**(12): p. 3205-18.
205. Giaever, I. and C.R. Keese, *Monitoring fibroblast behavior in tissue culture with an applied electric field.* Proceedings of the National Academy of Sciences of the United States of America, 1984. **81**(12): p. 3761-4.
206. Stolwijk, J.A., et al., *Impedance analysis of GPCR-mediated changes in endothelial barrier function: overview and fundamental considerations for stable and reproducible measurements.* Pflugers Archiv : European journal of physiology, 2014.
207. Johnson, D., et al., *Ultrastructural changes in the trabecular meshwork of human eyes treated with corticosteroids.* Archives of ophthalmology, 1997. **115**(3): p. 375-83.
208. Clark, A.F., et al., *Dexamethasone-induced ocular hypertension in perfusion-cultured human eyes.* Investigative ophthalmology & visual science, 1995. **36**(2): p. 478-89.
209. Bill, A., *Editorial: The drainage of aqueous humor.* Investigative ophthalmology, 1975. **14**(1): p. 1-3.
210. Lo, C.M., C.R. Keese, and I. Giaever, *Monitoring motion of confluent cells in tissue culture.* Experimental cell research, 1993. **204**(1): p. 102-9.
211. Pang, I.H., et al., *Expression of matrix metalloproteinases and their inhibitors in human trabecular meshwork cells.* Investigative ophthalmology & visual science, 2003. **44**(8): p. 3485-93.
212. De Groef, L., et al., *MMPs in the trabecular meshwork: promising targets for future glaucoma therapies?* Investigative ophthalmology & visual science, 2013. **54**(12): p. 7756-63.
213. Snyder, R.W., et al., *Corticosteroid treatment and trabecular meshwork proteases in cell and organ culture supernatants.* Experimental eye research, 1993. **57**(4): p. 461-8.
214. Vittitow, J. and T. Borras, *Genes expressed in the human trabecular meshwork during pressure-induced homeostatic response.* Journal of cellular physiology, 2004. **201**(1): p. 126-37.
215. Gonzalez-Avila, G., et al., *Collagen metabolism in human aqueous humor from primary open-angle glaucoma. Decreased degradation and increased biosynthesis play a role in its pathogenesis.* Archives of ophthalmology, 1995. **113**(10): p. 1319-23.
216. Tripathi, R.C., et al., *Growth factors in the aqueous humor and their clinical significance.* Journal of glaucoma, 1994. **3**(3): p. 248-58.
217. Tripathi, B.J., et al., *Trabecular cell expression of fibronectin and MMP-3 is modulated by aqueous humor growth factors.* Experimental eye research, 2004. **78**(3): p. 653-60.
218. Wen, F.Q., et al., *Glucocorticoids modulate TGF-beta production by human fetal lung fibroblasts.* Inflammation, 2003. **27**(1): p. 9-19.

219. Armaly, M.F., *Effect of Corticosteroids on Intraocular Pressure and Fluid Dynamics. Ii. The Effect of Dexamethasone in the Glaucomatous Eye.* Archives of ophthalmology, 1963. **70**: p. 492-9.
220. Johnson, D.H., J.M. Bradley, and T.S. Acott, *The effect of dexamethasone on glycosaminoglycans of human trabecular meshwork in perfusion organ culture.* Investigative ophthalmology & visual science, 1990. **31**(12): p. 2568-71.
221. Francois, J. and V. Victoria-Troncoso, *Corticosteroid glaucoma.* Ophthalmologica. Journal international d'ophtalmologie. International journal of ophthalmology. Zeitschrift fur Augenheilkunde, 1977. **174**(4): p. 195-209.
222. Yue, B.Y., *The extracellular matrix and its modulation in the trabecular meshwork.* Survey of ophthalmology, 1996. **40**(5): p. 379-90.
223. Zhou, L., Y. Li, and B.Y. Yue, *Glucocorticoid effects on extracellular matrix proteins and integrins in bovine trabecular meshwork cells in relation to glaucoma.* International journal of molecular medicine, 1998. **1**(2): p. 339-46.
224. Samples, J.R., J.P. Alexander, and T.S. Acott, *Regulation of the levels of human trabecular matrix metalloproteinases and inhibitor by interleukin-1 and dexamethasone.* Investigative ophthalmology & visual science, 1993. **34**(12): p. 3386-95.
225. Conley, S.M., et al., *Selenium's effects on MMP-2 and TIMP-1 secretion by human trabecular meshwork cells.* Investigative ophthalmology & visual science, 2004. **45**(2): p. 473-9.
226. Sanka, K., et al., *Influence of actin cytoskeletal integrity on matrix metalloproteinase-2 activation in cultured human trabecular meshwork cells.* Investigative ophthalmology & visual science, 2007. **48**(5): p. 2105-14.
227. Zhang, X., et al., *Dexamethasone inhibition of trabecular meshwork cell phagocytosis and its modulation by glucocorticoid receptor beta.* Experimental eye research, 2007. **84**(2): p. 275-84.
228. Acott, T.S., *Biochemistry of aqueous humor outflow*. Glaucoma, ed. P.L. Kaufman and T.Q. Mitaq1994, Lonson: Mosby.
229. Wordinger, R.J. and A.F. Clark, *Effects of glucocorticoids on the trabecular meshwork: towards a better understanding of glaucoma.* Progress in Retinal and Eye Research, 1999. **18**(5): p. 629-67.
230. Tripathi, R.C., et al., *Corticosteroids and glaucoma risk.* Drugs & aging, 1999. **15**(6): p. 439-50.
231. Olson, M.W., et al., *Kinetic analysis of the binding of human matrix metalloproteinase-2 and -9 to tissue inhibitor of metalloproteinase (TIMP)-1 and TIMP-2.* The Journal of biological chemistry, 1997. **272**(47): p. 29975-83.
232. Gerometta, R., et al., *Treatment of sheep steroid-induced ocular hypertension with a glucocorticoid-inducible MMP1 gene therapy virus.* Investigative ophthalmology & visual science, 2010. **51**(6): p. 3042-8.
233. Geiger, B., et al., *Transmembrane crosstalk between the extracellular matrix--cytoskeleton crosstalk.* Nature reviews. Molecular cell biology, 2001. **2**(11): p. 793-805.
234. Provenzano, P.P., et al., *Matrix density-induced mechanoregulation of breast cell phenotype, signaling and gene expression through a FAK-ERK linkage.* Oncogene, 2009. **28**(49): p. 4326-43.
235. Cukierman, E., et al., *Taking cell-matrix adhesions to the third dimension.* Science, 2001. **294**(5547): p. 1708-12.
236. Johnson, D.H., *The effect of cytochalasin D on outflow facility and the trabecular meshwork of the human eye in perfusion organ culture.* Investigative ophthalmology & visual science, 1997. **38**(13): p. 2790-9.
237. Tian, B., et al., *Combined effects of H-7 and cytochalasin B on outflow facility in monkeys.* Experimental eye research, 1999. **68**(6): p. 649-55.
238. Honjo, M., et al., *Effects of rho-associated protein kinase inhibitor Y-27632 on intraocular pressure and outflow facility.* Investigative ophthalmology & visual science, 2001. **42**(1): p. 137-44.

239. Sabanay, I., et al., *Functional and structural reversibility of H-7 effects on the conventional aqueous outflow pathway in monkeys.* Experimental eye research, 2004. **78**(1): p. 137-50.
240. Stolwijk, J.A., S. Michaelis, and J. Wegener, *Electric Cell-Substrate Impedance Sensing and Cancer Metastasis*, ed. W.G. Jiang2012, London: Springer.
241. Zhong, C., et al., *Rho-mediated contractility exposes a cryptic site in fibronectin and induces fibronectin matrix assembly.* The Journal of cell biology, 1998. **141**(2): p. 539-51.
242. Yoneda, A., et al., *Fibronectin matrix assembly requires distinct contributions from Rho kinases I and -II.* Molecular biology of the cell, 2007. **18**(1): p. 66-75.
243. Overby, D., et al., *The mechanism of increasing outflow facility during washout in the bovine eye.* Investigative ophthalmology & visual science, 2002. **43**(11): p. 3455-64.
244. Rao, P.V., et al., *Modulation of aqueous humor outflow facility by the Rho kinase-specific inhibitor Y-27632.* Investigative ophthalmology & visual science, 2001. **42**(5): p. 1029-37.
245. Fujimoto, T., et al., *Involvement of RhoA/Rho-associated kinase signal transduction pathway in dexamethasone-induced alterations in aqueous outflow.* Investigative ophthalmology & visual science, 2012. **53**(11): p. 7097-108.
246. Lutjen-Drecoll, E., et al., *Localization of the stress proteins alpha B-crystallin and trabecular meshwork inducible glucocorticoid response protein in normal and glaucomatous trabecular meshwork.* Investigative ophthalmology & visual science, 1998. **39**(3): p. 517-25.
247. Kottler, U.B., et al., *Comparative effects of TGF-beta 1 and TGF-beta 2 on extracellular matrix production, proliferation, migration, and collagen contraction of human Tenon's capsule fibroblasts in pseudoexfoliation and primary open-angle glaucoma.* Experimental eye research, 2005. **80**(1): p. 121-34.
248. Connor, T.B., Jr., et al., *Correlation of fibrosis and transforming growth factor-beta type 2 levels in the eye.* The Journal of clinical investigation, 1989. **83**(5): p. 1661-6.
249. Picht, G., et al., *Transforming growth factor beta 2 levels in the aqueous humor in different types of glaucoma and the relation to filtering bleb development.* Graefe's archive for clinical and experimental ophthalmology = Albrecht von Graefes Archiv fur klinische und experimentelle Ophthalmologie, 2001. **239**(3): p. 199-207.
250. Welge-Lussen, U., C.A. May, and E. Lutjen-Drecoll, *Induction of tissue transglutaminase in the trabecular meshwork by TGF-beta1 and TGF-beta2.* Investigative ophthalmology & visual science, 2000. **41**(8): p. 2229-38.
251. Gottanka, J., et al., *Effects of TGF-beta2 in perfused human eyes.* Investigative ophthalmology & visual science, 2004. **45**(1): p. 153-8.
252. Fuchshofer, R., U. Welge-Lussen, and E. Lutjen-Drecoll, *The effect of TGF-beta2 on human trabecular meshwork extracellular proteolytic system.* Experimental eye research, 2003. **77**(6): p. 757-65.
253. Fletcher, D.A. and R.D. Mullins, *Cell mechanics and the cytoskeleton.* Nature, 2010. **463**(7280): p. 485-92.
254. Pattabiraman, P.P. and P.V. Rao, *Mechanistic basis of Rho GTPase-induced extracellular matrix synthesis in trabecular meshwork cells.* American journal of physiology. Cell physiology, 2010. **298**(3): p. C749-63.
255. Tamm, E.R., et al., *Transforming growth factor-beta 1 induces alpha-smooth muscle-actin expression in cultured human and monkey trabecular meshwork.* Experimental eye research, 1996. **62**(4): p. 389-97.
256. Wallace, D.M., et al., *The role of matricellular proteins in glaucoma.* Matrix biology : journal of the International Society for Matrix Biology, 2014. **37**: p. 174-82.
257. Stone, E.M., et al., *Identification of a gene that causes primary open angle glaucoma.* Science, 1997. **275**(5300): p. 668-70.

258. Blanchoin, L., et al., *Actin dynamics, architecture, and mechanics in cell motility.* Physiological reviews, 2014. **94**(1): p. 235-63.
259. Han, H., et al., *Elasticity-dependent modulation of TGF-beta responses in human trabecular meshwork cells.* Investigative ophthalmology & visual science, 2011. **52**(6): p. 2889-96.
260. Goffin, J.M., et al., *Focal adhesion size controls tension-dependent recruitment of alpha-smooth muscle actin to stress fibers.* The Journal of cell biology, 2006. **172**(2): p. 259-68.
261. Pattabiraman, P.P., R. Maddala, and P.V. Rao, *Regulation of plasticity and fibrogenic activity of trabecular meshwork cells by Rho GTPase signaling.* Journal of cellular physiology, 2014. **229**(7): p. 927-42.
262. Wecker, T., et al., *Effects of TGF-beta2 on cadherins and beta-catenin in human trabecular meshwork cells.* Investigative ophthalmology & visual science, 2013. **54**(10): p. 6456-62.
263. Fuchshofer, R. and E.R. Tamm, *Modulation of extracellular matrix turnover in the trabecular meshwork.* Experimental eye research, 2009. **88**(4): p. 683-8.
264. Sato, T. and S. Roy, *Effect of high glucose on fibronectin expression and cell proliferation in trabecular meshwork cells.* Investigative ophthalmology & visual science, 2002. **43**(1): p. 170-5.
265. Fleenor, D.L., I.H. Pang, and A.F. Clark, *Involvement of AP-1 in interleukin-1alpha-stimulated MMP-3 expression in human trabecular meshwork cells.* Investigative ophthalmology & visual science, 2003. **44**(8): p. 3494-501.
266. Fleenor, D.L., et al., *TGFbeta2-induced changes in human trabecular meshwork: implications for intraocular pressure.* Investigative ophthalmology & visual science, 2006. **47**(1): p. 226-34.
267. Wilhelm, S.M., et al., *Human skin fibroblast stromelysin: structure, glycosylation, substrate specificity, and differential expression in normal and tumorigenic cells.* Proceedings of the National Academy of Sciences of the United States of America, 1987. **84**(19): p. 6725-9.
268. Han, H., et al., *TGF-beta2-induced invadosomes in human trabecular meshwork cells.* PloS one, 2013. **8**(8): p. e70595.
269. Okada, Y., T. Matsuo, and H. Ohtsuki, *Bovine trabecular cells produce TIMP-1 and MMP-2 in response to mechanical stretching.* Japanese journal of ophthalmology, 1998. **42**(2): p. 90-4.
270. Bahler, C.K., et al., *Pharmacologic disruption of Schlemm's canal cells and outflow facility in anterior segments of human eyes.* Investigative ophthalmology & visual science, 2004. **45**(7): p. 2246-54.
271. Ethier, C.R. and D.W. Chan, *Cationic ferritin changes outflow facility in human eyes whereas anionic ferritin does not.* Investigative ophthalmology & visual science, 2001. **42**(8): p. 1795-802.
272. Johnson, M., et al., *Modulation of outflow resistance by the pores of the inner wall endothelium.* Investigative ophthalmology & visual science, 1992. **33**(5): p. 1670-5.
273. Maepea, O. and A. Bill, *Pressures in the juxtacanalicular tissue and Schlemm's canal in monkeys.* Experimental eye research, 1992. **54**(6): p. 879-83.
274. Polansky, J.R., D.J. Fauss, and C.C. Zimmerman, *Regulation of TIGR/MYOC gene expression in human trabecular meshwork cells.* Eye, 2000. **14 (Pt 3B)**: p. 503-14.
275. Pedrigi, R.M., et al., *A model of giant vacuole dynamics in human Schlemm's canal endothelial cells.* Experimental eye research, 2011. **92**(1): p. 57-66.
276. Stamer, W.D., et al., *Cellular basis for bimatoprost effects on human conventional outflow.* Investigative ophthalmology & visual science, 2010. **51**(10): p. 5176-81.
277. Tamm, E.R., et al., *Human and monkey trabecular meshwork accumulate alpha B-crystallin in response to heat shock and oxidative stress.* Investigative ophthalmology & visual science, 1996. **37**(12): p. 2402-13.
278. Heimark, R.L., S. Kaochar, and W.D. Stamer, *Human Schlemm's canal cells express the endothelial adherens proteins, VE-cadherin and PECAM-1.* Current eye research, 2002. **25**(5): p. 299-308.

279. Burke, A.G., et al., *Effect of hydrostatic pressure gradients and Na2EDTA on permeability of human Schlemm's canal cell monolayers.* Current eye research, 2004. **28**(6): p. 391-8.
280. Lin, S., et al., *Differentiation of cultured Schlemm's canal endothelial (SCE) and trabecular meshwork (TM) cells into capillary-like structures. [ARVO Abstract].* Investigative ophthalmology & visual science, 1994. **35**(4): p. S2082.
281. Ellis, D.Z., N.A. Sharif, and W.M. Dismuke, *Endogenous regulation of human Schlemm's canal cell volume by nitric oxide signaling.* Investigative ophthalmology & visual science, 2010. **51**(11): p. 5817-24.
282. Dautriche, C.N., et al., *A biomimetic Schlemm's canal inner wall: A model to study outflow physiology, glaucoma pathology and high-throughput drug screening.* Biomaterials, 2015. **65**: p. 86-92.
283. Bhandari, R.N., et al., *Liver tissue engineering: a role for co-culture systems in modifying hepatocyte function and viability.* Tissue engineering, 2001. **7**(3): p. 345-57.
284. Truskey, G.A., *Endothelial Cell Vascular Smooth Muscle Cell Co-Culture Assay For High Throughput Screening Assays For Discovery of Anti-Angiogenesis Agents and Other Therapeutic Molecules.* International journal of high throughput screening, 2010. **2010**(1): p. 171-181.
285. Neofytou, E.A., et al., *Adipose tissue-derived stem cells display a proangiogenic phenotype on 3D scaffolds.* Journal of biomedical materials research. Part A, 2011. **98**(3): p. 383-93.
286. Dautriche, C., *3D-Bioengineering of the Conventional Outflow Tract for High Throughput Drug or Gene Transfer Screening for Glaucoma Treatment*, in *College of Nanoscale Science and Engineering*2015, State University of New York at Albany: Albany, NY.
287. Davis, J.S., B.R. Rueda, and K. Spanel-Borowski, *Microvascular endothelial cells of the corpus luteum.* Reproductive biology and endocrinology : RB&E, 2003. **1**: p. 89.
288. Chung-Welch, N., et al., *Phenotypic comparison between mesothelial and microvascular endothelial cell lineages using conventional endothelial cell markers, cytoskeletal protein markers and in vitro assays of angiogenic potential.* Differentiation; research in biological diversity, 1989. **42**(1): p. 44-53.
289. Scott, P.A. and R. Bicknell, *The isolation and culture of microvascular endothelium.* Journal of cell science, 1993. **105 (Pt 2)**: p. 269-73.
290. Fenyves, A.M., J. Behrens, and K. Spanel-Borowski, *Cultured microvascular endothelial cells (MVEC) differ in cytoskeleton, expression of cadherins and fibronectin matrix. A study under the influence of interferon-gamma.* Journal of cell science, 1993. **106 (Pt 3)**: p. 879-90.
291. Liu, K.C., et al., *Role of VEGF in Conventional Outflow Homeostasis.* Investigative ophthalmology & visual science, 2014. **55**(13): p. 2910.
292. Gonzalez, P., et al., *Expression analysis of the matrix GLA protein and VE-cadherin gene promoters in the outflow pathway.* Investigative ophthalmology & visual science, 2004. **45**(5): p. 1389-95.
293. Iljin, K., et al., *VEGFR3 gene structure, regulatory region, and sequence polymorphisms.* FASEB journal : official publication of the Federation of American Societies for Experimental Biology, 2001. **15**(6): p. 1028-36.
294. Resch, Z.T. and M.P. Fautsch, *Glaucoma-associated myocilin: a better understanding but much more to learn.* Experimental eye research, 2009. **88**(4): p. 704-12.
295. O'Brien, E.T., X. Ren, and Y. Wang, *Localization of myocilin to the golgi apparatus in Schlemm's canal cells.* Investigative ophthalmology & visual science, 2000. **41**(12): p. 3842-9.
296. Grierson, I. and W.R. Lee, *Light microscopic quantitation of the endothelial vacuoles in Schlemm's canal.* American journal of ophthalmology, 1977. **84**(2): p. 234-46.